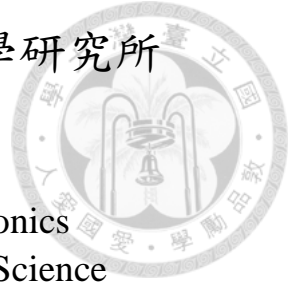


國立臺灣大學電資資訊學院光電工程學研究所



碩士論文

Graduate Institute of Photonics and Optoelectronics  
College of Electrical Engineering and Computer Science

National Taiwan University

Master Thesis

具腈基小分子有機太陽能電池之優化與紅螢烯薄膜激  
子動態特性之研究

Device optimization for small molecular organic solar  
cell with cyano groups and exciton dynamics of rubrene  
thin film

陳佳勳

Chia-Hsun Chen

指導教授：李君浩 博士

Advisor: Jiun-Haw Lee, Ph.D.

中華民國104年6月

June, 2015



國立臺灣大學碩士學位論文  
口試委員會審定書

具腈基小分子有機太陽能電池之優化與  
紅螢烯薄膜激子動態特性之研究  
Device Optimization for Small Molecular Organic  
Solar Cell with Cyano Groups and Exciton  
Dynamics of Rubrene Thin Film

本論文係陳佳勳君（學號 R02941007）在國立臺灣大學  
光電工程學研究所完成之碩士學位論文，於民國 104 年 6 月  
16 日承下列考試委員審查通過及口試及格，特此證明

口試委員：

李君浩

（指導教授）

王俊凱

邵天浩

汪松標

洪仲地

所長

林恭如

## 致謝



這篇論文今日能夠完整呈現，亦或能順利完成碩士的生涯，最主要要感謝筆者的指導教授李君浩老師，不只在求學的過程中，提供實驗上的建議與創新的見解，使得在自我思考與判辨上有一大精進，且不願辛勞的包容過錯與教導，在自身的待人處事上更有莫大的幫助。

另外，也要感謝實驗室裡支持並給予鼓勵的筆者的每個人，特別感謝邱天隆及林奇鋒教授，兩位老師在實驗的思考與討論上給了非常大的鼓勵，並且在問題面對上提供了明確的方向，解決了種種的困難。更要謝謝過去曾經幫助過或給予鼓勵的學長姐們：梓堯、Nemo、傳恩、博聖、Joanne、舜博、維甫、嘉呈、伯彥、義信，特別感謝柏勳學長在兩年來的幫忙，受益匪淺、難以言喻。二者，也要感謝同甘共苦的同儕們：詒澤、政韻、力嘉、御翔，從碩士生涯中是最能同甘共苦的好夥伴，還有學弟們：政斌、明哲、浩淳、資展、煥捷、建良的陪伴。

此求學生涯之成果，亦感謝在此幫助過筆者的貴人。要特別感謝中研院原分所王俊凱老師提供的量測環境，讓我能順利完成此篇之第四章，並且適時提供精闢的質疑與鼓勵，特別感謝佘斌豪博士，在實驗架設與討論上給予了莫大的幫忙，也要感謝藍鈺邴與鄭天佑學長在 AFM 上的協助。本文的第三章之呈獻，主要感謝化學所汪根權老師與丁浩淳學長，能協助提供小分子材料讓我可以無後顧之憂的進行實驗。也感謝陳錦地教授在會議上提供豐富的見解與幫助，並不辭辛勞的擔任口試委員。學海無涯，然而不僅是此篇成果的呈現，且有今日之成就，在學途曾協助筆者並提升自我修生之人難以計數，但又缺一不可。

最後將此篇成果獻給在人生路途上支持我的家人：父親陳基漳先生；母親黃麗敏女士；弟弟陳佳緯，兩隻天竺鼠，還有我最愛的小貓咪，有家人的支持與陪伴如今筆者才得以走到這並有如今的成果，使我無後顧之憂的學習與成長茁壯。

## 摘要



本論文旨有其二，第一部分將介紹藉由合成四個新的施體材料運用於有機太陽能電池元件，其結構施體 - 施體 - 受體型小分子。

7-(5-(di-p-tolylamino)thiophen-2-yl)benzo[c][1,2,5]thiadiazole-4-carbonitrile (DTCTB), 7-(4-(di-p-tolylamino)phenyl)benzo[c][1,2,5]thiadiazole-4-carbonitrile (DTCPB),

7-(5-(di-p-tolylamino)thiophen-2-yl)benzo[c][1,2,5]oxadiazole-4-carbonitrile (DTCTBO), 及

7-(4-(di-p-tolylamino)phenyl)benzo[c][1,2,5]oxadiazole-4-carbonitrile (DTCPBO). 在一系列由混和濃度及膜厚變化之塊材異質混和界面架構下，利用與受體材料碳70混合，我們可得以四個小分子 DTCPB, DTCTB, DTCPBO 及 DTCTBO 所製成太陽能電池之最佳化功率轉換效率分別為 6.55%, 4.40%, 5.98% 及 4.65%。

二者，我們使用暫態螢光之量測，來瞭解 5,6,11,12-tetraphenylanthracene (rubrene)之單重態分裂(singlet fission)與三重態激子融合(triplet fusion)動態特性。在不同溫度及單重態-單重態滅絕可忽略之前提下，單重態分裂之活化動能可被決定。再者，在膜厚較薄之薄膜中，由於空間局限之故，其會表現出較高機率之三重態激子融合速率。

關鍵字: 有機太陽能電池，塊材異質界面，激發光光譜量測系統，單重態分裂，三重態融合。

## Abstract



There are two parts in this dissertation. In the first part, we employed four donor-donor-acceptor (D-A-A) configurations molecules, 7-(5-(di-p-tolylamino)thiophen-2-yl)benzo[c][1,2,5]thiadiazole-4-carbonitrile (DTCTB), 7-(4-(di-p-tolylamino)phenyl)benzo[c][1,2,5]thiadiazole-4-carbonitrile (DTCPB), 7-(5-(di-p-tolylamino)thiophen-2-yl)benzo[c][1,2,5]oxadiazole-4-carbonitrile (DTCTBO), and 7-(4-(di-p-tolylamino)phenyl)benzo[c][1,2,5]oxadiazole-4-carbonitrile (DTCPBO) as electron donor materials for organic solar cell applications. By a series of methodical optimization, the highest power conversion efficiencies are 6.55%, 4.40%, 5.98%, 4.65% for DTCPB, DTCTB, DTCPBO and DTCTBO respectively with bulk heterojunction configuration.

In the second part of this dissertation, the exciton dynamic of 5,6,11,12-tetraphenylnaphthacene (rubrene) was investigated by transient photoluminescence (TrPL) measurements. With low excitation energy (to avoid singlet-singlet annihilation) at different temperatures, the activation energy of singlet fission (SF) in rubrene thin film can be obtained. We also found that the thinner rubrene exhibited higher fusion rate, which may result from higher probability for non-germinate recombination.

**Keyword:** organic solar cells, bulk heterojunction, transient photoluminescence, singlet fission, and triplet fusion.

# Content



致謝.....	ii
摘要.....	iv
Abstract.....	v
Content.....	vi
1 Chapter 1 Introduction.....	1
1.1 Overview.....	1
1.2 Small molecule organic solar cells.....	2
1.2.1 Introduction of OSC.....	2
1.2.2 Bulk heterojunction configuration.....	4
1.2.3 D-A-A system organic materials.....	5
1.2.4 Recombination mechanisms of OSC.....	7
1.3 Singlet fission.....	9
1.3.1 Introduction.....	9
1.3.2 Exciton dynamics of aromatic based materials.....	11
1.3.3 Caging effect.....	14
1.4 Motivation.....	15
2 Chapter 2 Experiments.....	17
2.1 Introduction.....	17
2.2 Device fabrication and measurement systems for OSC.....	17
2.2.1 Substrate patterning.....	17
2.2.2 Device fabrication.....	18
2.2.3 Device performances measurement.....	19
2.2.4 Measurement of external quantum efficiency (EQE).....	20
2.2.5 Absorption spectrum measurement.....	21

2.2.6	Measurement of optical constants.....	21
2.2.7	Sun variation system.....	22
2.3	Sample fabrication and measurement systems for exciton dynamics .....	23
2.3.1	Samples fabricated for exciton dynamic investigation .....	23
2.3.2	Steady state and time-resolve photoluminence (TrPL) at different temperatures.....	24
3	Chapter 3 Optimization of bulk heterojunction OSC for D-A-A configuration molecule with single cyano group as the electron donor material.....	27
3.1	Introduction.....	27
3.2	Photophysical properties of the four single cyano group electron donor materials.....	27
3.3	OSC optimization of four electron donor materials with single cyano substituent molecules .....	31
3.3.1	Comparison between PMHJ and BHJ of DTCTB devices .....	32
3.3.1.1	C <sub>60</sub> based OSC .....	32
3.3.1.2	C <sub>70</sub> based OSC .....	34
3.3.2	Optimization of different mixing ratio and thickness of active layer for DTCTB .....	36
3.3.2.1	C <sub>60</sub> based OSC .....	37
3.3.2.2	C <sub>70</sub> based OSC .....	39
3.3.2.3	Replacement of different blocking layer for DTCTB: C <sub>60</sub> based OSC .....	42
3.3.3	Comparison between PMHJ and BHJ of DTCPB: C <sub>60</sub> based OSC ....	46
3.3.4	Optimization of mixing ratio and thickness of active layer for DTCPB .....	48
3.3.4.1	C <sub>60</sub> based OSC .....	48



3.3.4.2	C <sub>70</sub> based OSC .....	52
3.3.4.3	Insertion of blocking layer for DTCPB: C <sub>60</sub> based OSC .....	55
3.3.7	Optimization of mixing ratio and thickness of active layer for DTCTBO.....	65
3.3.7.1	C <sub>60</sub> based OSC .....	65
3.4	Comparison of optimized device structures among four single cyano groups electron donor materials.....	70
3.5	Sun intensity variation measurements of OSCs with four single cyano groups electron donor materials.....	73
4	Chapter 4 Exciton dynamics in rubrene thin films .....	74
4.1	Introduction.....	74
4.2	Basic characteristics of amorphous rubrene thin films .....	75
4.3	TrPL of rubrene in toluene .....	76
4.4	TrPL of 100-nm rubrene thin film at 78 K with different excitation energy .	78
4.5	TrPL of 100-nm rubrene thin film at room temperature with different excitation energy .....	79
4.6	TrPL of 100-nm rubrene thin film at different temperatures with ultra-low excitation energy .....	80
4.7	TrPL of rubrene thin film with different thickness and different excitation energy at room temperature .....	84
5	Chapter 5 Conclusion.....	89
5.1	Summary .....	89
5.2	Future work.....	89
	Appendix.....	91
	Appendix. I Morphology for four single cyano groups electron donor materials	91
	Appendix. II Anisotropic characteristics of four single cyano groups electron	

donor materials.....93

References.....95



## Figure content

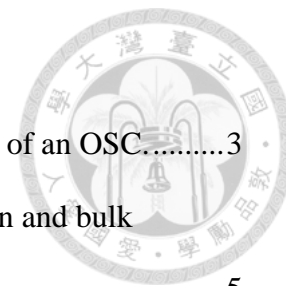


Fig. 1-1 (a) Operation principle and (b) J-V characteristic of an OSC.....	3
Fig. 1-2 Comparison between planar mixed heterojunction and bulk heterojunction OSCs <sup>21</sup> .....	5
Fig. 1-3 Striking a balance between $J_{SC}$ and $V_{OC}$ <sup>26</sup> .....	6
Fig. 1-4 Molecular structures of the D-A-A electron donor materials with BO and BT moieties.....	7
Fig. 1-5 (a) Germinate and non-germinate recombination. (b) Trade-off between $\Delta E_{LUMO}$ and PCE <sup>34</sup> .....	8
Fig. 1-6 Shockley Queisser (SQ) limit for single junction solar cell <sup>55</sup> . .....	10
Fig. 1-7 Operation principles for singlet fission. ....	11
Fig. 1-8 (a) TrPL at 77 and 298 K <sup>68</sup> and (b) energy diagrams of rubrene thin film.....	12
Fig. 1-9 Magnetic field effect on (a) pentacene based OSC <sup>74</sup> and (b) rubrene thin film <sup>68</sup> .....	13
Fig. 1-10 Radiative lifetime of tetracene with various concentration of BC <sup>85</sup> . .....	15
Fig. 2-1 Device configurations. ....	19
Fig. 2-2 Set up of device performances measurement.....	20
Fig. 2-3 Set up of EQE measurement. ....	21
Fig. 2-4 Set up of variable incident angle ellipsometry .....	22
Fig. 2-5 Set up of Sun variation system.....	23
Fig. 2-6 Set up of steady state and time-resolve photoluminescence (TrPL) ...	25
Fig. 2-7 Temperature-controlled sample holder. ....	26
Fig. 3-1 Molecular structures of (a) DTCTB, (b) DTCPB, (c) DTCPBO, (d)	

DTCTBO and (e) DTDCPB.....	28
Fig. 3-2 Absorption spectra of the four molecules (a) in solution, and (b) thin films. ....	29
Fig. 3-3 HOMO of DTCPB, DTCPBO, DTCTB and DTCTBO thin films measured by photoelectron spectrometer. ....	30
Fig. 3-4 Energy diagrams of four single cyano groups moieties molecules with C <sub>60</sub> and C <sub>70</sub> under simple bulk heterojunction .....	32
Fig. 3-5 J-V performances of devices from A-1 to A-4 under (a) dark condition and (b) 1-sun solar illuminations. ....	33
Fig. 3-6 (a) EQE, (b) IQE and (c) absorption spectrum of devices from A-1 to A-4. ....	34
Fig. 3-7 J-V performances of devices from A-5 to A-7 under (a) dark condition and (b) 1-sun solar illuminations. ....	35
Fig. 3-8 (a) EQE, (b) IQE and (c) absorption spectrum of devices from A-5 to A-7. ....	36
Fig. 3-9 J-V performances from of device A-4 to A-12 under (a) dark condition and (b) 1-sun solar illuminations. ....	37
Fig. 3-10 (a) EQE, (b) IQE and (c) absorption spectrum of devices A-8 and A-13. ....	39
Fig. 3-11 J-V performance of devices from 3-20 to 3-22 under (a) dark condition and (b) 1-sun solar illuminations. ....	40
Fig. 3-12 (a) EQE, (b) IQE and (c) absorption spectrum of devices A-7, A-14 to A-15 with different mixing ratio and (d) EQE, (e) IQE and (f) absorption spectrum of devices from A-14, A-16 to A-17 with different thickness of active layer. ....	41
Fig. 3-13 Configurations of devices and energy diagrams for different	

blocking layer of DTCTB:C <sub>60</sub> based OSC.....	43
Fig. 3-14 J-V performances from A-18 to A-25 under (a) mCP inserted dark condition and (b) 1-sun solar illuminations, (c) NPB inserted under dark condition and (d) 1-sun solar illuminations and (e) DTDTB inserted under dark condition and (f) 1-sun solar illuminations.....	44
Fig. 3-15(a) EQE, (b) IQE and (c) absorption spectrum mCP inserted OSC and (d) EQE, (e) IQE and (f) absorption spectrum NPB inserted OSC and (g) EQE, (h) IQE and (i) absorption spectrum mCP inserted OSC and.....	46
Fig. 3-16 J-V performances of devices under (a) dark condition and (b) 1-sun solar illuminations from B-1 to B-7.....	47
Fig. 3-17 (a) EQE, (b) IQE and (c) absorption spectrum of devices from B-1 to B-7. ....	48
Fig. 3-18 J-V performances of devices for B-7, B-10 to B-15 with different thickness under (a) and (c) dark condition and (b) and (d) 1-sun solar illuminations. ....	50
Fig. 3-19 (a) and (d) EQE, (b) and (e) IQE and (c) and (f) absorption spectrum of devices in this section. ....	51
Fig. 3-20 J-V performances of devices from B-16 to B-20 of different mixing ratio under (a) dark condition and (b) 1-sun solar illuminations and different thickness of active layer under (c) dark condition and (d) 1-sun solar illuminations.....	53
Fig. 3-21 (a) EQE, (b) IQE and (c) absorption spectrum of devices with various mixing ratio of mixing layers and (d) EQE, (e) IQE and (e) absorption spectrum of devices with different thickness of active layers for C <sub>70</sub> based OSC.....	54

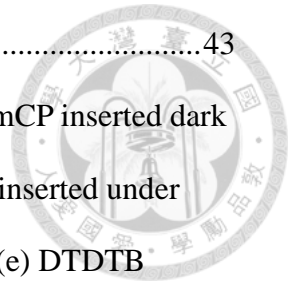


Fig. 3-22 J-V performances of devices from B-5, B-8 to B-9 under (a) dark condition and (b) 1-sun solar illuminations .....	55
Fig. 3-23 (a) EQE, (b) IQE and (c) absorption spectrum of devices from B-5, B-8 to B-9 with various thickness of blocking layers.....	56
Fig. 3-24 J-V performances of devices from C-1 to C-2 as (a) linear, (b) logarithm plots under dark condition and (c) 1-sun solar illuminations. ....	57
Fig. 3-25 (a) EQE, (b) IQE and (c) absorption spectrum of devices from C-1 to C-2 with various relative ratio between mixing and transport layers under 1-sun solar illumination .....	58
Fig. 3-26 J-V performances of devices for (a) different mixing ratio under dark condition, (b) 1-sun solar illuminations and (c) different thicknesses of active layer under dark condition, (d) 1-sun solar illuminations. ....	60
Fig. 3-27 (a) EQE, (b) IQE and (c) absorption spectrum of devices with various mixing ratio of mixing layers and (d) EQE with different thickness of active layers for C <sub>60</sub> based OSC. ....	61
Fig. 3-28 J-V performances of devices under various ratio for (a) dark condition and (b) 1-sun solar illuminations (c) dark with logarithms plot and various thickness for (d) dark condition and (e) 1-sun solar illuminations .....	63
Fig. 3-29 (a) EQE, (b) IQE and (c) absorption spectrum of devices with various mixing ratio of mixing layers and (d) EQE, (e) IQE and (e) absorption spectrum of devices with different thickness of active layers for C <sub>70</sub> based OSC.....	64
Fig. 3-30 J-V performance of devices from D-1 to D-6 under various ratio	

for (a) dark condition and (b) 1-sun solar illumination and under different thickness for (c) dark condition and (d) 1-sun solar illumination.....	66
Fig. 3-31 (a) EQE, (b) IQE and (c) absorption spectrum with various mixing ratio and (d) EQE, (e) IQE and (f) absorption spectrum for different thickness.....	68
Fig. 3-32 J-V performances of devices to with different mixing ratio under (a) dark condition and (b) 1-sun solar illuminations, and various thickness under (c) dark condition and (d) 1-sun solar illuminations..	69
Fig. 3-33 (a) EQE, (b) IQE and (c) absorption spectrum with various mixing ratio and (d) EQE, (e) IQE and (f) absorption spectrum for different thickness.....	70
Fig. 3-34 J-V performances of best devices for four compounds (a) C <sub>60</sub> based under dark condition and (b) 1-sun solar illuminations and (c) C <sub>70</sub> based under dark condition and (d) 1-sun solar illuminations....	71
Fig. 3-35 EQE spectrums of best devices for four compounds (a) C <sub>60</sub> based and (b) C <sub>70</sub> based.....	72
Fig. 3-36 Four parameters under sun variation for four compounds under devices ratio 1:2.2, 70 nm thickness C <sub>70</sub> based (a) V <sub>OC</sub> (b) J <sub>SC</sub> (c) FF (d) PCE.....	73
Fig. 4-1 Normalized TrPL fluorescence decay response for thin-films 4-1 and 4-2 in (a) 40 ns window, and (b) 4 $\mu$ s window.....	75
Fig. 4-2 Absorbance (A) versus rubrene thickness (l).....	76
Fig. 4-3 Normalized TrPL fluorescence decay response for 10 <sup>-5</sup> M rubrene in toluene in (a) 10 ns window, and (b) 0.6 $\mu$ s window..	77
Fig. 4-4 (a) Temperature independent of radiative decay of rubrene in	

polystyrene and (b) normalized absorption spectrum for rubrene in solution and thin film.....	78
Fig. 4-5 Normalized TrPL fluorescence decay response for rubrene 100 nm at 78 K in (a) 40 ns window, and (b) 0.5 $\mu$ s window.....	78
Fig. 4-6 Normalized TrPL fluorescence decay response for rubrene 100 nm at room temperature in (a) 2 ns window, and (b) 2 $\mu$ s window.....	80
Fig. 4-7 Normalized TrPL fluorescence decay for rubrene 100 nm at 0.047 $\mu$ J/cm <sup>2</sup> in (a) 1, (b) 5 ns window, and (c) 2 $\mu$ s window under different temperatures.....	82
Fig. 4-8 SF rates versus the reciprocal temperature.....	83
Fig. 4-9 Normalized TrPL fluorescence decay response for 20, 100, 200 nm rubrene under (a) 0.00329, (b) 0.049 (c) 136.8 (d) 1256.6 $\mu$ J / cm <sup>2</sup> excitation density in 2.0 ns window.....	85
Fig. 4-10 Normalized TrPL fluorescence decay response for 20, 100, 200 nm rubrene under (a) 0.00329, (b) 0.049 (c) 136.8 (d) 1256.6 $\mu$ J / cm <sup>2</sup> excitation density in 2.0 $\mu$ s window.....	87
Fig. 4-11 (a) $\tau_1$ and (b) $\tau_2$ values of 20, 100, and 200 nm rubrene thin films. ....	87
Fig. 4-12 Normalized TrPL fluorescence decay response for different thickness of rubrene for (a) 2 ns window, (b) 2 $\mu$ s window, (c) $\tau_2$ versus thickness and (d) schema of caging effect.....	88



## Table content

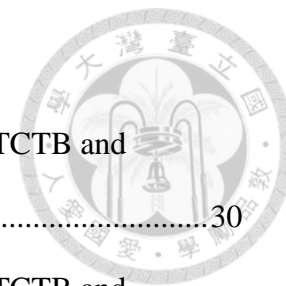


Table. 3-1 Basic characteristics of DTCPB, DTCPBO, DTCTB and DTCTBO in solution.....	30
Table. 3-2 Basic characteristics of DTCPB, DTCPBO, DTCTB and DTCTBO for thin film.....	30
Table. 3-3 Device configurations from A-1 to A-4 of DTCPB:C <sub>60</sub> OSC. The unit is nm.....	32
Table. 3-4 Performances of devices from A1 to A-4 under 1-sun solar illumination.....	33
Table. 3-5 Device configurations from A-5 to A-7 of DTCPB:C <sub>70</sub> OSC. The unit is nm.....	35
Table. 3-6 Performances of devices from A-5 to A-7 under 1-sun solar illumination.....	35
Table. 3-7 Devices configuration of devices from A-4, A-8 to A-13. The unit is nm.....	37
Table. 3-8 Performances of devices from A-4, A-8 to A-13 under 1-sun solar illumination.....	38
Table. 3-9 Device configurations for different ratio and thickness of active layer of A-7, A-14 to A-17 of DTCTB:C <sub>70</sub> based OSC. The unit is nm. ....	39
Table. 3-10 Devices performance of different mixing ratio and thickness of active layer for DTCPB/ C <sub>70</sub> based OSC.....	40
Table. 3-11 Device configurations for different blocking layers applied on champion device for DTCTB:C <sub>60</sub> based OSC. The unit is nm. ....	42
Table. 3-12 Devices performances of for different blocking layer of	

DTCTB:C60 based OSC.....	44
Table. 3-13 Device configurations for different relative ratio between mixing transporting layer from B-1 to B-7 of DTCPB based OSC. The unit is nm.....	46
Table. 3-14 Performances of device from B-1 to B-7 with various thickness of mixing layer under 1-sun solar illumination.....	48
Table. 3-15 Device configurations for different thickness and mixing ratio of active layer for devices B-10 to B-15 of DTCPB: C <sub>60</sub> based OSC. The unit is nm. ....	49
Table. 3-16 Performance of device from B-7 to B-15 with various ratio between mixing and transporting layers under 1-sun solar illumination .....	50
Table. 3-17 Device configurations of DTCPB: C <sub>70</sub> based OSC from B-16 to B-20. The unit is nm. ....	52
Table. 3-18 Performance of devices from B-16 to B-20 with various mixing ratio and thickness of active layer under 1-sun solar illumination. ....	53
Table. 3-19 Device configurations of DTCPB based OSC for different thickness of blocking layer from B-5, B-8 to B-9. The unit is nm. ....	55
Table. 3-20 Performances of device from B-5, B-8 to B-9 with various thickness of blocking layer under 1-sun solar illumination.....	55
Table. 3-21 Device configurations for different relative ratio between mixing transporting layer from C-1 to C-2 of DTCPBO based OSC. The unit is nm. ....	57
Table. 3-22 Performance of device from C-1 to C-2 with various relative ratio between mixing and transport layers under 1-sun solar illumination .....	58

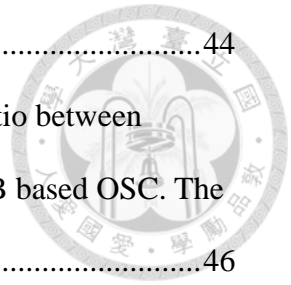
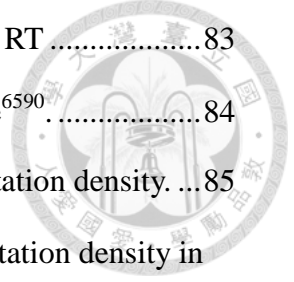


Table. 3-23 Device configurations of DTCPBO, C <sub>60</sub> based OSC for different mixing ratio from C-2 to C-8. The unit is nm.....	59
Table. 3-24 Performances of devices with different mixing ratio and different thicknesses of active layer.....	60
Table. 3-25 Device configurations of DTCPBO based OSC with different mixing ratio and thickness. The unit is nm.....	61
Table. 3-26 Performance of devices from C-9 to C-14 with various mixing ratio and thickness under 1-sun solar illumination.....	63
Table. 3-27 Device configurations of DTCTBO, C <sub>60</sub> based OSC for different mixing ratio and thickness of mixing layer from D-1 to D-6. The unit served as nm.....	65
Table. 3-28 Performances of devices with various mixing ratio and thickness of active layer under 1-sun solar illumination.....	66
Table. 3-29 Device configurations of DTCTBO, C <sub>70</sub> based OSC for different mixing ratio and thickness from D-7 to D-11. The unit is nm.....	68
Table. 3-30 Performances of devices from D-7 to D-11 with various mixing ratio and thickness under 1-sun solar illumination.....	69
Table. 3-31 Device configurations of dye for C <sub>60</sub> and C <sub>70</sub> based OSC for fine-tune mixing ratio and thickness. The unit served as nm.....	71
Table. 3-32 Performances of dye for C <sub>60</sub> and C <sub>70</sub> based OSC for fine-tune mixing ratio and thickness. The unit is nm.....	72
Table. 3-33 Slope for V <sub>OC</sub> versus natural logarithm of the light intensity...	73
Table. 4-1 Sample structures of thin films 4-1 and 4-2.....	75
Table. 4-2 $\tau_1$ of different excitation densities for 100 nm rubrene at room temperature.....	80

Table. 4-3 SF rates for different temperature from 78 K to RT .....	83
Table. 4-4 $\Delta E$ for different packing conditions of rubrene <sup>6590</sup> .....	84
Table. 4-5 $\tau_1$ for different thickness under different excitation density. ...	85
Table. 4-6 $\tau_2$ for different thickness under different excitation density in long time scale. ....	87
Table. 4-7 $\tau_2$ for different thickness of rubrene under 43 $\mu\text{J}/\text{cm}^2$ .....	88





# 1 Chapter 1 Introduction

## 1.1 Overview

In the first part of this thesis, we introduce device performances of solar cell (OSC) with four electron donor materials, 7-(5-(di-p-tolylamino)thiophen-2-yl)benzo[c][1,2,5]thiadiazole-4-carbonitrile (DTCTB), 7-(4-(di-p-tolylamino)phenyl)benzo[c][1,2,5]thiadiazole-4-carbonitrile (DTCPB), 7-(5-(di-p-tolylamino)thiophen-2-yl)benzo[c][1,2,5]oxadiazole-4-carbonitrile (DTCTBO), and 7-(4-(di-p-tolylamino)phenyl)benzo[c][1,2,5]oxadiazole-4-carbonitrile (DTCPBO). All these four electron donor materials exhibit donor-acceptor-acceptor (D-A-A) configuration. With optimization of device layer structures, OSC with DTCPB as the donor material exhibited the highest power conversion efficiency of 6.55%, with C<sub>70</sub> as the electron acceptor material. In such a device, open circuit voltage ( $V_{OC}$ ), short circuit current density ( $J_{SC}$ ) and fill factor (FF) are 0.90 V, 11.12 mA/cm<sup>2</sup>, and 65.63%, respectively.

In the second part of this thesis, exciton dynamics for 5, 6, 11, 12-tetraphenyltetracene (rubrene) in different thickness were studied by transient photoluminescence (TrPL) measurement with varying pumping intensity and sample temperature. Under low temperature (78 K) and pumping intensity (0.049  $\mu\text{J}/\text{cm}^2$ ), fission and fusion dynamics can be obtained without singlet-singlet annihilation (SSA). With low excitation (no SSA) at different temperature, the activation energy of singlet fission (SF) was measured. We also found that the thinner rubrene (5 nm)

exhibited higher fusion rate, which may result from higher probability for non-germinate recombination. Such phenomenon was also observed when increasing the input power to the thicker film (100 nm rubrene at  $43.4 \mu\text{J}/\text{cm}^2$ ).

In this chapter, we will introduce the operation principle, device structure, D-A-A molecule system, and recombination mechanism of OSC. Then, physical mechanism of singlet fission (SF) will be introduced. Caging effect, which was observed in our experiments, will be illustrated. Then, exciton dynamics of pentacene and tetracene-based molecules were reviewed.

## 1.2 Small molecule organic solar cells

### 1.2.1 Introduction of OSC

Solar cell technology provides clean and renewable energy which converts the optical power (mainly from sun) to electric power and has attracted lots of attentions<sup>1,2</sup>. OSC, including macromolecule (polymer) and small molecule<sup>3,4</sup>, has advantages of low production cost, light weight and large fabrication area in consumer market comparing to the inorganic solar cells<sup>5,6</sup>.

A milestone for OSC was proposed in 1985, by C. W. Tang<sup>7</sup> et al. By using two organic materials, copper phthalocyanine (CuPc) and perylenetetracarboxylic derivative (PV) as donor and acceptor materials, respectively, it was possible to achieve power conversion efficiency up to 1% under AM2.0 illumination<sup>8</sup>. In 1992, an evidence for photo-induced charge transfer between a conducting polymer and buckminsterfullerene was claimed by F. Wudl<sup>9,10,11</sup> et al. Such fullerene derivatives, C<sub>60</sub> and C<sub>70</sub>, were efficient electron acceptor materials, while the quantum yields in C<sub>70</sub> were higher than C<sub>60</sub> under the measurement of transient absorption<sup>12</sup>. Fig. 1-1 shows the operation principle of an OSC. First, (1) incident photons excite the

molecules to generate the singlet excitons, which are mainly the Frenkel excitons in active layer; (2) then, the excitons diffuse randomly inside the cell and reach D/A interface; (3) electron-hole pairs are generated from excitons are dissociation by built-in potential and (4) finally, electron and holes transport via acceptor and donor materials which are collected by the electrodes<sup>13</sup>.

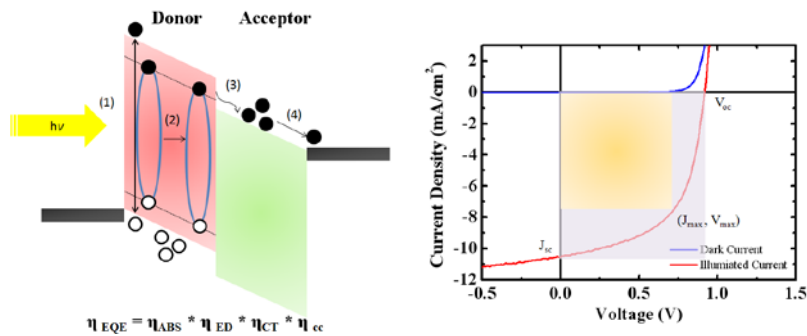


Fig. 1-1 (a) Operation principle and (b) J-V characteristic of an OSC.

There are several parameters which can be extracted from a typical J-V characteristic under light illumination, as shown in Fig. 1 (b). Open circuit voltage ( $V_{OC}$ ) is defined as the voltage at zero current density, related to the energy offset between the highest occupied molecular orbital (HOMO) of donor and the lowest unoccupied molecular orbital (LUMO) of acceptor. The short circuit current ( $J_{SC}$ ) represents the current under the zero applied bias, which can be improved with the use of small band-gap organic material. Along the J-V characteristics, one can find a point which delivers maximum electrical power, with voltage and current density at  $V_{mp}$  and  $J_{mp}$ , respectively. Fill factor (FF) corresponds to the area ratio between multiplication of  $V_{mp} \times J_{mp}$  and  $V_{OC} \times J_{SC}$ . This important parameter is closely related to series resistance ( $R_s$ ) and shunt resistance ( $R_{sh}$ ), which are the mainly determined by carrier mobility and leakage recombination, respectively. The final efficiency (PCE) can be calculated as the multiplication for  $J_{SC}$ ,  $V_{OC}$  and FF.

## 1.2.2 Bulk heterojunction configuration<sup>14</sup>

Exciton dissociation of OSC was achieved by D-A interface, which provides the potential to overcome the strongly binding energy of the exciton (e.g., ~0.3–0.5 eV)<sup>15,18</sup>. Mixing of donor and acceptor materials can effectively improve exciton dissociation<sup>16</sup>. It was first given by M. Hiramoto et al. in 1992. They applied a p-i-n structure which i-layer was constructed by mixing p-type phthalocyanine (PC) and n-type perylene derivative (PTC). This three-layer OSC doubled the photo-generate-current compared to the two layer ones<sup>17</sup>. In 2000, T. Tsuzuki et al. doped the titanylphthalocyanine (TiOPc) with a fullerene (C<sub>60</sub>) and achieved a PCE of 0.63%.<sup>18</sup> In 2003, D. Gebeyehu et al. blended zinc-phthalocyanine (ZnPc) as electron donor and C<sub>60</sub> as electron acceptor to raise the efficiency to 1.04% with a proper transporting layer<sup>19</sup>. The mixing ratio of donor and acceptor materials strongly impacted the performance. But this p-i-n architecture limited the thickness of the mix layer in the middle due to the poor carrier collection efficiency within 30 nm. As shown by S. Uchida et al. in 2004,<sup>20</sup> with a traditional organic materials copper phthalocyanine (CuPc) blending with C<sub>60</sub>, the PCE can be as high as 3.6%, 3.5% and 3.3% under 0.3, 1 and 2.4 suns, respectively which showed the recombination limited behaviors.

In 2014, Y. Zou et al. used a simple bulk heterojunction for OSC to boost up the efficiency to 7.9%<sup>21</sup>. The active region of the OSC consisted of a mixed layer with 2-{[7-(4-N,N-ditolylaminophenyl-1-yl)-2,1,3-benzothiadiazol-4-yl]methylene} malonitrile (DTDCPB) as electron donor material and fullerene C<sub>70</sub> as the electron acceptor material, respectively. DTDCPB is a donor material with the molecular configuration of donor-acceptor-acceptor (D-A-A). As shown in Fig. 2 (a), the active region was sandwiched by neat donor and acceptor materials, which is called planar



mixed heterojunction (PMHJ) structure. The neat donor and acceptor in Fig. 2 (a) can be replaced by a high mobility buffer layer  $\text{MoO}_x$  in Fig. 2 (b) which reduced the resistance of the cell. This architecture can effectively reduce the non-geminate recombination for electrons and holes on the interfaces of the planar layers that usually happened in PMHJ-OSC and led a high fill factor over 0.65.

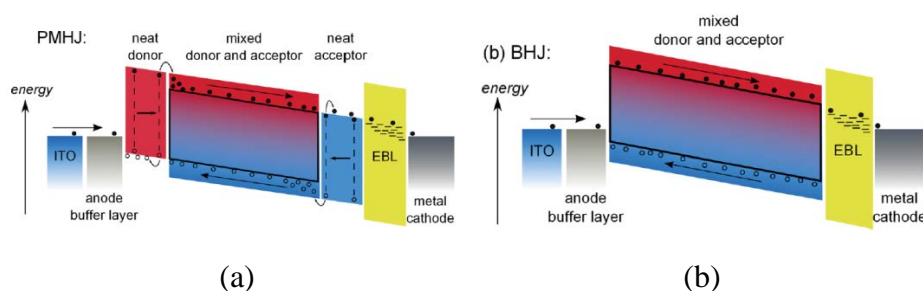


Fig. 1-2 Comparison between planar mixed heterojunction and bulk heterojunction OSCs<sup>21</sup>

### 1.2.3 D-A-A system organic materials

In this section, we will introduce the donor materials with asymmetric donor-acceptor-acceptor (D-A-A) configurations<sup>22</sup>. The concept of D-A-A systems originally came from the configuration D- $\pi$ -A which was used to in the dye-sensitizers solar cell<sup>23,24</sup>. Maintaining the advantages for strong benzothiadiazole moiety and quinoid character, an inceptive compound 2- $\{[7-(5-N,N$ -ditolylaminothiophen-2-yl)-2,1,3-benzothiadiazol-4-yl]methylene\}malononitrile (DTDCTB) was synthesized and PCE up to 5.81% was obtained<sup>25</sup>. Then, 2- $\{[7-(4-N,N$ -ditolylaminophenyl-1-yl)-2,1,3-benzothiadiazol-4-yl]methylene\}malononitrile (DTDCPB), which replaced the thiophene groups by phenylene, showed a higher PCE for 6.8%<sup>26</sup>. From the electron donor endcap architecture, the electron-rich

and fortified quinoidal characters of thiophene functional groups of DTDCTB resulted in the redshift (50-70 nm) in absorption spectra, compared to phenylene attached molecules, DTDCPB. It increased the  $J_{SC}$  of DTDCTB-based OSC, compared to DTDCPB-one. This was not only due to the packing of the molecular which laid for a coplanar conformation between the thiophene and BT rings with a small dihedral angle in comparison with phenylene (with ortho-ortho steric interactions by single crystal X-ray crystallography) but also the support electron-rich of thiophene for better  $\pi$ -electron delocalization as shown in Fig. 1-3. However, owing to the electron-rich nature of thiophene of DTDCTB, it showed a smaller oxidation potential than phenylene-containing molecule (DTDCPB) and resulted in a lower  $V_{OC}$ , and hence PCE. When replacing the p-tolyl substituent of DTDCPB into hydrogen bond, 2-[[7-(4-N,N-diphenylaminophenyl)-2,1,3-benzothiadiazol-4-yl]methylene]malononitrile (DPDCPB) exhibited a higher oxidation potential which resulted in a better  $V_{OC}$ . And it resulted in the blue shift of absorption spectra and hence lower  $J_{SC}$ . Compromising the  $J_{SC}$  and  $V_{OC}$ , DTDCPB exhibited the highest PCE=6.8%<sup>27</sup>.

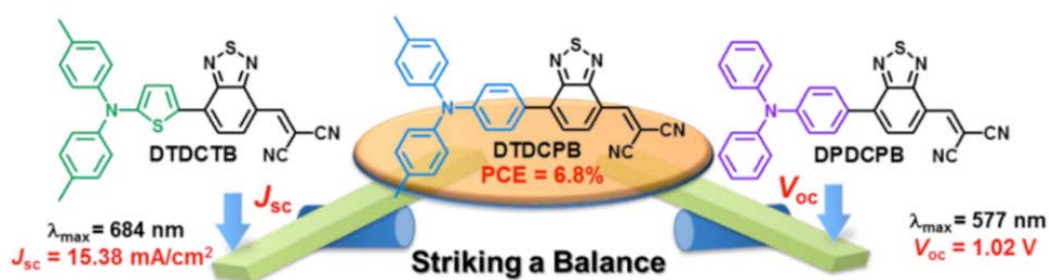


Fig. 1-3 Striking a balance between  $J_{SC}$  and  $V_{OC}$ <sup>26</sup>

Further, a substitution for benzochalcogenodiazole unit was also possible to adjust the photophysical properties as shown in Fig. 1-4. Here, 2,1,3-benzoxadiazole (BO) was adopted as the central bridging acceptor of DTDCPBO, which resulted in red shift of absorption spectra ~10 nm compared to 2,1,3-benzothiadiazole (BT)

bridged molecules, DTDCTBO, due to a larger electronegativity of the oxygen atom and a lower HOMO level, owing to the decrement of the energy for frontier orbital<sup>28</sup>. However, although OSC devices based on BO materials exhibited longer absorption spectra and higher  $J_{SC}$ , the FF was lower due to more serious bimolecular recombination, compared to those based on BT ones.

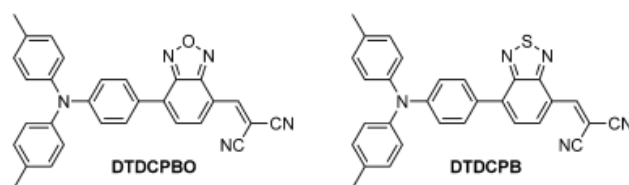


Fig. 1-4 Molecular structures of the D-A-A electron donor materials with BO and BT moieties.

#### 1.2.4 Recombination mechanisms of OSC

There are mainly two basic recombination routes in OSCs<sup>29,30</sup>: geminate and nongeminate (bimolecular) pair recombination. For the first-order geminate loss, recombination happens before it splits into charge. It is population independent because it is only driven by coulomb attraction. After the exciton bonding pair is totally dissociated, there is still possible for carriers to encounter (collide) and meet each other before they are collected by electrodes, which is called bimolecular recombination. This loss depends on the populations of carriers. It is noted that bimolecular recombination is likely to happen via reformation of interfacial charge transfer states. Typically, recombination mechanisms were studied by transient photoconductivity<sup>31</sup>, time-of-flight<sup>32</sup>. Besides, it can be investigated by light intensity dependent measurement<sup>33</sup>.

Eq. 1 illustrates the relation between  $V_{OC}$  and  $J_{SC}$ . Here,  $n$  and  $J_{OL}$  are the ideal factor and the leakage current, respectively. Typically,  $n$  equals to 1 for the ideal diode and falls on 1.0-2.0 for OSCs. For an OSC dominated by bimolecular recombination,  $n$  is 1.0. On the other hand, trap assisted Shockley-Read-Hall (SRH) recombination resulted in  $n=2$ .

$$V_{oc} = \frac{nkT}{q} \ln \frac{J_{sc}}{J_{OL}} \quad (1)$$

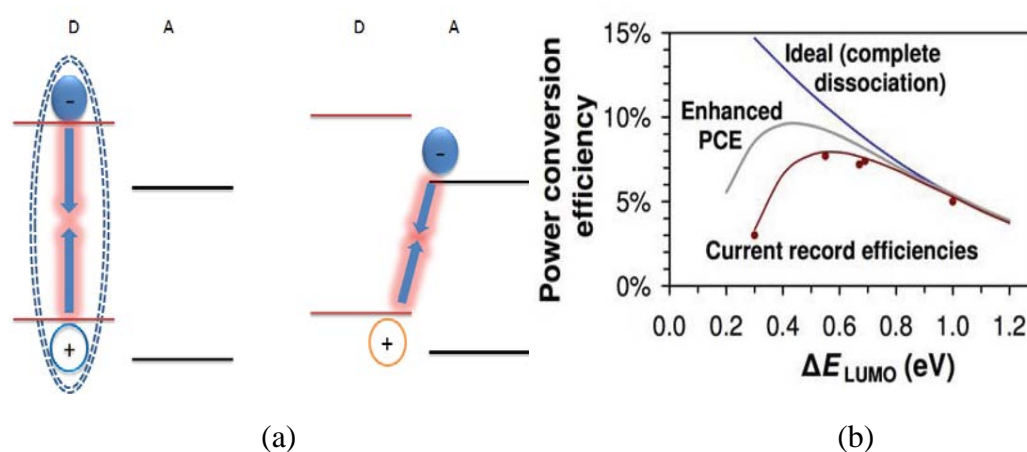


Fig. 1-5 (a) Germinate and non-germinate recombination. (b) Trade-off between  $\Delta E_{LUMO}$  and PCE<sup>34</sup>.

The lowest unoccupied molecule orbital (LUMO) energy offset between donor and acceptor,  $\Delta E_{LUMO}$ , also take place in germinate pair dissociation here<sup>34</sup>. This offset will not only play an important role in charge transfer (CT), but also attribute to free carriers dynamics. Literatures had been report that a higher  $\Delta E_{LUMO}$  (>1 eV) resulted to a better electric properties for a promotion in FF and quantum efficiency<sup>35</sup> compared to a modest one (0.2-0.3 eV). Note that this is valid when the donor material is the main absorber. On the other hand, when the acceptor material is the main absorber,  $\Delta E_{HOMO}$  is the dominating factor. Anyway, this offset will oppositely

expend too much exciton energy during dissociation if the value lying too high, so the trade-off between for its limitation is shown in Fig. 1-5 (b).. This difference can also relative to the charge energetic driving force for separation  $\Delta G_{CS}=E_g - (IP_D - EA_A)$ , which shows a charge separation dependence  $(\sim\Delta E_{LUMO})^{36}$  by providing a 40%/eV enhancement in charge collection efficiency<sup>37</sup>.  $IP_D$  and  $EA_A$  represented to an ionized potential and electron affinity for donor and acceptor, respectively.

## 1.3 Singlet fission

### 1.3.1 Introduction

In a single junction solar cell, only photons with the energy above the band gap can be absorbed and contribute to  $J_{SC}$ , which means band gap should be as small as possible for higher  $J_{SC}$ . On the other hand, for a photon with higher energy than bandgap, it generate a high energy electron-hole pair, which losses the energy via heat to the bandgap and extract out the solar cell. Hence, the bandgap determines  $V_{OC}$ . Larger bandgap is needed for higher  $V_{OC}$  and shows a tradeoff with  $J_{SC}$ , which is called the Schlocky Queasier (SQ) limit<sup>38</sup> as shown in Fig. 1-6. One way to overpass the SQ limit is by using multi-exciton generation (MEG) and multi-carrier generation (MCG). By using a narrow bandgap material ( $V_{OC}$  is limited), however, one high energy photon can generate more than one exciton (carrier) and greatly improve the  $J_{SC}$  value. Such phenomenon was found in several materials, such as quantum dot<sup>39</sup>, carbon nanotube<sup>40</sup>, indirect-band gap semiconductor<sup>41,42</sup> and organic materials<sup>43,44</sup>. In this thesis, we will focus on the MEG in organic material. By splitting one singlet exciton into two triplet exciton, which is called singlet fission (SF), it shows the possibility to obtain a high internal quantum efficiency over 100%<sup>45,46,47,48,49</sup>.

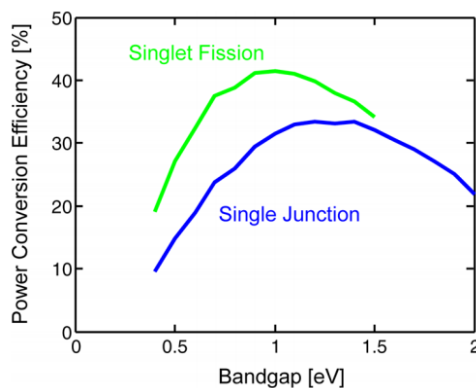


Fig. 1-6 Shockley Queisser (SQ) limit for single junction solar cell<sup>51</sup>.

For archetypal polyacene based materials, early in 1965, S. Singh et al. observed the prompt- and delayed-fluorescence under short-pulse laser excitation from anthracene single crystal. Here, the authors claimed that the prompt-fluorescence came from the singlet emission, while the delayed-one may involve triplet states<sup>50</sup>. In 1968, C. E. Swenberg et al. proposed the possibility of SF to explain the low quantum yield of tetracene (0.002 in room temperature)<sup>51</sup>. In the same year, N. Geacintov et al. observed the fluorescence increase of tetracene crystal under a magnetic field, due to lower SF rate<sup>52</sup>. Besides, they also found that the activation energy of tetracene was around 0.16 eV by temperature-dependent measurement. In 1969, R. P. Groff et al. obtained the fission and fusion rates of  $0.63 \text{ ns}^{-1}$  and  $9 \times 10^{-10} \text{ cm}^3 \text{ s}^{-1}$  in tetracene crystal<sup>53</sup>.

SF is a physical phenomenon that occurs in certain organic materials, especially in the aromatic hydro base materials<sup>54,55,56,57,58</sup>. For SF, energy for one singlet exciton must be as about double as its energy for triplet exciton. The operation principle is shown as in Fig. 1-7 When one chromophore is excited by an incident photon and jumps to an excited state (generating one singlet exciton, spin=0), it is possible to share the energy to its nearby chromophore (if close enough) and split into two independent triplet excitons (spin=1) with the energy around half. In SF process,

energy and spin are conserved. If the two triplet excitons can be dissociated completely into free carriers, it hinders that two electron-hole pair can be generated by just a single photon so the internal quantum efficiency will be 200% theoretically. Such exciton dynamics can be observed by transient photoluminescence (TrPL) measurement. Delayed fluorescence in TrPL comes from the singlet excitons generated by two triplet excitons (which is called the fusion process), due to the long lifetime of the triplet exciton ( $\mu\text{s}$ ) compared to singlet one (ns).

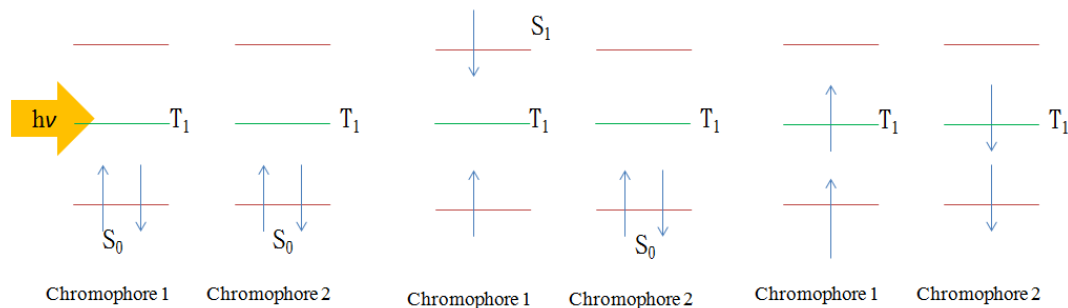


Fig. 1-7 Operation principles for singlet fission.

### 1.3.2 Exciton dynamics of aromatic based materials

In this section, we will introduce some important researches on excitonic photochemistry of aromatic hydrocarbon materials (ex: tetracene and anthracene). An ultrafast SF rate for 80 fs in polycrystalline pentacene was demonstrated by M. W. Wilson et al., which competed with phonon-mediated exciton localization processes<sup>59</sup>. On the other hand, SF rate was 80 ps in polycrystalline tetracene<sup>60</sup>. For the sublimed rubrene film, SF process competed with the formation of polaron pair which resulted in a fast decay of 2.5 ps, and delay fluorescence was strongly dependent to laser excitation<sup>61</sup>. The SF rate of hexacene, a six-ring acene, was 0.19 ps. Singlet exciton can split into three triplets in such a material<sup>69</sup>. Besides, there are lots of tetracene and

pentacene derivatives exhibiting SF characteristics, due to their favorable molecular packing<sup>70,62</sup>.

Due to strongly  $\pi$  stacking in tetracene, tetracene molecules tends to crystallize under room temperature which forms excimer and compete with SF process. On the other hand, the four phenyl groups of rubrene helps to separate the molecules apart and reduce excimer formation<sup>63,64</sup>. As shown in Fig. 1-8 (a), TrPL of rubrene thin film is quite different under 77 K and 298 K in the 20 ns window. At 298 K, intensity decreased fast due to strong SF process. On the other hand, single exponential slow decay was observed under 77 K, which suggested that such SF in rubrene thin film was a thermally activated process, as shown in Fig. 1-8 (a). For SF process, singlet exciton underwent a dark state (2T state, which is optical forbidden) before split into two triplets. And hence, thermal energy was needed to overcome the energy offset between S and 2T. For example,  $[2E(T_1) - E(S_1)]$  values of tetracene, rubrene solution, single-crystal rubrene, DPT (5, 12-diphenyl tetracene), and pentacene are 190 meV<sup>65</sup>, -12 meV<sup>65</sup>, 50 meV<sup>66,89</sup>, -87 meV<sup>67</sup>, and -0.11 eV, respectively.

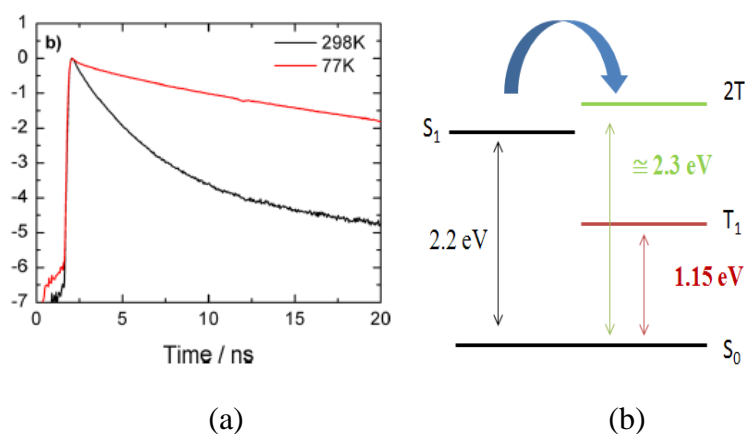


Fig. 1-8 (a) TrPL at 77 and 298 K<sup>64</sup> and (b) energy diagrams of rubrene thin film.

Magnetic field effect gives more powerful evidence into exciton dynamics under



SF process. Nine triplet states under magnetic field will be rearranged, which reduces the SF rate<sup>68</sup>. Fig. 1-9 (a) shows photocurrent of an OSC with increasing magnetic field<sup>69</sup>. When the strong magnetic field applied to a pentacene base OSC, the allow state decreases from nine to three to suppress the SF rate and decreases the photocurrent from SF. When increasing the magnetic field,  $J_{SC}$  resulting from tetracene reduces due to the suppression of SF under magnetic field while that from  $C_{60}$  keeps the same because it is insensitive to the magnetic field. Fig. 1-9 (b) shows the TrPL of rubrene thin films. One can see that magnetic field reduced the SF process, and hence increased the optical intensity.

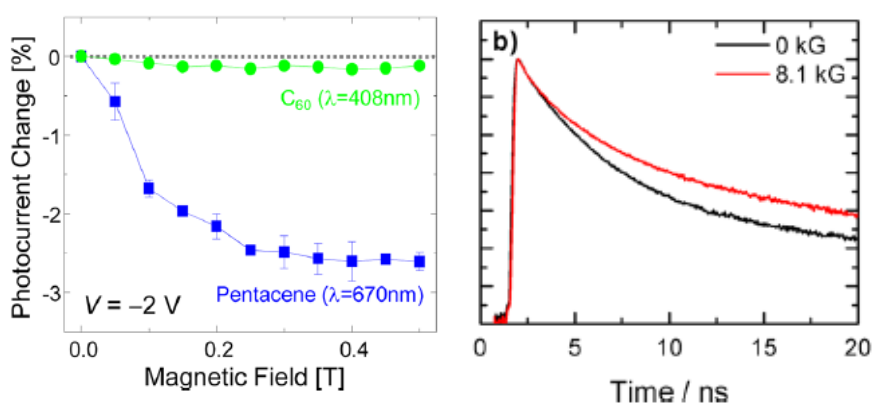


Fig. 1-9 Magnetic field effect on (a) pentacene based OSC<sup>69</sup> and (b) rubrene thin film<sup>64</sup>

For single crystal rubrene, L. Ma et al. found the triplet exciton formation on the time scale of 200 fs while intersystem cross channel can be neglected ( $<0.05\%$ )<sup>70</sup>. Observed by A. Ryasnyanskiy et al., SF and triplet fusion rates are very high. And the triplet lifetime is about  $100\ \mu\text{s}$ <sup>71</sup>. For X. Wen et al., they investigated the singlet and triplet dynamics under different vibration band, and an ultrafast characteristic for carrier scattering and phonon scattering within 100 fs and 47 ps was observed, respectively<sup>72</sup>.

### 1.3.3 Caging effect

Caging effect, a diffusion-mediated<sup>73</sup> process, was first observed in solution. Early in 1936, Frank and Rabinowitch tried to explain the reason for different germinate recombination rates in iodine atoms dissociated from excited I<sub>2</sub> in solution compared to the gas phase<sup>74,75</sup>. After, cage effect was defined<sup>76</sup>: for a molecular under a densely condition, gas or solution<sup>77</sup>, molecules are hard to interact or diffuse due to the surrounding solvent molecules. Reactance species acted as caged by the solvent molecules and this effect relied on the radical radius and radical mass of the solvent<sup>78</sup>, which was also known as the Franck–Rabinowitch effect.

There are some techniques to perform a ‘cage’ by a small volume confinement spacing design. One can grow small crystallite inside frozen glasses<sup>79</sup>, one dimension plasma<sup>80</sup> or by an incomplete thermal evaporation on a suitable substrate to form molecular islands. The motivation is to diminish the crystal size in which exciton is free to move. Caging effect is more significant in anisotropic materials such as tetracene and anthracene. Exciton in these kinds of materials will be restricted to a given plane, for example, ab plane for tetracene<sup>81</sup>. For SF materials, triplet-triplet (T-T) annihilation rate will depend on the concentration of exciton and the volume of the thin film domain.

An experiment was performed by S. Arnold et al. in 1975<sup>82,83</sup>. They mixed the host material tetracene (the source of triplet exciton) into a high concentration of guest exciton reflecting molecules, 2, 3-benzocarbazole (BC). This skill had been performed by Hichestrasser and Whiteman to exhibit a “one dimension” crystal<sup>84</sup>. If the exciton caging can be formed, the triplet concentration of tetracene should be high enough to produce a non-germinate (bimolecular) recombination than neat films (no caging) even at a low prompt intensity. By varying the containment of BC, a

consequent for caging effect can be observed. As shown in Fig. 1-10, the fluorescence lifetime increase from 100 ps to 360 ps by varying the BC concentration from 0% to 50% implied that the caging effect became serious and blocked the SF channel which increased radiative lifetime.

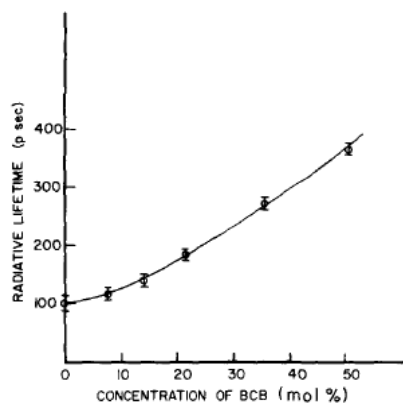


Fig. 1-10 Radiative lifetime of tetracene with various concentration of BC<sup>82</sup>.

## 1.4 Motivation

There are two parts in this dissertation. First, four small molecule donor material with D-A-A structure configuration were employed in organic solar cells.

Compared to our previous works, end acceptor of these materials were modified from dicyanoethylene into single cyano group<sup>85</sup>. The HOMO levels were higher lying for triggering the charge transfer and separation state. Besides, the thermal properties of these materials were being improved. These four materials were provided by Dr. Hao-Chun Ting and Prof. Keng-Tsung Wong's group, Department of Chemistry, National Taiwan University. To pursuing a high efficiency, a series of optimization in OSCs were taken with bulk heterojunction structure.

Second, exciton dynamics of amorphous rubrene thin film with different thicknesses was studied under different temperature and excitation energy by TrPL, supported by Dr. Juen-Kai Wang, Center for Condensed Matter Sciences, NTU, and Institute of Atomic and Molecular Sciences, Academia Sinica. A rate equation was

used to explain the dynamics and the parameters (such singlet fission rate, triplet fusion rate, singlet-singlet annihilation rate...) was quantitatively extracted from our TrPL results.



## 2 Chapter 2 Experiments



### 2.1 Introduction

In this chapter, all the fabrication and measurement systems in this thesis will be introduced.

Thin-film structures for OSC and SF studies in this thesis we obtained by thermal evaporator under high vacuum. Suitable patterning and treatments were applied before the thin-film process. And the encapsulation process was performed directly after the thin-film evaporation.

For OSC thin-film and devices, J-V characteristics under dark and 1-sun illumination was performed for calculating device performances such as  $V_{OC}$ ,  $J_{SC}$ ,  $R_s$ ,  $R_{sh}$ , FF, and PCE. Recombination mechanism in our OSCs was studied by varying the illumination intensity of solar simulator. External quantum efficiency and absorption spectra were measured and hence internal quantum efficiency can be obtained. Besides, photoelectron spectroscopy and ellipsometry measurements were performed for the energy levels and optical constants of organic thin-films, respectively.

In our SF study, transient trPL was used with various laser pulse energy under different sample temperatures (77K to room temperature).

### 2.2 Device fabrication and measurement systems for OSC

#### 2.2.1 Substrate patterning

Glass substrates with 150-nm indium tin oxide (ITO) were used (Lumtec Corporation, resistance 15  $\Omega$ /square). ITO pattern was obtained through

photolithography and etching processes in the clean room.

First we cleaned the substrates by detergent (DI water with detergent 10:1), acetone and isopropyl alcohol (IPA) consecutively each for 10 min and dried it with nitrogen gun. Then spin the positive photoresist (PR, S1813) on the substrates with two different rotation speed and time (550 and 1250 rpm for 5 and 25 sec respectively). followed by 10 min hard-bake to solidify the film. UV exposure (for 13 sec with photo masks followed by developine process (MF 319) for 13 sec was used to obtain the PR pattern. After that, soft bake was applied by remove the redundant vapor. Then, aqua regia (mixed by HCl: HNO<sub>3</sub>= 3:1) was used to etch the ITO without PR. Finally, acetone was used to remove the PR in the substrate. Then, patterned substrates were cut into 1.78 × 2.78 cm<sup>2</sup> for the following processes.

### **2.2.2 Device fabrication**

All the devices were fabricated in the thermal evaporate system under a high vacuum ( $1 \times 10^{-6}$  torr) which included 7 thermal cells for small molecule organic materials and 3 boat for metal and C<sub>60</sub>. Evaporation rates for materials were monitored (Mextek 350, 400) by the sense of quartz crystal microbalance (QCM). With proper shadow masks for both organic materials and metal, active region can be defined for 0.04 cm<sup>2</sup> which contained three pixels on a substrate. Samples were then transferred to a 99.999% (5N) N<sub>2</sub> glove box with the concentration of O<sub>2</sub> and H<sub>2</sub>O below 0.1 ppm. After spreading the UV glues at the peripherals of the cover glass and attaching it with the thin-film substrates, samples were illuminated by UV lamp for 12 minutes to solidify the UV glues. Such encapsulation provided reliable storage lifetime at least over two weeks.

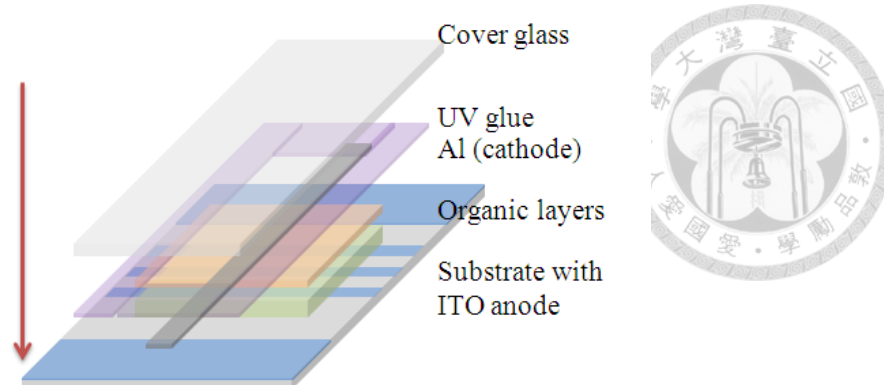


Fig. 2-1 Device configurations.

### 2.2.3 Device performances measurement

In device performances measurement, OSCs were illuminated by a class-A solar simulator (Newport Model 94022a) under a standard condition (1-sun,  $100 \text{ mW/cm}^2$ , air mass (AM) 1.5G) as shown in Fig. 2-2. The solar simulator was calibrated regularly to prevent from the decay of the lamp (155W) with measuring distance of 2.5 inches. Hence, uniform illumination region with precise illuminance can be achieved. Manual shutter was used when measuring the dark current of the OSCs, which were connected to power meter (Keithley 2400). A computer was used to control the power meter via GIPB interface for obtaining the J-V characteristics and analyzing the device parameters such as  $V_{OC}$ ,  $J_{SC}$ ,  $R_s$ ,  $R_{SH}$ , FF and PCE. The solar simulator system is supported by Prof. Tien-Lung Chiu in Yuan Ze University, Taoyuan Taiwan.

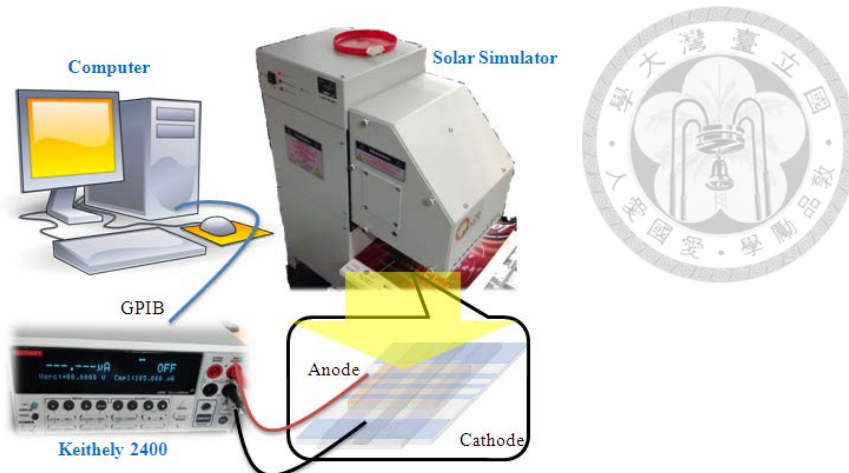


Fig. 2-2 Set up of device performances measurement.

## 2.2.4 Measurement of external quantum efficiency (EQE)

Setup of EQE measurement was shown in Fig. 2-3. A halogen light source (Newport Model 66901) supported by power supply (Newport Model 69907) gave a continuous white light source which passed the monochromator (Oriel Conerstone130 1/8m) with a precise grating working for 200-1200 nm. Then it passed through a chopper with the rotation speed 350 Hz, controlled by a chopper controller (Stanford Research system SR540) which connected with lock-in amplifier (SR-830) to eliminate the noise from environment. After that a filter wheel (Newport 74040) was constructed to cancel the 2nd diffraction from grating in monochromator. A silicon photodiode was employed to calibrate the input photon density (count the photon number). Then the photocurrent was measured by lock-in amplifier (count the numbers of electron) and sent the information to computer via GPIB interface and the software was provided by Forter Technology Corporation. EQE spectra can obtained by the ratio between photon and electron numbers.



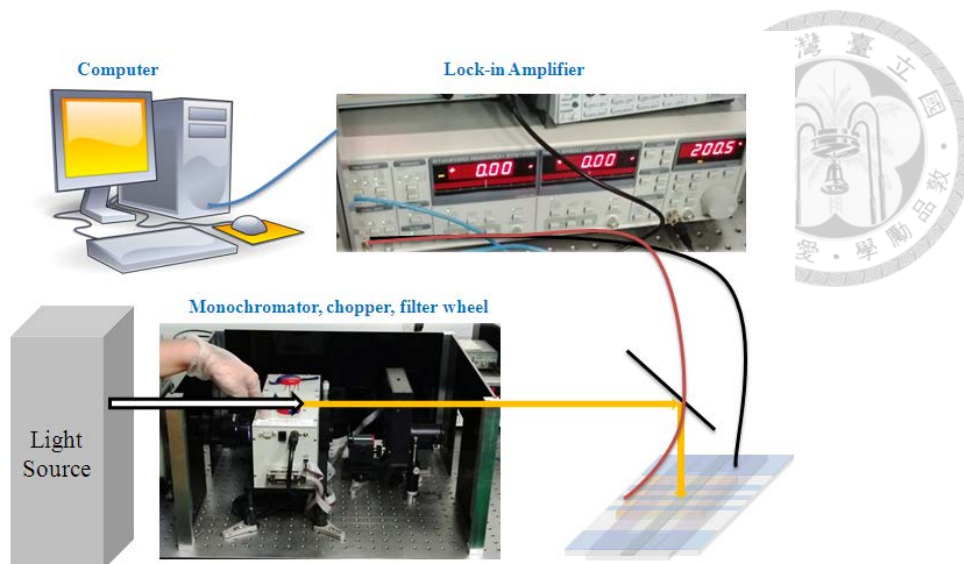


Fig. 2-3 Set up of EQE measurement.

### 2.2.5 Absorption spectrum measurement

To gain the value for internal quantum efficiency (IQE), we have to measure the absorption spectra for the devices. A commercial spectrometer U4100 by Hitachi was employed and gives a wide range for absorption measurement from 240 nm to 2600 nm. Due to the zero transmission of metal cathode in OSC devices, we can obtain the absorption spectra from reflection spectra. And IQE spectrum can be achieved by using the EQE spectrum dividing the value for absorption spectrum from the equation below. The spectrometer were supported by Man-Kit Leung's Lab in Chemistry Department of National Taiwan University.

$$\frac{\text{EQE}(\%)}{\text{abs}(\%)} = \text{IQE}(\%) \dots \dots \dots (2)$$

### 2.2.6 Measurement of optical constants

We can realize the optical characteristic and packing situation for molecules under the measurement of ellipsometry. In this research, a variable incident angle ellipsometry SOPRA GES5 (Gonio-Ellipso-Spectro-Photometer) which was support by Radiation Technology was employed, shown in Fig. 2-4. For ellipsometry system,

we detected the elliptically polarized reflect light from the dielectric organic thin film by input a plane polarized beam. With extracting the information for amplitude and phase of the polarization from neat film which were deposited on the n-type silicon substrate with reflection mode, we can simulate and scan by these data then get the values for anisotropic refractive index and extinction coefficient accurately in scanning mode, without destroyed the thin film morphology. This variable angle goniometer constructed by an analyzer and polarizer (Xe lamp include) arm, which can be mounted by stepper meter and high-resolution monochromator, photon counting detector is contained. During the scan, the detected signal were collected into a optical fiber which connected to a monochromator.

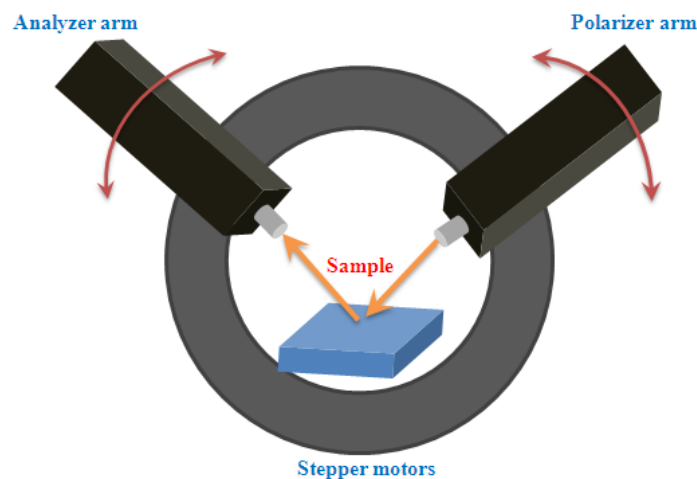


Fig. 2-4 Set up of variable incident angle ellipsometry

### 2.2.7 Sun variation system

A sun variation experiment is powerful to give the standpoint for exciton and carrier behavior because a power dependent can separate the recombination between exciton and charges. The system is built as shown in Fig. 2-5. A Wacom light source for radiative parallel luminous of high luminous (Wacom HX-504) with a tunable input current supported (Wacom XDS-501SG) had ability for varied the incident

power from 0.001 to over 1sun.

The value of sun can be accurately measured and calibrated by a silicon diode (Model 99150 V). By tuning the wanted sun value detected by reference cell, our solar cells were replaced on the holder. All the measurements were taken under the dark room to preventing the noise from the environment, especially under low intensity measurement. And to avoid the thermal formation during the measurement, each test will place over 1 min to cool down when the measurement is too frequently. The system is also supported by Prof. Tian Lung Chiu in Yuan Ze University, Taoyuan Taiwan

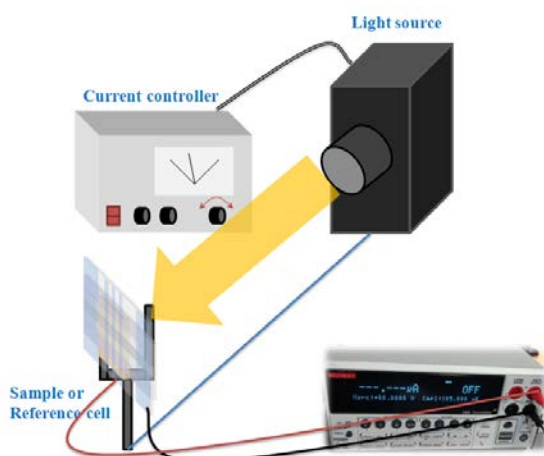


Fig. 2-5 Set up of Sun variation system

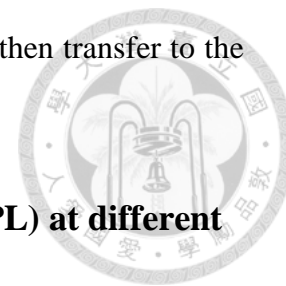
## 2.3 Sample fabrication and measurement systems for exciton

### dynamics

#### 2.3.1 Samples fabricated for exciton dynamic investigation

All the samples were fabricated under the same evaporation system as mentioned in section 2.2.2. Rubrene and LiF thin film were deposited on the quartz and glass substrates under high vacuum, which the quartz purity over 99.99% and the

transmission also greater than 95% in visible region. The samples then transfer to the nitrogen glove box to seal it with UV glues.



### **2.3 2 Steady state and time-resolve photoluminescence (TrPL) at different temperatures**

In this research, exciton dynamic was studied by the measurement of steady state photoluminescence and TrPL. The system is established and supported by Dr. Pin-Hao Sher from Prof. Juen-Kai Wang's group in Institute of Atomic and Molecular Sciences, Academia Sinica, Taiwan and the detail construction was shown in Fig. 2- 6.

A Nd:VAN (High Q IC-1064-15000) laser source with 1064 nm emission wavelength was employed in this research. Laser pulsewidth was 6.5 ps in full width at half maximum (FWHM) with its origin repetition rate 76 MHz. The pulse passed through a second harmonic generation (SHG) crystal which generated 532 nm pulses. Then the radio frequency (RF) acoustic pulse selector changed the repetition rate by producing a periodic wave grating to reflect the unwanted pulses. The repetition rate we chose was 170 kHz. A first 4X lens and aperture served the function of space filter to eliminate the frequency noise from the light source. A combination for half wave plate and broad band polarizer (SM1PM10) was used to vary the input intensity.

By using the power meter diode (818-UV) and optical power meter (1916C, Newport) before the microscope, an accurate intensity density (in terms of W) can be measured. It can monitor and focus the sample by microscope (Olympus BX61W1) in front of sample. After passing the long pass filter, the reflecting fluorescence signal coming from samples went through the same path and back to the detector. To detect the signal, one can obtain the steady state behavior by detecting the signals with Charge-coupled Device (CCD) (Andor DU920P BR-DD) or transient characteristic by Time-Correlated Single Photon Counting (TCSPC) system with reverse mode to delay

the time, all the fluorescence was collected by monochromator (Horiba Jobin Yvon MicroHR).

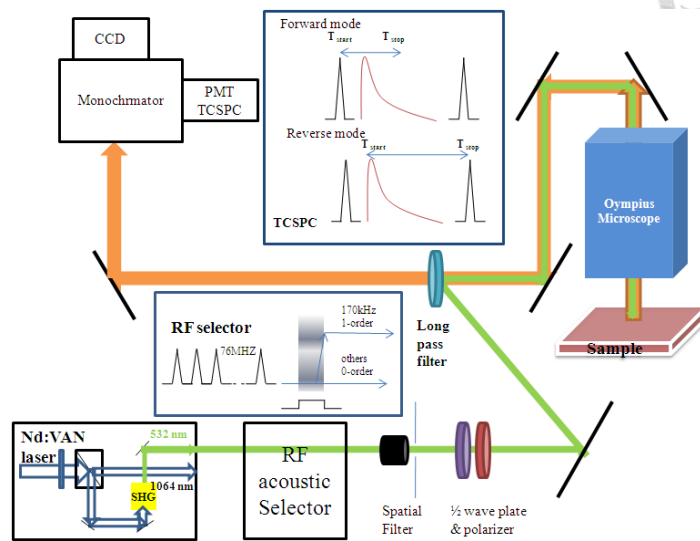


Fig. 2-6 Set up of steady state and time-resolve photoluminescence (TrPL)

In our measurement, samples were mounted on a stage with temperature control system from 77K to room temperature. Here, samples attached to the special cryo carrier (Cryo industries CFM 1738-X6M102, 5119) as illustrated in Fig. 2-7. To provide a better thermal conduction, silver glue was applied between copper holder in cryo carrier and samples. The base pressure of the measurement chamber is  $1 \times 10^{-5}$  by turbo pump (Varian vacuum tec TPS-compact). Liquid nitrogen was used to cool down the system to 77 K. Under the temperature controller (Lakeshore 331), the heater can control the temperature in carrier.

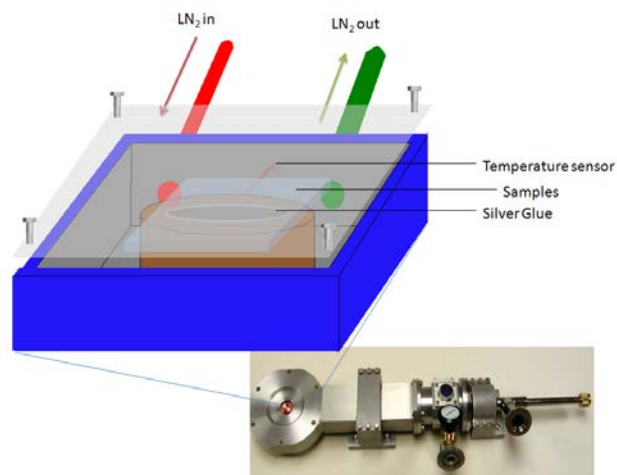


Fig. 2-7 Temperature-controlled sample holder.



### **3 Chapter 3 Optimization of bulk heterojunction OSC for**

#### **D-A-A configuration molecule with single cyano group as**

#### **the electron donor material**

### **3.1 Introduction**

In this chapter, four novel p-type electron donor materials, DTCPB, DTCTB, DTCPBO and DTCTBO were investigated and fabricated into OSC. These compounds were synthesized and supported by Prof. Keng-Tsung Wong's group, Department of Chemistry, National Taiwan University. Compared with the previous work<sup>86</sup>, dicyanovinylene (DCV) groups were replaced by single cyano in our study to provide larger  $\Delta E_{\text{LUMO}}$  between electron donor and acceptor materials, which improves exciton dissociation at donor/acceptor interface and reduce recombination.

With systematically engineering the OSC device structures based on these four electron donor materials and  $C_{60}$  and  $C_{70}$  as the electron acceptor materials, we found that the optimized ones were bulk heterojunction due to their superior FF values. In our optimized device structures, power conversion efficiencies of DTCPB, DTCTB, DTCPBO and DTCTBO based OSCs were 6.55%, 4.40%, 5.98%, 4.65%, respectively. Incident illumination power was varied for studying the recombination characteristics of OSCs with different electron donor materials.

### **3.2 Photophysical properties of the four single cyano group electron**

## donor materials

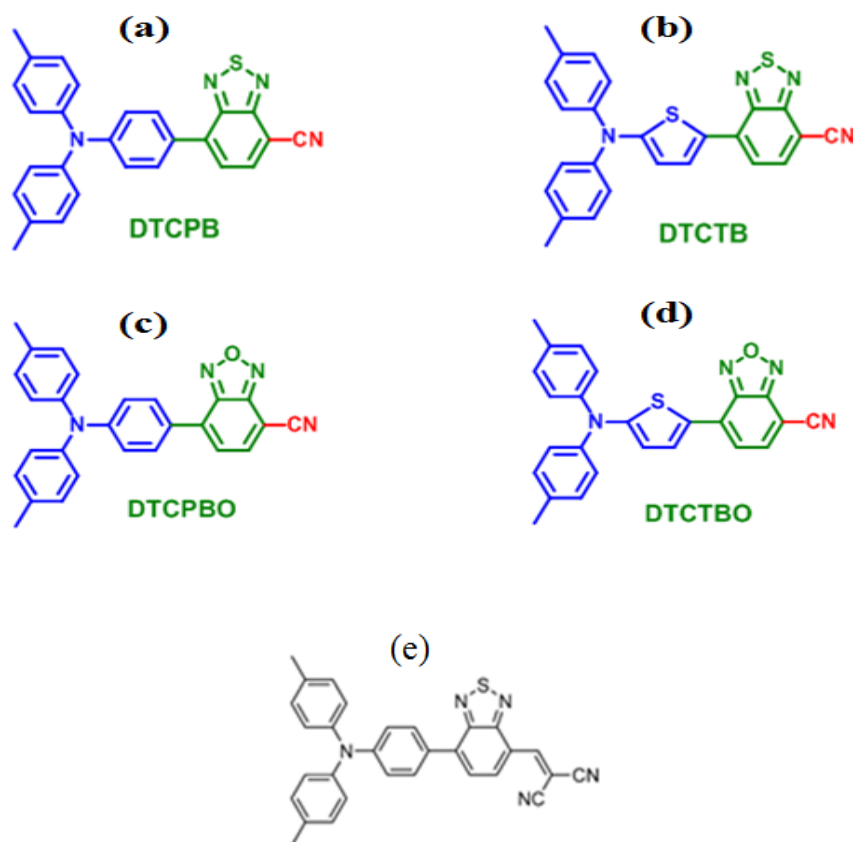


Fig. 3-1 Molecular structures of (a) DTCTB, (b) DTCPB, (c) DTCPBO, (d) DTCTBO and (e) DTDCPB.

Fig. 3-1 shows the molecular structures of DTCPB, DTCTB, DTCPBO and DTCTBO, respectively, which were originally modified from the compound 2-{[7-(4-N, N-ditolylaminophenyl)-1-yl]-2,1,3-benzothiadiazol-4-yl}methylene} malononitrile (DTDCPB), as shown in Fig. 3-1 (e). All these organic materials were synthesized by Prof. Keng-Tsung Wong's group. With connecting a single cyano moiety attached as the electro-withdrawing end-group, LUMO value can be easily raised up (1 eV higher than acceptor) while maintaining a HOMO value which provides a suitable D-A electro-withdrawing ability compared to an over-strong one



in DTDCPB to prevent the formation of dipoles. The entire chemical configuration for four compounds with single cyano groups were shown in Fig. 3-1. However, there is one disadvantage for these four materials that the wide bandgap characteristics (higher LUMO with the same HOMO, compared to DTDCPB) results in blue-shift in absorption spectra combined with the lower absorption ability.

The differences between these four compounds are illustrated below: from the electron donor endcap, the electron-rich and fortified quinoidal characters of thiophene functional groups of DTCTB and DTCTBO result in the redshift (50-70 nm) in absorption spectra, compared to phenylene attached molecules, DTCPB and DTCPBO. Then, considering the central bridging electron-withdrawing unit, benzoxadiazole (BO) and benzothiadiazole (BT), absorption spectra of BO-based molecules (DTCPBO and DTCTBO) are redshifted compared to those of BT-based ones (for DTCPB and DTCTB). and the HOMO levels were also deep-lying. Fig. 3-2 shows the absorption spectra of these four molecules in solution ( $\text{CH}_3\text{Cl}$ ) and thin films (by thermal evaporation).

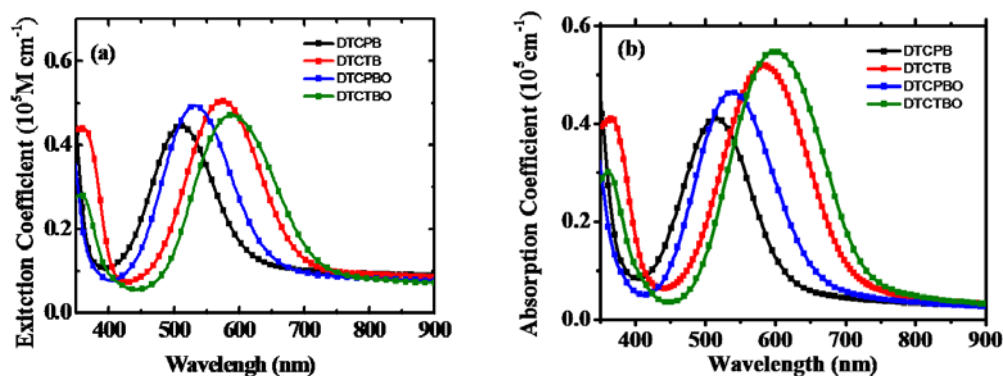


Fig. 3-2 Absorption spectra of the four molecules (a) in solution, and (b) thin films.

The absorption peak for DTCPB, DTCPBO, DTCTB and DTCTBO are 491, 518, 563 and 583 nm for solution and 511, 537, 583, 600 nm for thin film, respectively.

HOMO values of these thin film measured by photoelectron spectrometer are shown in Fig. 3-3. The phenylene-containing groups help to lower the HOMO value respect to thiophene by ~0.1 eV, this shows a similar result in BO and BT moiety. All the parameters and thermal properties for intrinsic parameters were reorganized in the Table. 3-1 and Table. 3-2.

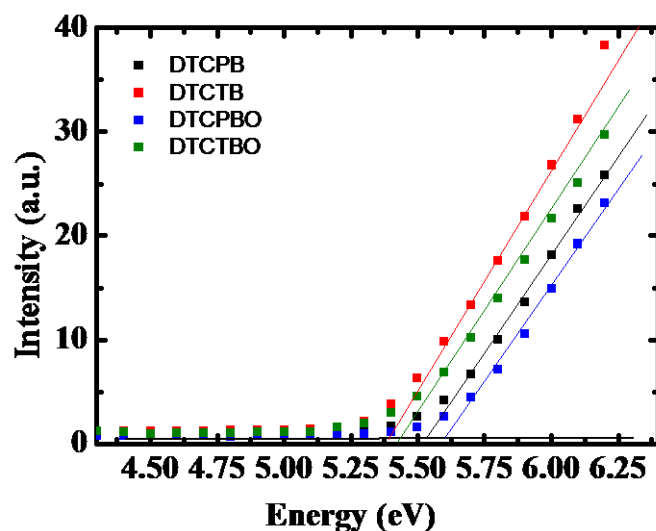


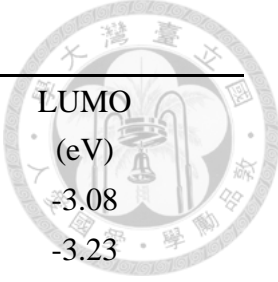
Fig. 3-3 HOMO of DTCPB, DTCPBO, DTCTB and DTCTBO thin films measured by photoelectron spectrometer.

Table. 3-1 Basic characteristics of DTCPB, DTCPBO, DTCTB and DTCTBO in solution.

Dye	$\lambda_{\text{abs}}$ (nm)	$\epsilon$ ( $\text{M}^{-1}\text{cm}^{-1}$ )	HOMO (eV)	LUMO (eV)	$E_g$ (onset) (eV)	$T_g$ (T)	$T_d$ (T)
DTCPB	491	18186	-5.26	-3.22	2.04	-	287
DTCTB	563	23155	-5.16	-3.30	1.86	120	292
DTCPBO	518	23444	-5.30	-3.38	1.92	145	287
DTCTBO	583	33135	-5.24	-3.41	1.83	118	276

Table. 3-2 Basic characteristics of DTCPB, DTCPBO, DTCTB and DTCTBO

for thin film.



Dye	$\lambda_{\text{abs}}$ (nm)	HOMO (eV)	LUMO (eV)
DTCPB	511	-5.51	-3.08
DTCTB	583	-5.40	-3.23
DTCPBO	537	-5.60	-3.27
DTCTBO	600	-5.41	-3.29

### 3.3 OSC optimization of four electron donor materials with single

#### cyano substituent molecules

In this section, we illustrate the optimization procedures of OSCs by using these four electron donor materials with  $C_{60}$  and  $C_{70}$  electron acceptors. We optimized DTCTB first, followed by DTCPB, DTCPBO, and finally DTCTBO in sequence. In our previous research, we found that the optimized OSC structure consisted of an active layer and an electron transport layer (planar-mixed heterojunction structure, PMHJ)<sup>85</sup>. Besides, donor buffer layer between anode and active layer can effectively prevent exciton quenching and increase  $J_{\text{SC}}$  and PCE in OSCs. Hence, we started our device architecture from PMHJ. However, interestingly, in OSCs based on these four electron donor materials, device performances were even better when using simple bulk-heterojunction (BHJ) structure. Besides, insertion of donor buffer layer showed worse efficiency in these OSCs. Hence, the device structure was very simple with two variables, mixing ratio and active layer thicknesses.

In our devices, we used MoOx and bathocuproine (BCP) as the hole extraction layer and exciton blocking layer, respectively. The workfunctions of electrodes and energy levels of materials were shown in Fig. 3-4.

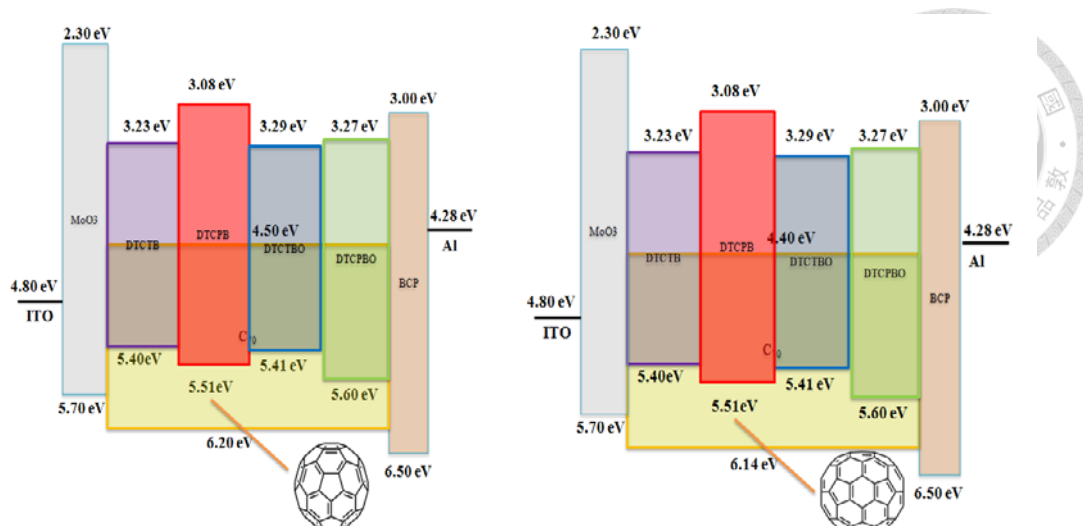


Fig. 3-4 Energy diagrams of four single cyano groups moieties molecules with  $C_{60}$  and  $C_{70}$  under simple bulk heterojunction

### 3.3.1 Comparison between PMHJ and BHJ of DTCTB devices

#### 3.3.1.1 $C_{60}$ based OSC

First of all, we fixed our thickness of active region to 60 nm by changing the ratio thickness between mixing layer and acceptor  $C_{60}$ . In such a design, the optical field distribution did not change a lot. The mixing ratio was fixed at 1:1.6<sup>[85]</sup>.

Table. 3-3 Device configurations from A-1 to A-4 of DTCPB: $C_{60}$  OSC. The unit is nm.

Device	MoO <sub>3</sub>	DTCTB: $C_{60}$	$C_{60}$	BCP	Al
A-1		1:1.6 (Mixing ratio), <b>20</b>	<b>40</b>		
A-2		1:1.6 (Mixing ratio), <b>30</b>	<b>30</b>		
A-3	20	1:1.6 (Mixing ratio), <b>40</b>	<b>20</b>	7	100
A-4		1:1.6 (Mixing ratio), <b>50</b>	<b>10</b>		

J-V characteristic of devices from A-1 to A-5 under dark condition and 1-sun AM 1.5 G solar illumination was shown in Fig. 3-5 and the device performance was shown in Table. 3-4. As the thickness of mixing layer increased,  $J_{SC}$  increased,  $R_S$  decreased, and PCE increased, which meant  $C_{60}$  layer should be as thin as possible.

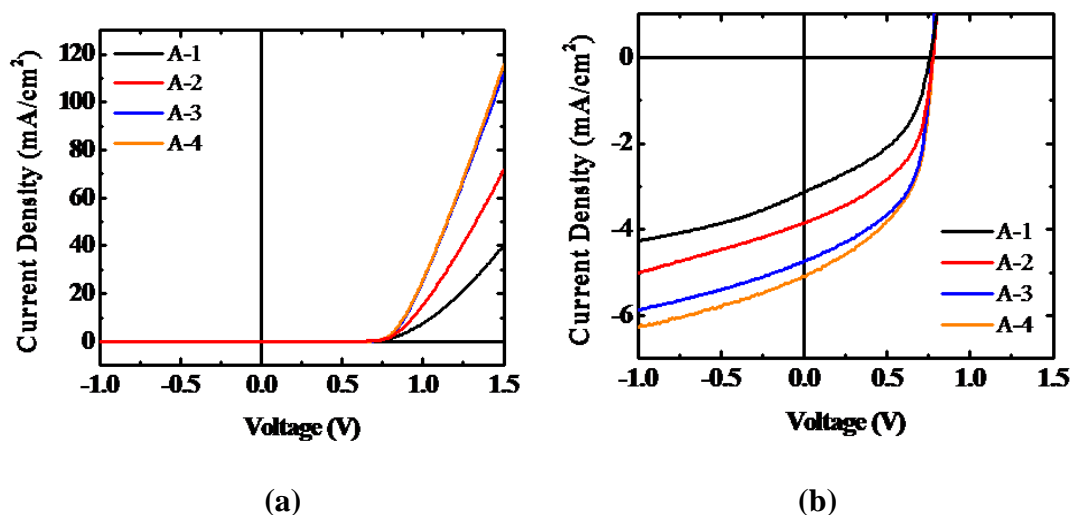


Fig. 3-5 J-V performances of devices from A-1 to A-4 under (a) dark condition and (b) 1-sun solar illuminations.

Table. 3-4 Performances of devices from A1 to A-4 under 1-sun solar illumination.

Name	$V_{OC}$ (V)	$J_{SC}$ (mA/cm <sup>2</sup> )	FF (%)	Eff (%)	$R_{sh}$ (k $\Omega$ *cm <sup>2</sup> )	$R_s$ ( $\Omega$ *cm <sup>2</sup> )
A-1	0.76	3.14	44.51	1.06	0.57	50.16
A-2	0.78	3.86	49.44	1.49	0.69	35.38
A-3	0.77	4.74	53.52	1.95	0.64	22.67
A-4	0.78	5.26	48.64	1.99	0.51	23.41

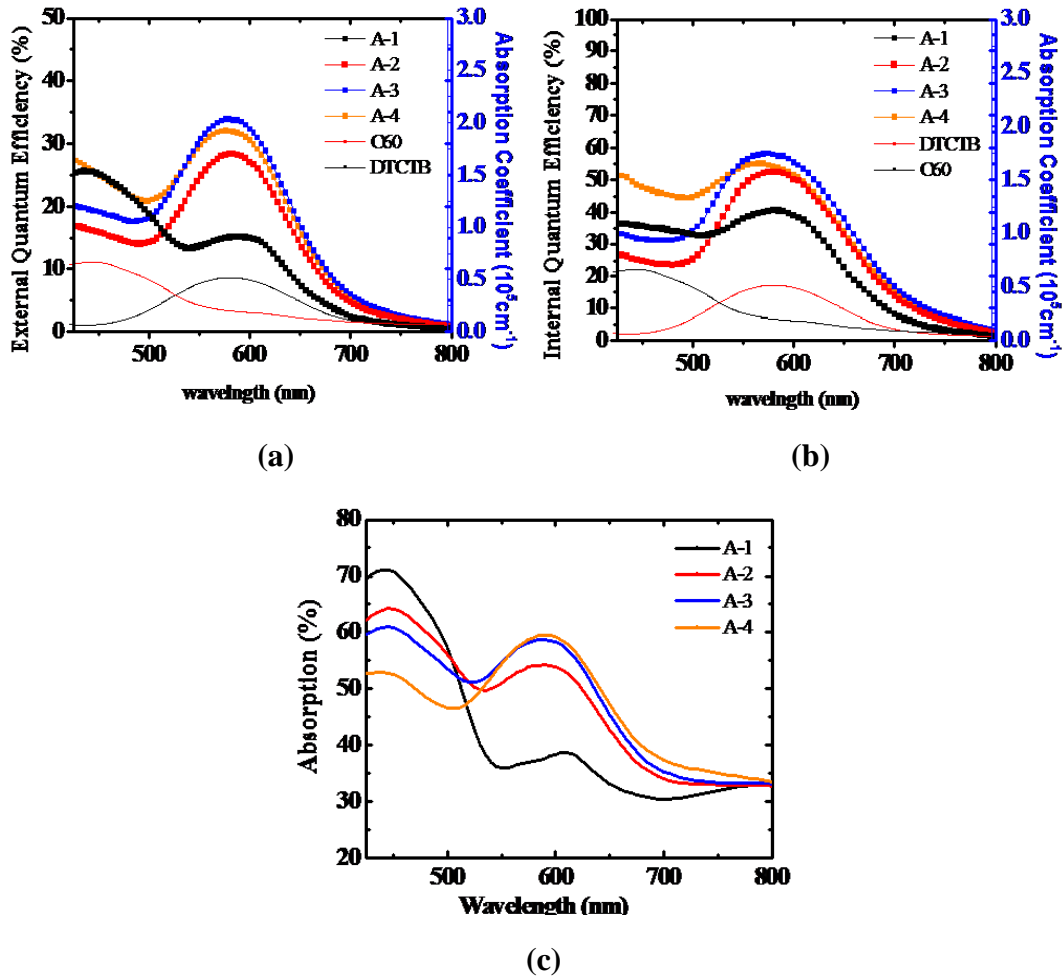


Fig. 3-6 (a) EQE, (b) IQE and (c) absorption spectrum of devices from A-1 to A-4.

### 3.3.1.2 C<sub>70</sub> based OSC

Here, we attempt to apply another acceptor, C<sub>70</sub> to enhance our PCE. In our previous work<sup>85</sup>, although C<sub>70</sub> can induce a higher J<sub>SC</sub>, the electrical property was poor compared to C<sub>60</sub> so we can introduce a transporting by higher mobility C<sub>60</sub> while mixture with C<sub>70</sub>. In this section, we varied the transporting layer as C<sub>60</sub> or C<sub>70</sub>, or give a replacement with a mixing layer for preventing from the variation of optical field distribution, in other words, to compare the PMHJ and BHJ in C<sub>70</sub> system.

Devices configurations and performances were shown in Table. 3-5 and Table. 3-6. The J-V performances for devices of A-5 to A-7 under dark condition and illuminations were shown in Fig. 3-7

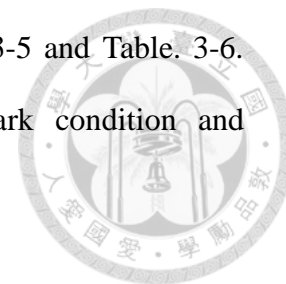


Table. 3-5 Device configurations from A-5 to A-7 of DTCPB:C<sub>70</sub> OSC. The unit is nm.

Device	MoO <sub>3</sub>	DTCTB:C <sub>60</sub>	C <sub>60</sub>	BCP	Al
A-5		1:2.2 (C <sub>70</sub> ) , 60	10 (C <sub>60</sub> )		
A-6	20	1:2.2 (C <sub>70</sub> ) , 60	10(C <sub>70</sub> )	7	100
A-7		1:2.2 (C <sub>70</sub> ) , 70	0		

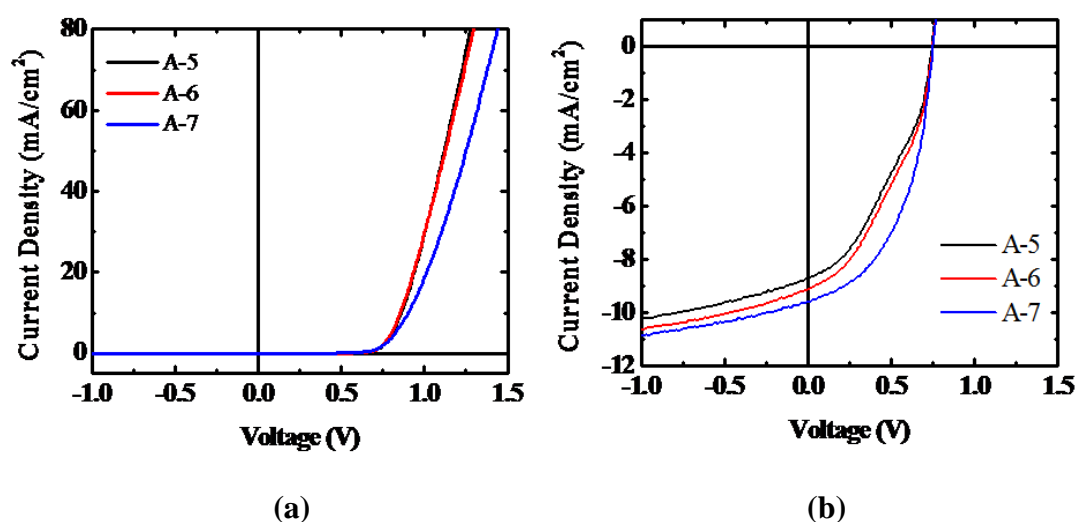


Fig. 3-7 J-V performances of devices from A-5 to A-7 under (a) dark condition and (b) 1-sun solar illuminations.

Table. 3-6 Performances of devices from A-5 to A-7 under 1-sun solar illumination.

Name	V <sub>oc</sub> (V)	J <sub>sc</sub> ( mA/cm <sup>2</sup> )	FF (%)	Eff (%)	R <sub>sh</sub> (kΩ*cm <sup>2</sup> )	R <sub>s</sub> (Ω*cm <sup>2</sup> )
A-5	0.75	8.67	36.28	2.37	0.36	17.01
A-6	0.74	9.16	38.65	2.62	0.36	15.55

A-7	0.75	9.63	47.02	3.41	0.44	15.90
-----	------	------	-------	------	------	-------

Among these three devices, one can see that BHJ device (A-7) exhibited highest RSH, FF, and PCE, which meant the introduction of acceptor layer (C60 or C70) resulted in carrier accumulation and carrier recombination.

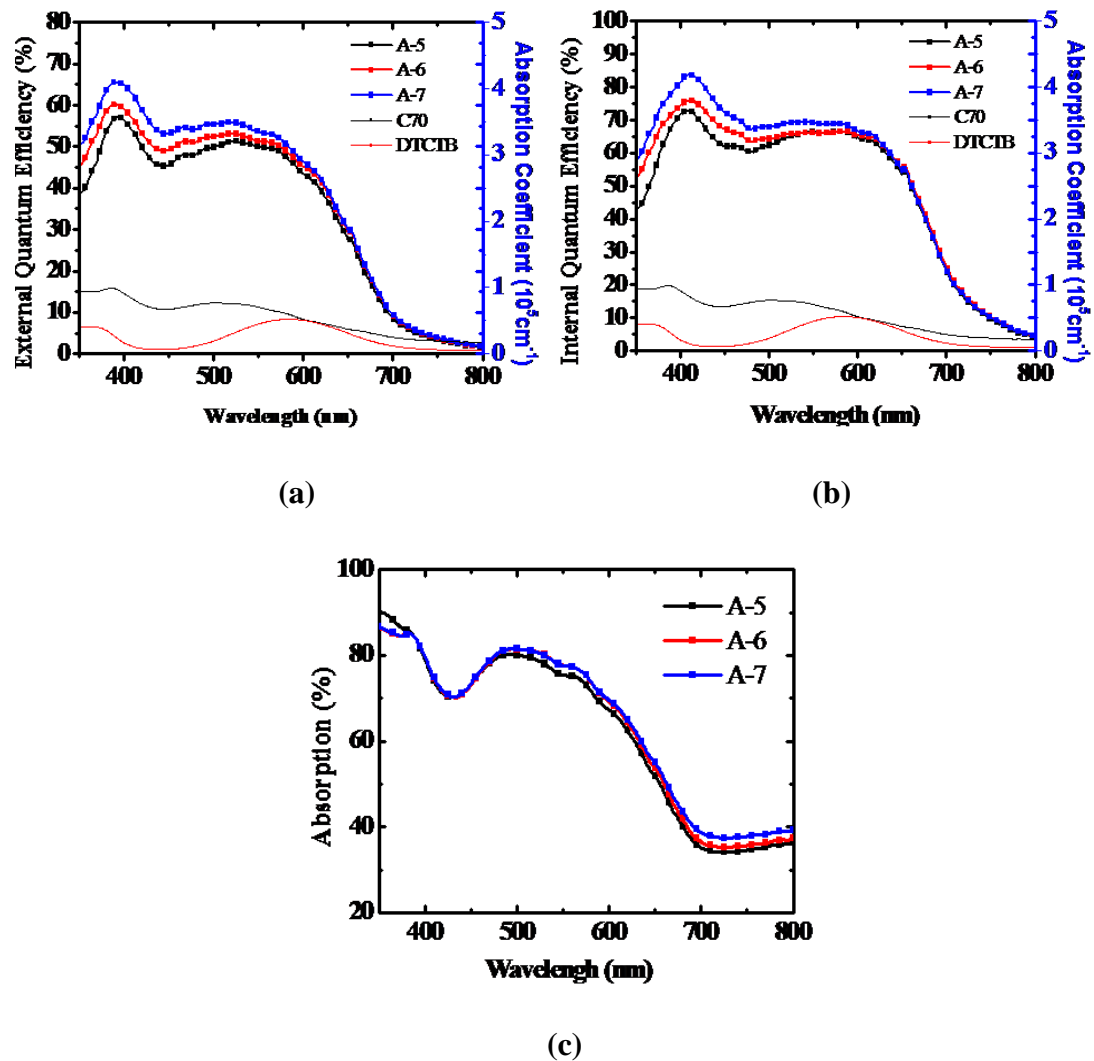


Fig. 3-8 (a) EQE, (b) IQE and (c) absorption spectrum of devices from A-5 to A-7.

### 3.3.2 Optimization of different mixing ratio and thickness of active layer for DTCTB



### 3.3.2.1 C<sub>60</sub> based OSC

Then, we tuned the mixing ratio of electron donor and acceptor material, as shown in Table 3-7. J-V characteristic of devices to under dark condition and 1-sun AM 1.5 G solar illumination was shown in Fig. 3-9 and performances were shown in Table. 3-8. One can see that the optimized mixing ratio is DTCTB:C<sub>60</sub> = 1:2.2 (A-10). Comparing devices A-10 and A-13, C<sub>60</sub> neat acceptor layer should be replaced by mixing layer for improving PCE.

Table. 3-7 Devices configuration of devices from A-4, A-8 to A-13. The unit is nm.

Device	MoO <sub>3</sub>	DTCTB:C <sub>60</sub>	C <sub>60</sub>	BCP	Al
A-4		1:1.6 (Mixing ratio), <b>50</b>	10		
A-8		<b>1:1.6</b> (Mixing ratio) , 60	10		
A-9		<b>1:1.9</b> (Mixing ratio) , 60	10		
A-10		<b>1:2.2</b> (Mixing ratio) , 60	10	7	100
A-11		<b>1:2.4</b> (Mixing ratio) , 60	10		
A-12		<b>1:2.5</b> (Mixing ratio) , 60	10		
A-13		1:2.2 (Mixing ratio) , <b>70</b>	<b>0</b>		

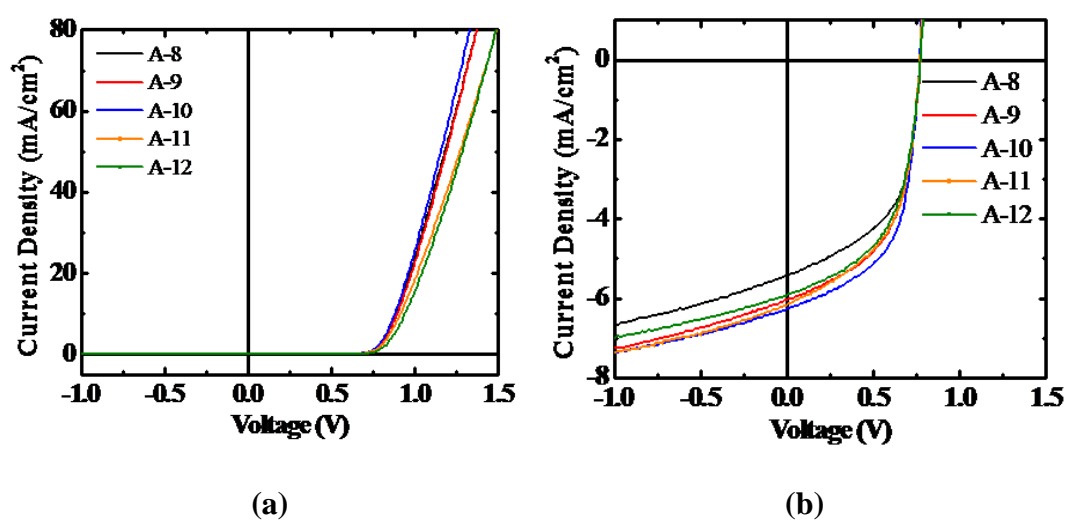


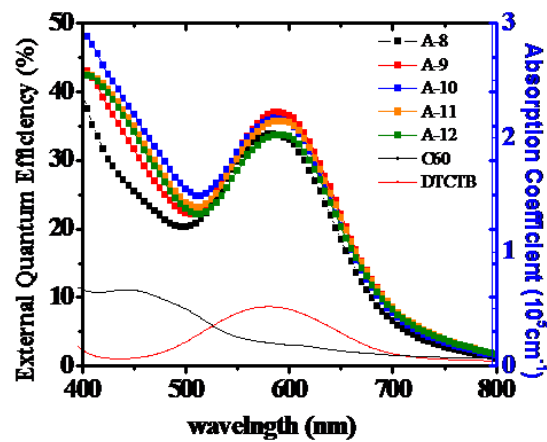
Fig. 3-9 J-V performances from of device A-4 to A-12 under (a) dark condition

and (b) 1-sun solar illuminations.



Table. 3-8 Performances of devices from A-4, A-8 to A-13 under 1-sun solar illumination.

Name	V <sub>OC</sub> (V)	J <sub>SC</sub> (mA/cm <sup>2</sup> )	FF (%)	Eff (%)	Rsh (kΩ*cm <sup>2</sup> )	Rs (Ω*cm <sup>2</sup> )
A-4	0.78	5.26	48.64	1.99	0.51	23.41
A-8	0.78	5.30	53.64	2.22	0.58	23.48
A-9	0.77	6.14	54.83	2.59	0.60	19.33
A-10	0.77	6.26	57.27	2.76	0.63	17.06
A-11	0.77	6.15	53.00	2.51	0.52	19.64
A-12	0.78	5.91	52.79	2.43	0.66	22.74
A-13	0.77	6.14	57.58	2.72	0.74	16.91



(a)

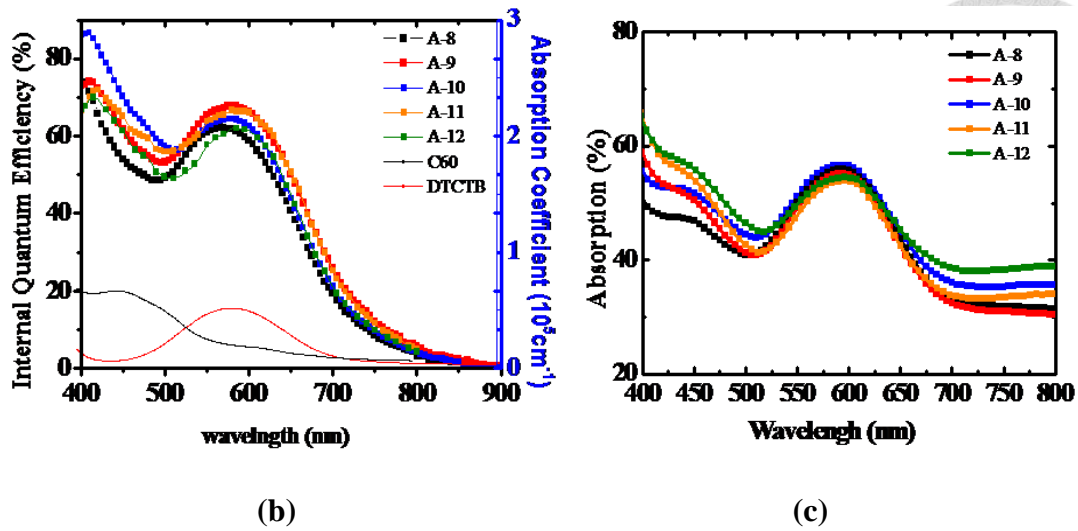


Fig. 3-10 (a) EQE, (b) IQE and (c) absorption spectrum of devices A-8 and A-13.

### 3.3.2.2 C<sub>70</sub> based OSC

In this section, we optimize the DTCTB: C<sub>70</sub> by varying the mixing ratio and thickness. The optimized condition is DTCTB: C<sub>70</sub> = 1: 2.6 with the thickness of 70 nm, as shown in Fig. 3-10 and 3-11 and Tables 3-9 and 3-10.

Table. 3-9 Device configurations for different ratio and thickness of active layer of A-7, A-14 to A-17 of DTCTB:C<sub>70</sub> based OSC. The unit is nm.

Device	MoO <sub>3</sub>	DTCTB:C <sub>70</sub>	C <sub>70</sub>	BCP	Al
A-7		<b>1:2.2</b> (Mixing ratio) , 70			
A-14		<b>1:2.6</b> (Mixing ratio) , 70			
A-15	20	<b>1:3.0</b> (Mixing ratio) , 70	0	7	100
A-16		1:2.6 (Mixing ratio), <b>60</b>			
A-17		1:2.6 (Mixing ratio), <b>80</b>			

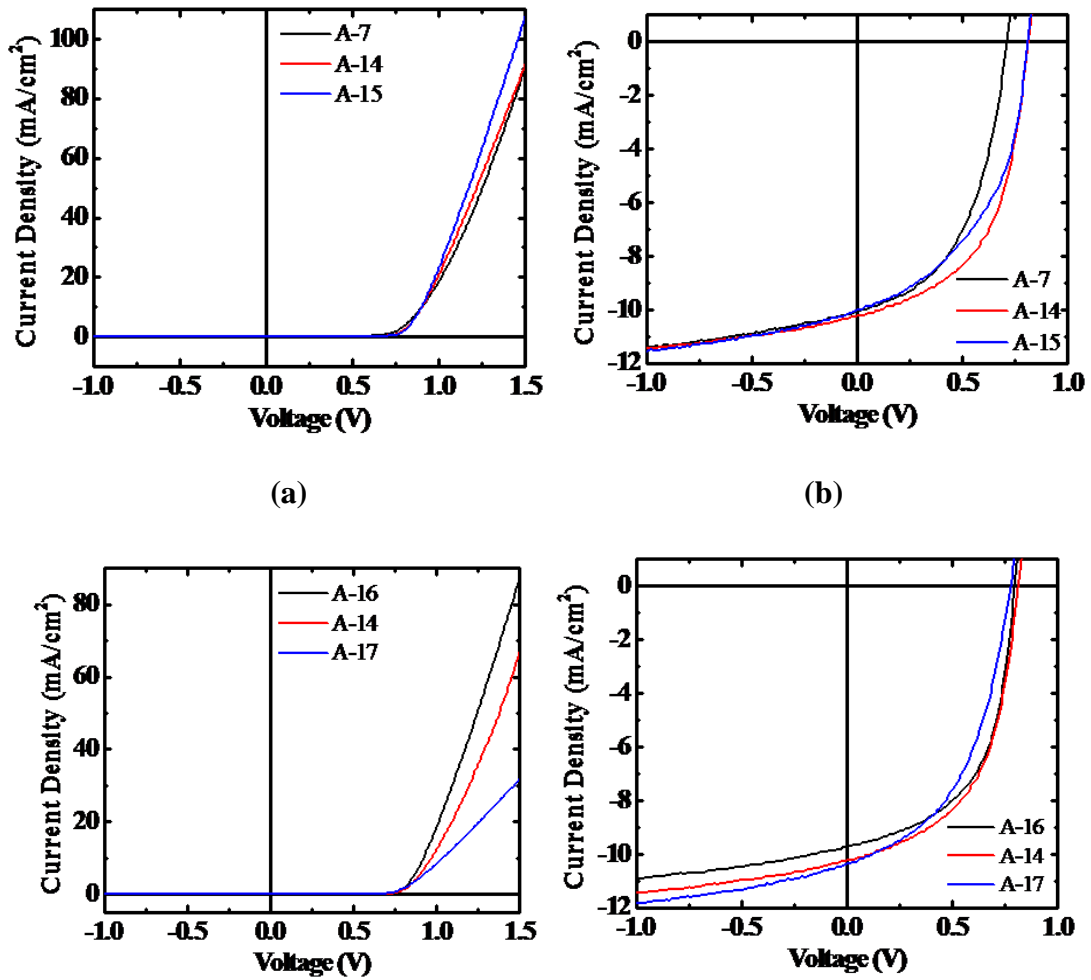
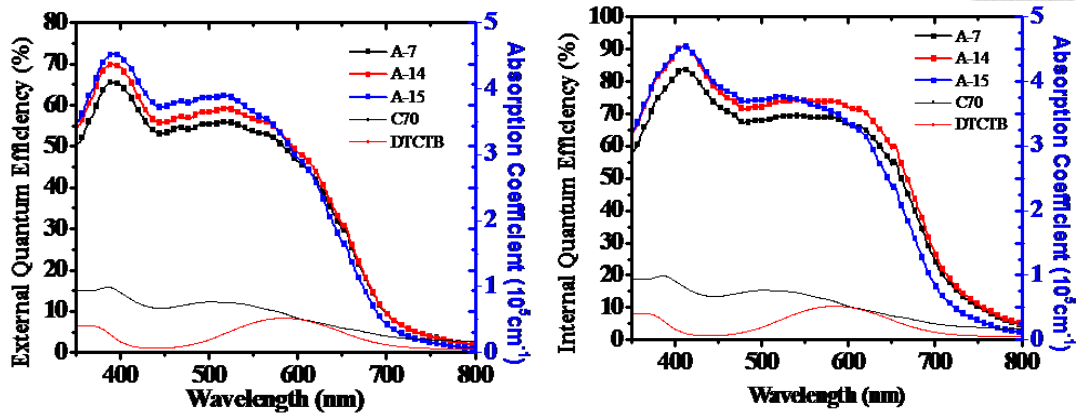


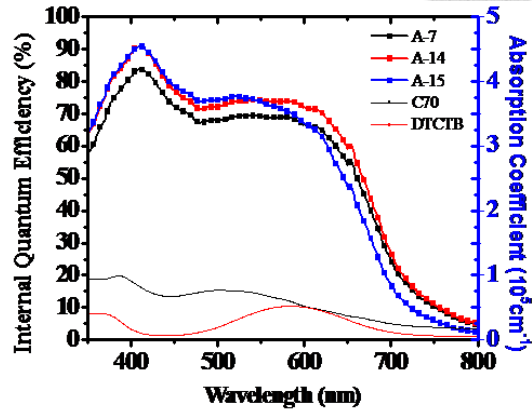
Fig. 3-11 J-V performance of devices from 3-20 to 3-22 under (a) dark condition and (b) 1-sun solar illuminations.

Table. 3-10 Devices performance of different mixing ratio and thickness of active layer for DTCPB/  $C_{70}$  based OSC.

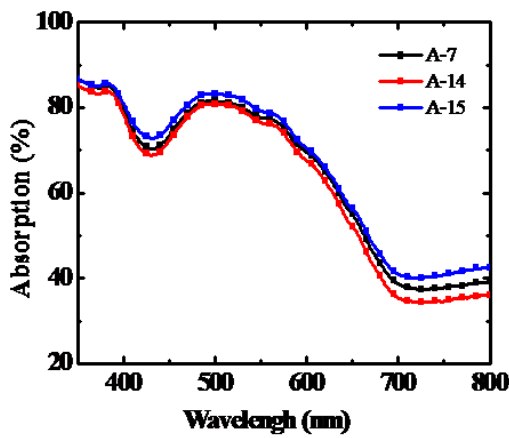
Name	$V_{OC}$ (V)	$J_{SC}$ ( $\text{mA}/\text{cm}^2$ )	FF (%)	Eff (%)	$R_{sh}$ ( $\text{k}\Omega \cdot \text{cm}^2$ )	$R_s$ ( $\Omega \cdot \text{cm}^2$ )
A-7	0.75	9.63	47.02	3.41	0.44	15.90
A-14	0.81	10.11	53.37	4.40	0.50	9.41
A-15	0.81	10.04	46.88	3.83	0.37	9.38
A-16	0.79	9.71	54.70	4.23	0.53	8.29
A-17	0.79	10.03	47.78	3.81	0.37	10.98



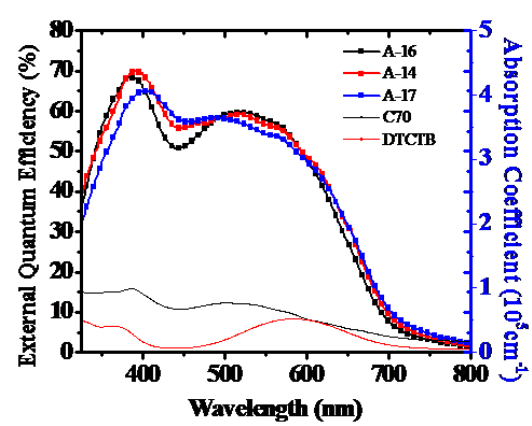
(a)



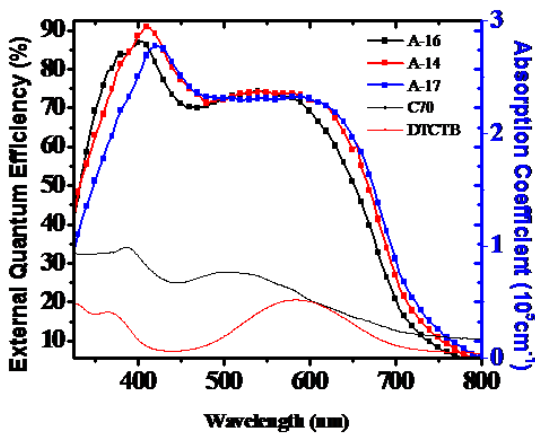
(b)



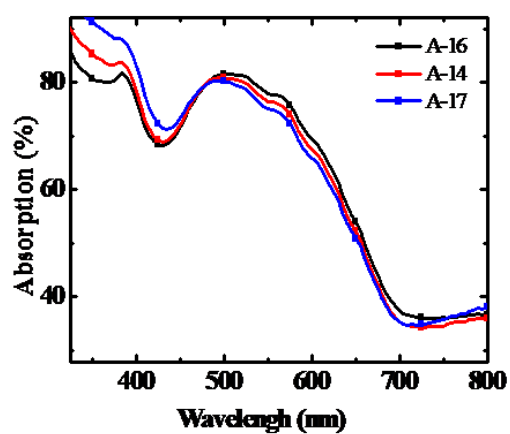
(c)



(d)



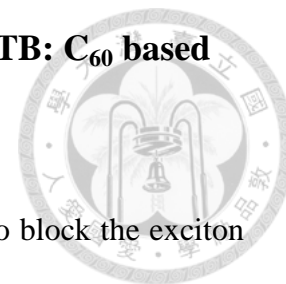
(e)



(f)

Fig. 3-12 (a) EQE, (b) IQE and (c) absorption spectrum of devices A-7, A-14 to A-15 with different mixing ratio and (d) EQE, (e) IQE and (f) absorption spectrum of devices from A-14, A-16 to A-17 with different thickness of active layer.

### 3.3.2.3 Replacement of different blocking layer for DTCTB: C<sub>60</sub> based OSC



Here, we employed several kinds of blocking layer in order to block the exciton from anode side and promote the hole transport ability. These blocking layer showed different HOMO values in Fig. 3-13. The devices configurations and detail performances were also present in Table. 3-11 and Table. 3-12, respectively. The J-V performances for devices from A-18 to A-25 under dark condition and illuminations were shown in Fig. 3-14. However, the insertion of blocking layer resulted in higher R<sub>s</sub>, and little enhancement (if any) on J<sub>SC</sub>, which resulted in worse PCE.

Table. 3-11 Device configurations for different blocking layers applied on champion device for DTCTB:C<sub>60</sub> based OSC. The unit is nm.

Device	MoO <sub>3</sub>	Blocking layer	DTCTB:C <sub>60</sub>	C <sub>60</sub>	BCP	Al
A-10		<b>None</b>				
A-18		<b>mCP 1</b>				
A-19		<b>mCP 3</b>				
A-20		<b>mCP 5</b>				
A-21	20	<b>NPB 1</b>	1:2.2 (Mixing ratio) , 60	10	7	100
A-22		<b>NPB 3</b>				
A-23		<b>NPB 5</b>				
A-24		<b>DTCTB 3</b>				
A-25		<b>DTCTB 5</b>				

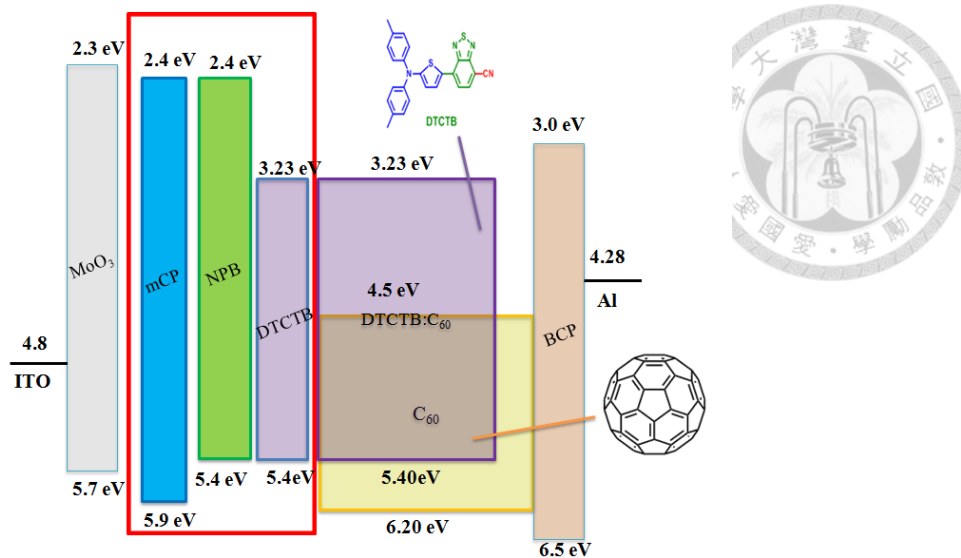
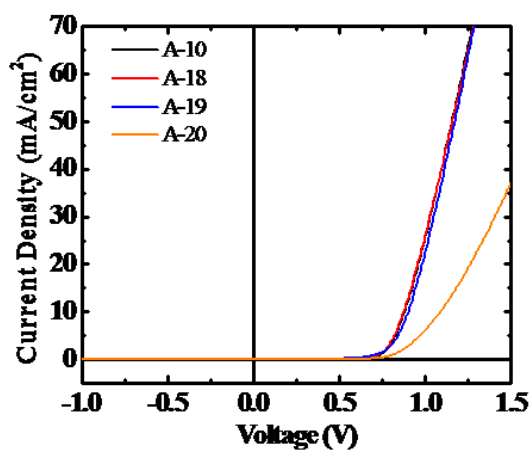
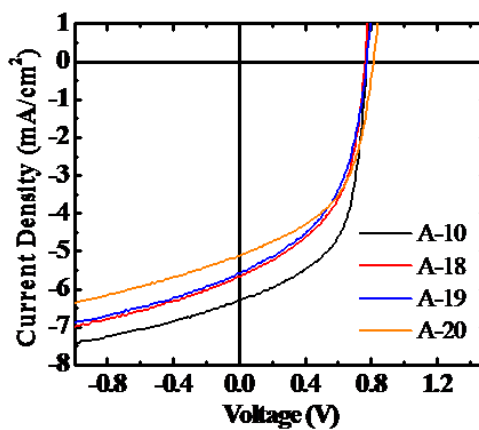


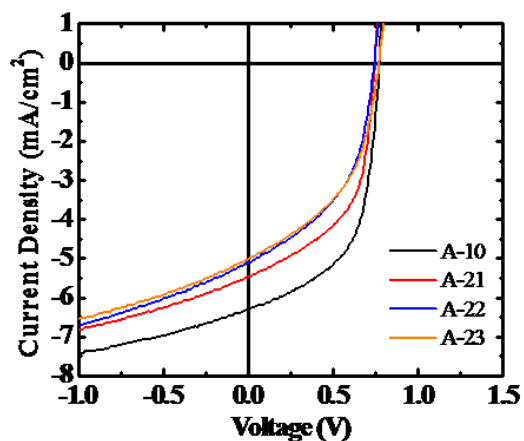
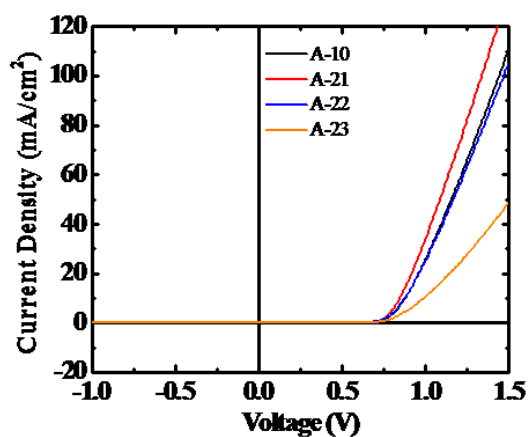
Fig. 3-13 Configurations of devices and energy diagrams for different blocking layer of DTCTB:C<sub>60</sub> based OSC.



(a)



(b)



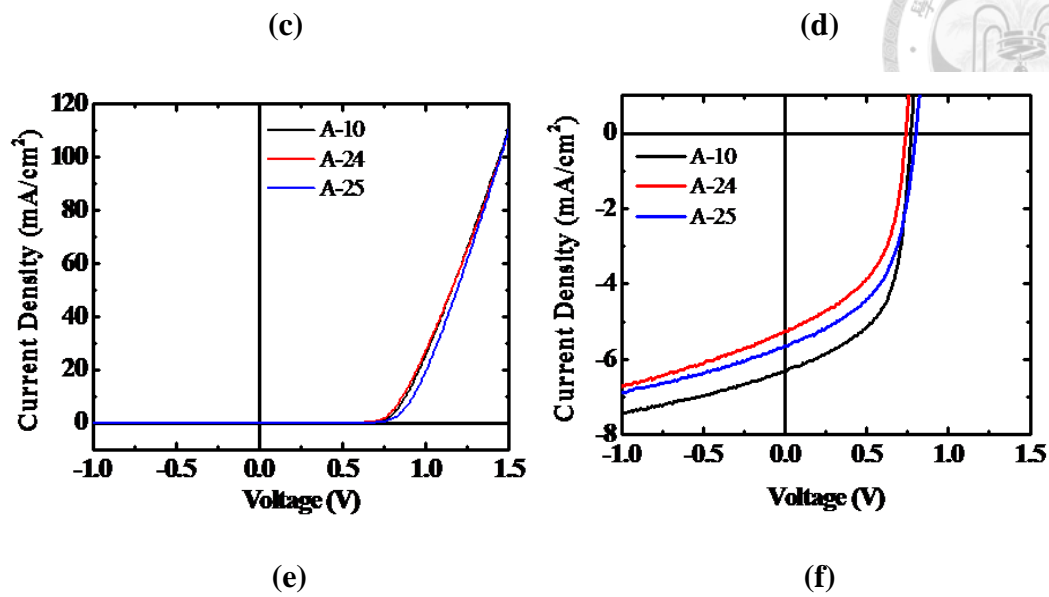
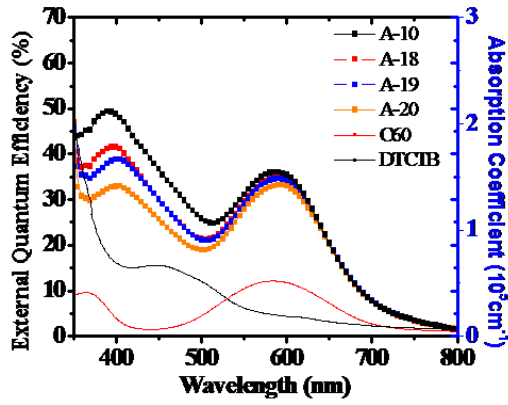
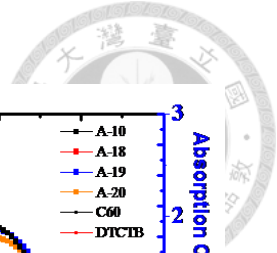


Fig. 3-14 J-V performances from A-18 to A-25 under (a) mCP inserted dark condition and (b) 1-sun solar illuminations, (c) NPB inserted under dark condition and (d) 1-sun solar illuminations and (e) DTDTB inserted under dark condition and (f) 1-sun solar illuminations.

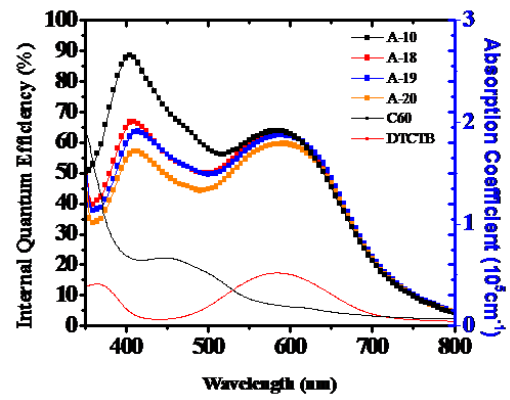
Table. 3-12 Devices performances of for different blocking layer of DTCTB:C60 based OSC.

Name	$V_{oc}$ (V)	$J_{sc}$ (mA/cm <sup>2</sup> )	FF (%)	Eff (%)	$R_{sh}$ (k $\Omega$ *cm <sup>2</sup> )	$R_s$ ( $\Omega$ *cm <sup>2</sup> )
A-10	0.77	6.26	57.27	2.76	0.63	17.06
A-18	0.76	5.64	49.15	2.12	0.50	24.22
A-19	0.79	5.59	47.51	2.12	0.49	36.76
A-20	0.81	5.17	49.59	2.10	0.59	48.17
A-21	0.76	5.64	49.15	2.121	0.50	24.22
A-22	0.79	5.59	47.51	2.122	0.49	36.76
A-23	0.81	5.17	49.59	2.100	0.59	48.17
A-24	0.76	5.22	50.06	1.99	0.51	20.92
A-25	0.80	5.73	50.24	2.32	0.54	38.95

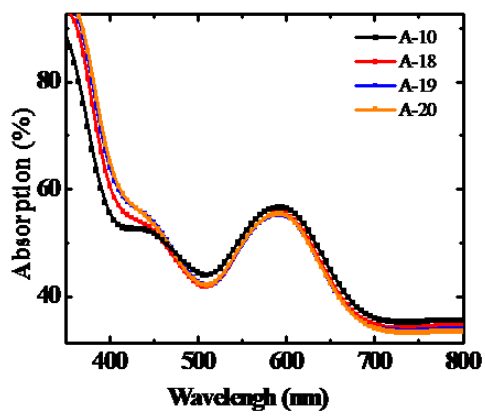




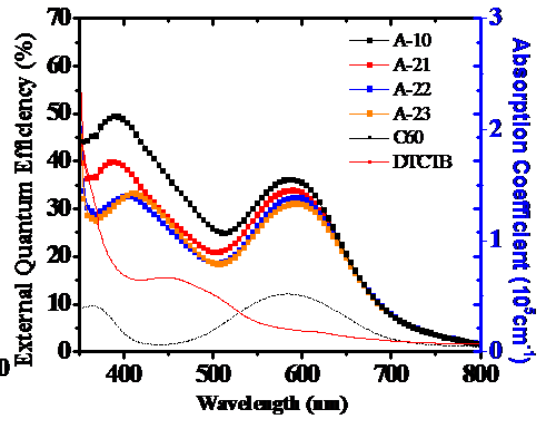
(a)



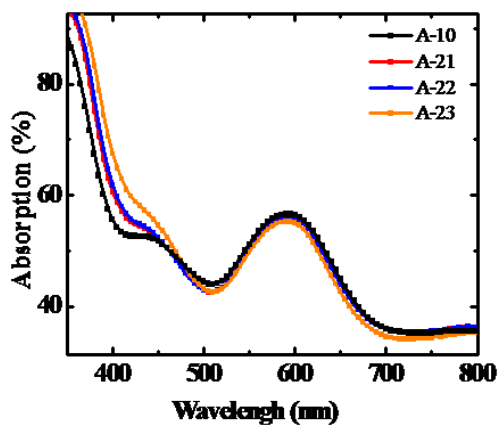
(b)



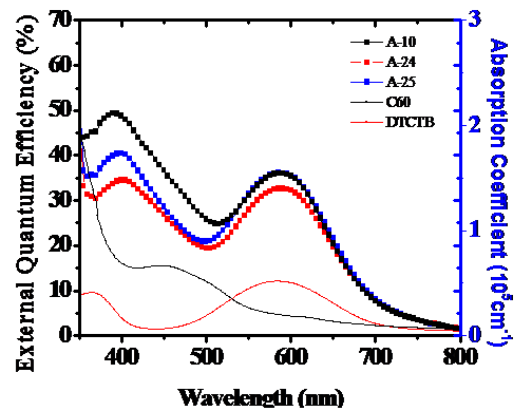
(c)



(d)



(e)



(f)

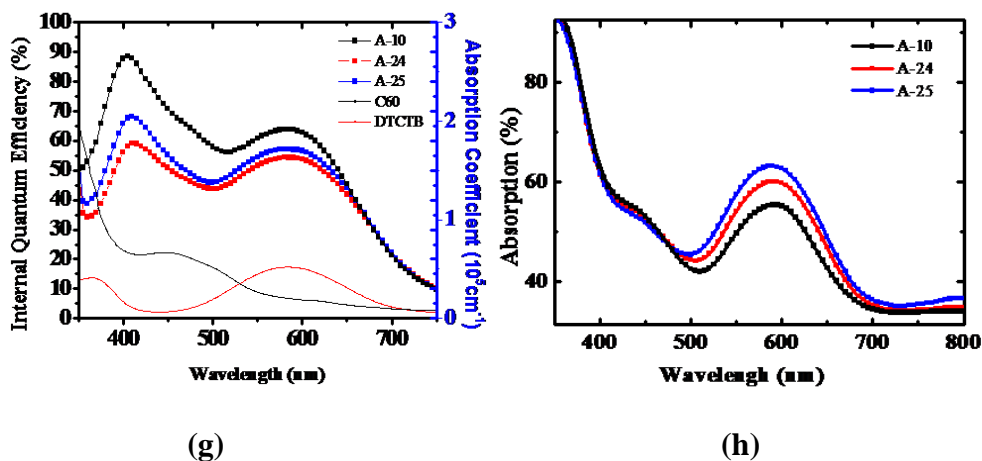


Fig. 3-15(a) EQE, (b) IQE and (c) absorption spectrum mCP inserted OSC and (d) EQE, (e) IQE and (f) absorption spectrum NPB inserted OSC and (g) EQE, (h) IQE and (i) absorption spectrum mCP inserted OSC and

### 3.3.3 Comparison between PMHJ and BHJ of DTCPB: C<sub>60</sub> based OSC

Table. 3-13 Device configurations for different relative ratio between mixing transporting layer from B-1 to B-7 of DTCPB based OSC. The unit is nm.

Device	MoO <sub>3</sub>	DTCPB:C <sub>60</sub>	C <sub>60</sub>	BCP	Al
B-1		1:1.6 (Mixing ratio), <b>30</b>	<b>30</b>		
B-2		1:1.6 (Mixing ratio), <b>40</b>	<b>20</b>		
B-3	20	1:1.6 (Mixing ratio), <b>45</b>	<b>15</b>	7	100
B-4		1:1.6 (Mixing ratio), <b>50</b>	<b>10</b>		
B-5		1:1.6 (Mixing ratio), <b>60</b>	<b>10</b>		
B-6	20	1:1.6 (Mixing ratio), <b>65</b>	<b>5</b>	7	100
B-7		1:1.6 (Mixing ratio), <b>70</b>	<b>0</b>		

In this section, we introduced the second compound under single cyano groups modification. Thiophene were replaced by phenylene can gives a lower lying HOMO but remained a similar LUMO value, which resulted in a weaker absorption ability. At

first, we varied the ratio between mixing layer and transporting layer with a fixed thickness 60 nm with mixing ratio of 1:1.6. Table. 3-12 shows the devices configurations for tuning the devices ratio and the devices performances were also present in Table. 3-13. The J-V performances for devices from B-1 to B-7 under dark condition and illuminations were shown in Fig. 3-16. One can see that OSC with BHJ structure (B-7) exhibited highest efficiency.

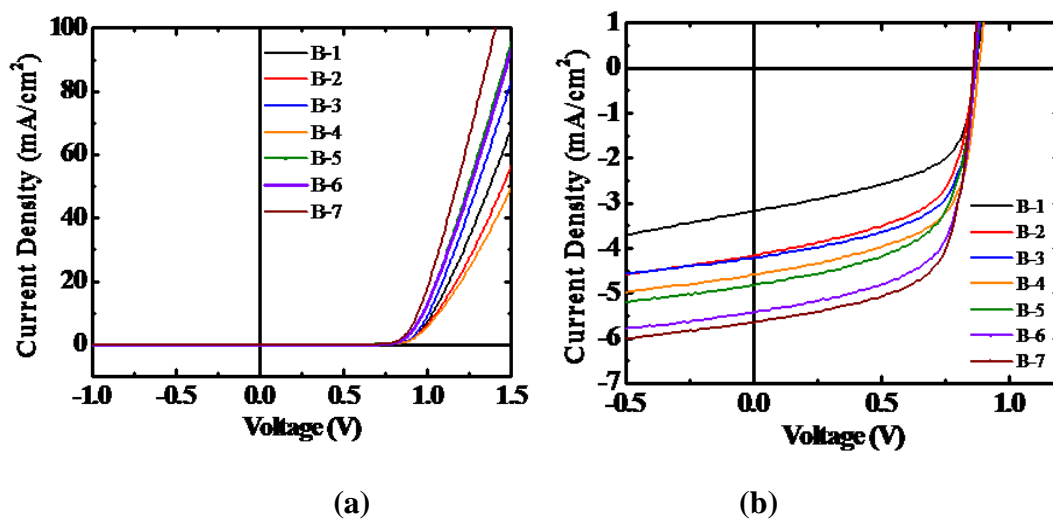
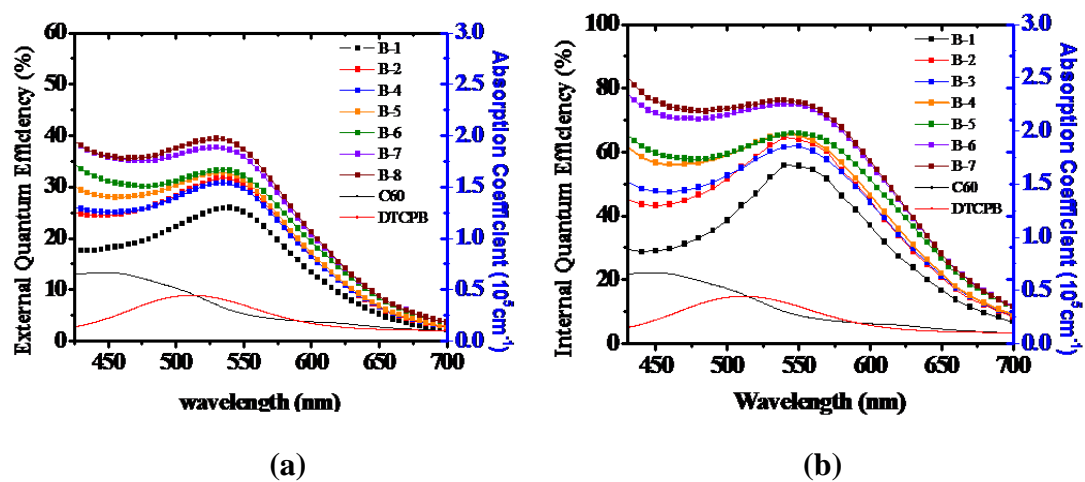


Fig. 3-16 J-V performances of devices under (a) dark condition and (b) 1-sun solar illuminations from B-1 to B-7.



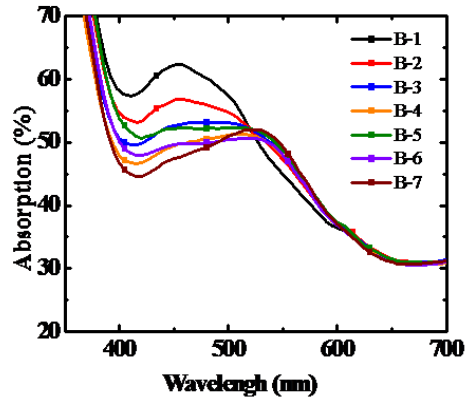


Fig. 3-17 (a) EQE, (b) IQE and (c) absorption spectrum of devices from B-1 to B-7.

Table. 3-14 Performances of device from B-1 to B-7 with various thickness of mixing layer under 1-sun solar illumination.

Name	V <sub>oc</sub> (V)	J <sub>sc</sub> ( mA/cm <sup>2</sup> )	FF (%)	Eff (%)	R <sub>sh</sub> (kΩ*cm <sup>2</sup> )	R <sub>s</sub> (Ω*cm <sup>2</sup> )
B-1	0.86	3.16	53.43	1.46	0.94	33.68
B-2	0.85	4.13	55.80	1.98	0.97	22.21
B-3	0.86	4.19	60.13	2.18	1.22	21.46
B-4	0.86	4.69	60.57	2.44	1.07	16.93
B-5	0.86	4.82	58.89	2.46	1.09	21.31
B-6	0.87	5.44	62.14	2.94	1.12	17.05
B-7	0.86	5.57	64.04	3.08	1.20	15.64

### 3.3.4 Optimization of mixing ratio and thickness of active layer for DTCPB

#### 3.3.4.1 C<sub>60</sub> based OSC

In this section, we varied the mixing ratio and the thickness of the active

layer. The optimized values are DTCPB:C<sub>60</sub>= 1: 2.2 with thickness of 90 nm in B-14, as shown below.

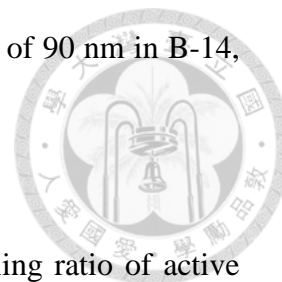
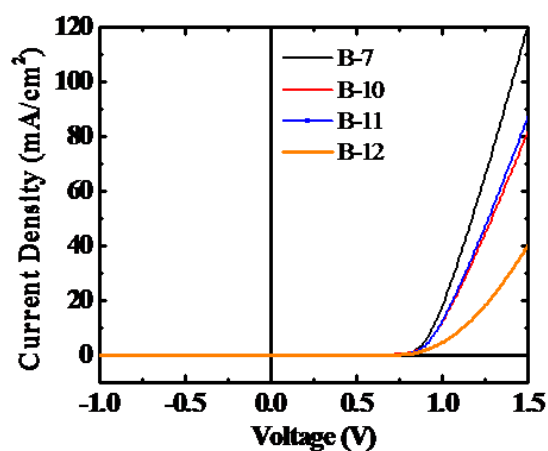
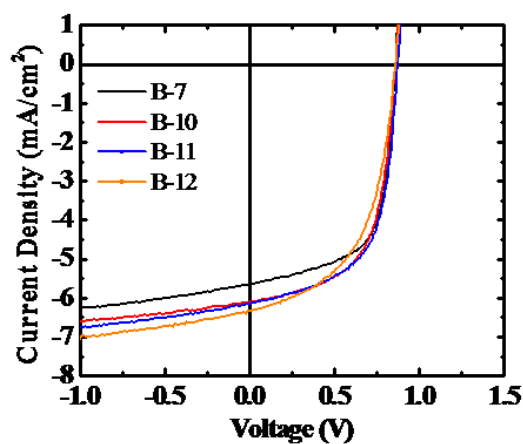


Table. 3-15 Device configurations for different thickness and mixing ratio of active layer for devices B-10 to B-15 of DTCPB: C<sub>60</sub> based OSC. The unit is nm.

Device	MoO <sub>3</sub>	DTCPB:C <sub>60</sub>	C <sub>60</sub>	BCP	Al
B-7		1:1.6 (Mixing ratio), <b>70</b>	<b>0</b>		
B-10		1:1.6 (Mixing ratio), <b>80</b>	<b>0</b>		
B-11		1:1.6 (Mixing ratio), <b>90</b>	<b>0</b>		
B-12	20	1:1.6 (Mixing ratio), <b>100</b>	<b>0</b>	7	100
B-13		<b>1:1.4</b> (Mixing ratio), 90	0		
B-14		<b>1:2.2</b> (Mixing ratio), 90	0		
B-15		<b>1:2.6</b> (Mixing ratio), 90	0		



(a)



(b)

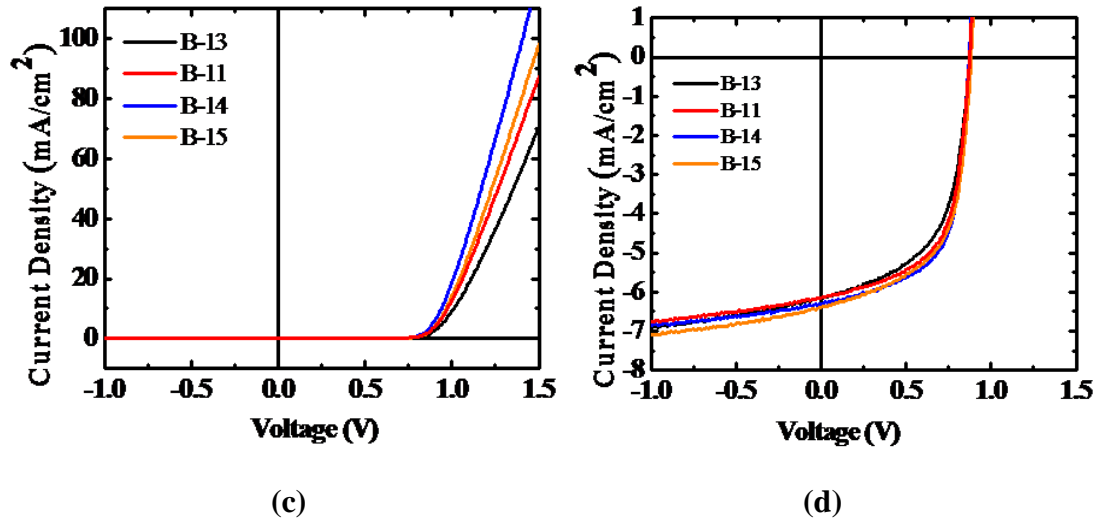
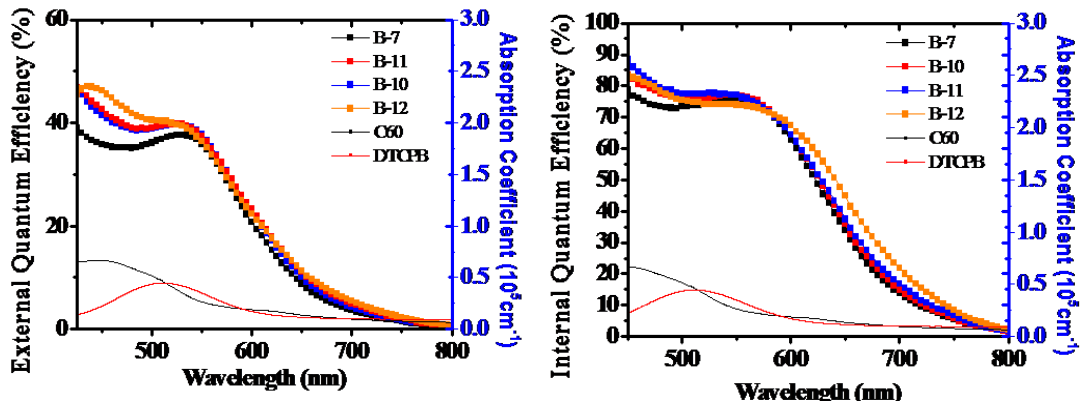


Fig. 3-18 J-V performances of devices for B-7, B-10 to B-15 with different thickness under (a) and (c) dark condition and (b) and (d) 1-sun solar illuminations.

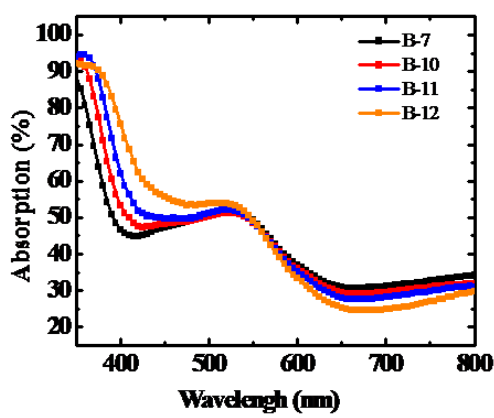
Table. 3-16 Performance of device from B-7 to B-15 with various ratio between mixing and transporting layers under 1-sun solar illumination

Name	$V_{OC}$ (V)	$J_{SC}$ (mA/cm <sup>2</sup> )	FF (%)	Eff (%)	$R_{sh}$ (k $\Omega$ *cm <sup>2</sup> )	$R_s$ ( $\Omega$ *cm <sup>2</sup> )
B-7	0.86	5.57	64.04	3.08	1.20	15.64
B-10	0.87	6.10	59.81	3.17	1.35	18.35
B-11	0.87	6.12	60.58	3.25	1.21	20.07
B-12	0.86	6.33	53.36	2.91	0.99	23.12
B-13	0.87	6.12	60.58	3.25	1.21	20.07
<b>B-14</b>	<b>0.87</b>	<b>6.36</b>	<b>62.67</b>	<b>3.46</b>	<b>1.16</b>	<b>15.75</b>
B-15	0.88	6.41	58.85	3.36	0.89	20.41

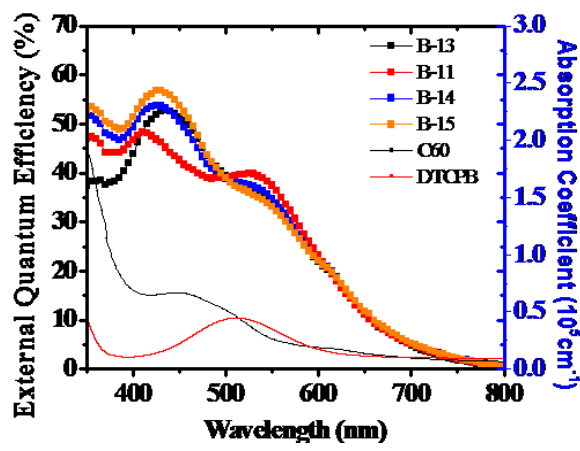


(a)

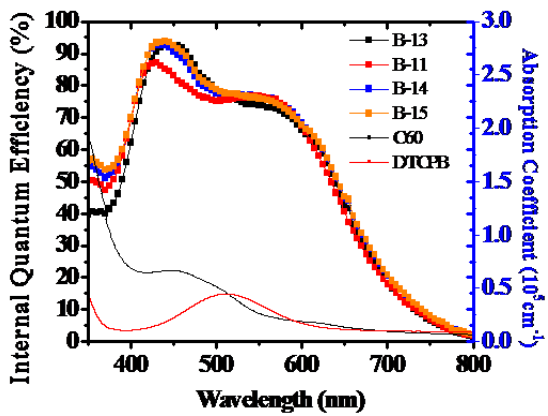
(b)



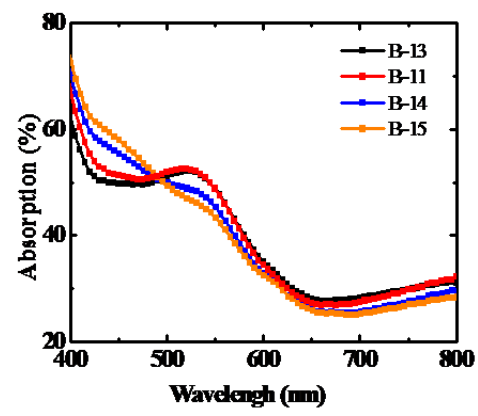
(c)



(d)



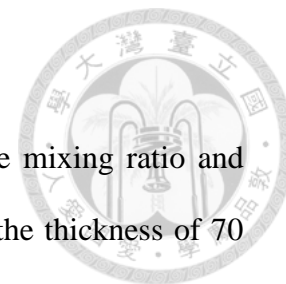
(e)



(f)

Fig. 3-19 (a) and (d) EQE, (b) and (e) IQE and (c) and (f) absorption spectrum of devices in this section.

### 3.3.4.2 C<sub>70</sub> based OSC

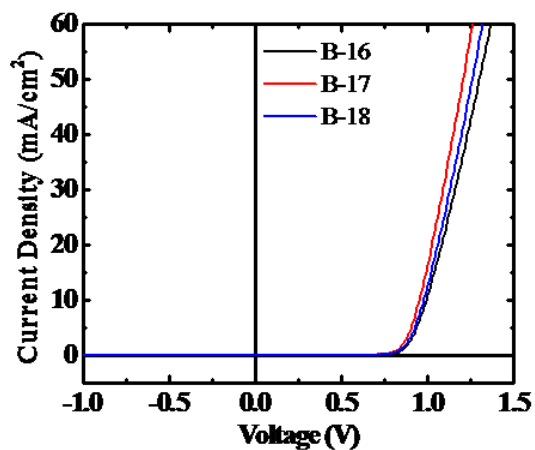


In this section, we optimize the DTCTB: C<sub>70</sub> by varying the mixing ratio and thickness. The optimized condition is DTCPB: C<sub>70</sub> = 1: 2.6 with the thickness of 70 nm, as shown below.

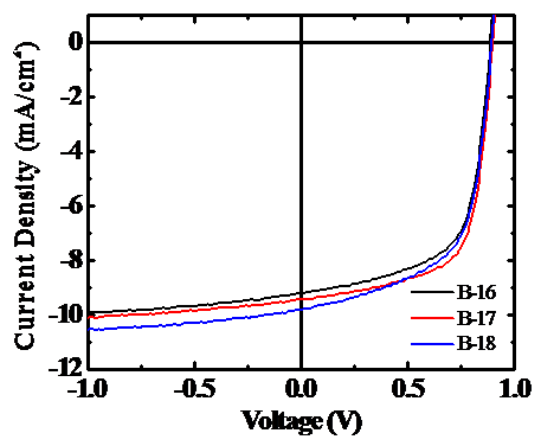
Table. 3-17 Device configurations of DTCPB: C<sub>70</sub> based OSC from B-16 to B-20.

The unit is nm.

Device	MoO <sub>3</sub>	DTCPB:C <sub>70</sub>	BCP	Al
B-16		<b>1:2.2</b> (Mixing ratio), 60		
B-17		<b>1:2.6</b> (Mixing ratio), 60		
B-18	20	<b>1:3.0</b> (Mixing ratio), 60	7	100
B-19		1:2.6 (Mixing ratio), <b>70</b>		
B-20		1:2.6 (Mixing ratio), <b>80</b>		



(a)



(b)



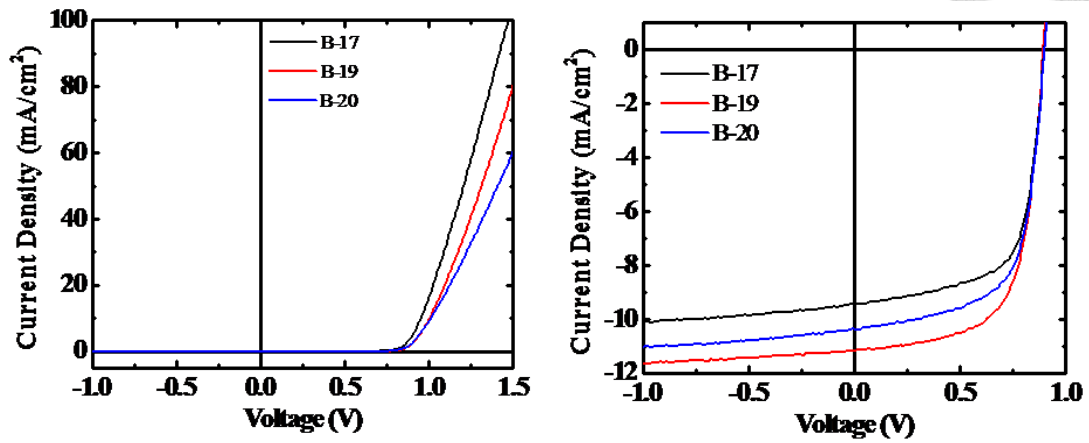
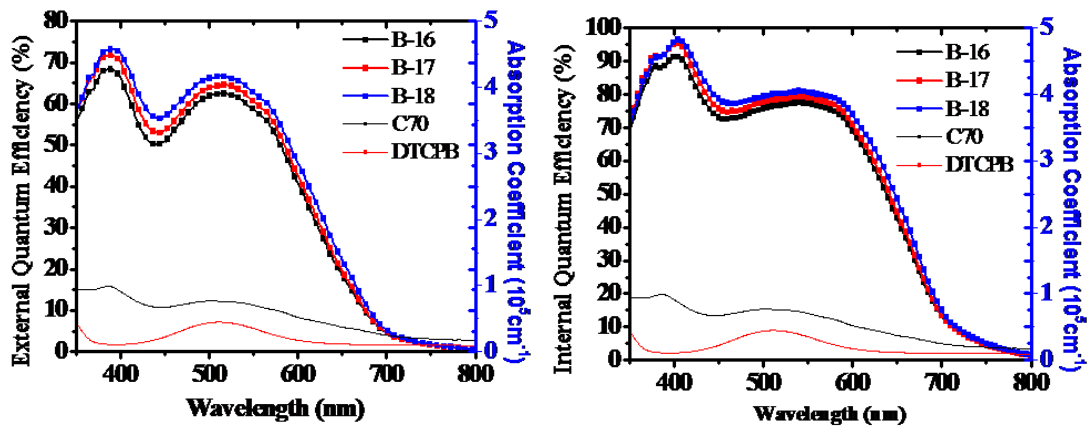


Fig. 3-20 J-V performances of devices from B-16 to B-20 of different mixing ratio under (a) dark condition and (b) 1-sun solar illuminations and different thickness of active layer under (c) dark condition and (d) 1-sun solar illuminations.

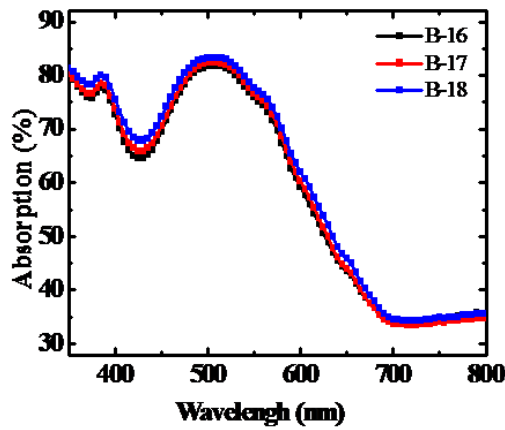
Table. 3-18 Performance of devices from B-16 to B-20 with various mixing ratio and thickness of active layer under 1-sun solar illumination.

Name	$V_{oc}$ (V)	$J_{sc}$ ( $\text{mA}/\text{cm}^2$ )	FF (%)	Eff (%)	$R_{sh}$ ( $\text{k}\Omega \cdot \text{cm}^2$ )	$R_s$ ( $\Omega \cdot \text{cm}^2$ )
B-16	0.89	9.02	63.71	5.22	0.92	7.76
B-17	0.90	9.40	66.21	5.65	0.95	8.56
B-18	0.90	9.91	59.96	5.38	0.62	8.41
B-19	0.90	11.12	65.63	6.55	1.35	14.60
B-20	0.90	10.56	63.89	6.09	0.95	14.86

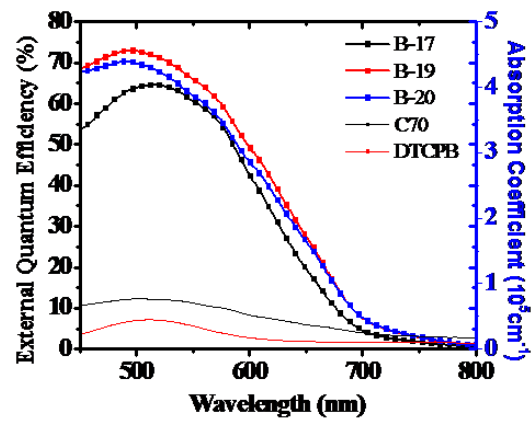


(a)

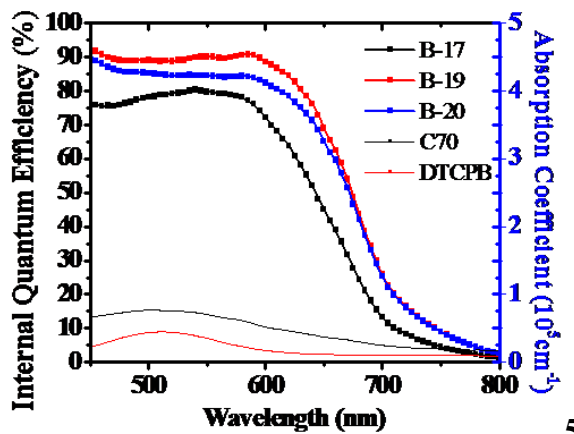
(b)



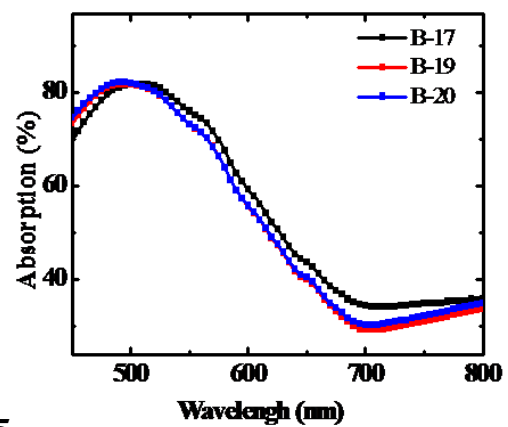
(c)



(d)



(e)



(f)

Fig. 3-21 (a) EQE, (b) IQE and (c) absorption spectrum of devices with various mixing ratio of mixing layers and (d) EQE, (e) IQE and (e) absorption spectrum of devices with different thickness of active layers for C<sub>70</sub> based OSC.



### 3.3.4.3 Insertion of blocking layer for DTCPB: C<sub>60</sub> based OSC

In this section, we tried to insert mCP layer between MoO<sub>3</sub> and mixing layer to prevent possible exciton quenching. However, the insertion of blocking layer resulted in higher R<sub>S</sub>, and little enhancement (if any) on J<sub>SC</sub>, which resulted in worse PCE.

Table. 3-19 Device configurations of DTCPB based OSC for different thickness of blocking layer from B-5, B-8 to B-9. The unit is nm.

	MoO <sub>3</sub>	mCP	DTCPB:C <sub>60</sub>	C <sub>60</sub>	BCP	Al
B-5		<b>0</b>				
B-8	20	<b>1</b>	1:1.6 (Mixing ratio), 60	10	7	100
B-9		<b>3</b>				

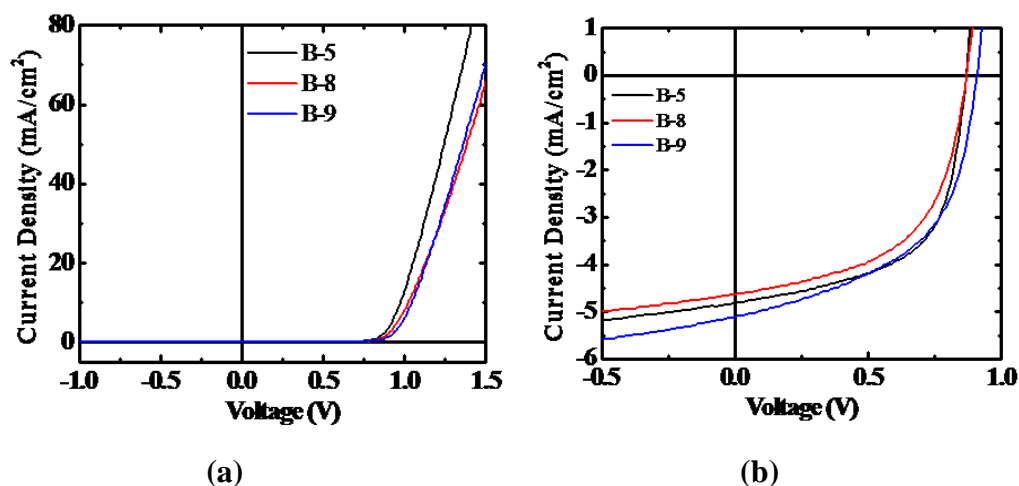
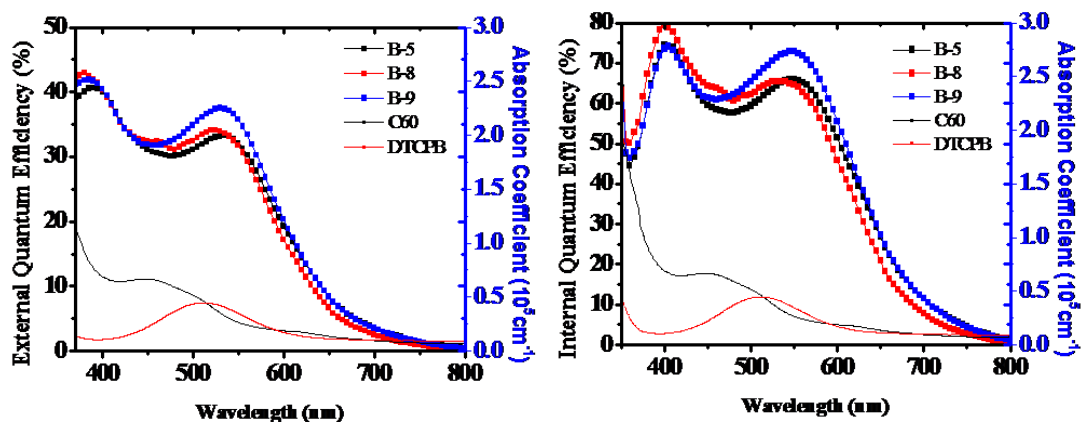


Fig. 3-22 J-V performances of devices from B-5, B-8 to B-9 under (a) dark condition and (b) 1-sun solar illuminations

Table. 3-20 Performances of device from B-5, B-8 to B-9 with various thickness

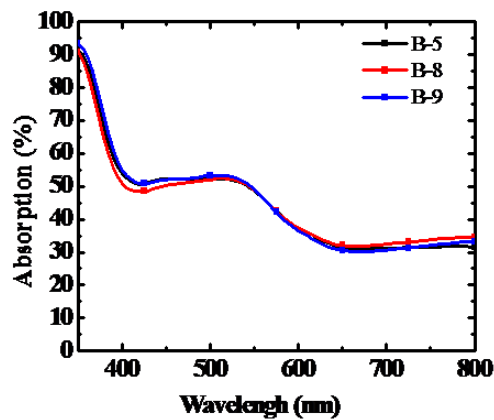
of blocking layer under 1-sun solar illumination

Name	V <sub>oc</sub> (V)	J <sub>sc</sub> (mA/cm <sup>2</sup> )	FF (%)	Eff (%)	R <sub>sh</sub> (kΩ*cm <sup>2</sup> )	R <sub>s</sub> (Ω*cm <sup>2</sup> )
B-5	0.86	4.82	58.89	2.46	1.09	21.31
B-8	0.87	4.70	53.93	2.21	1.07	34.59
B-9	0.89	5.05	47.36	2.13	0.73	41.20



(a)

(b)



(c)

Fig. 3-23 (a) EQE, (b) IQE and (c) absorption spectrum of devices from B-5, B-8 to B-9 with various thickness of blocking layers.

### 3.3.5 Comparison between PMHJ and BHJ for DTCPBO/ C<sub>60</sub> based OSC

In this section, we compared the PMHJ and BHJ structures in DTCPBO based

OSC. It was found that BHJ device exhibited higher PCE, as shown below.

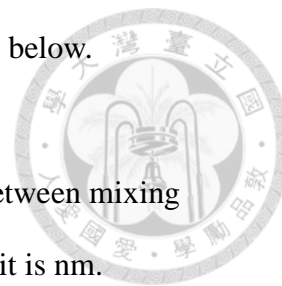


Table. 3-21 Device configurations for different relative ratio between mixing transporting layer from C-1 to C-2 of DTCPBO based OSC. The unit is nm.

Device	MoO <sub>3</sub>	DTCPBO:C <sub>60</sub>	C <sub>60</sub>	BCP	Al
C-1	20	1:1.6 (Mixing ratio), 50	10	7	100
C-2		1:1.6 (Mixing ratio), 60	0		

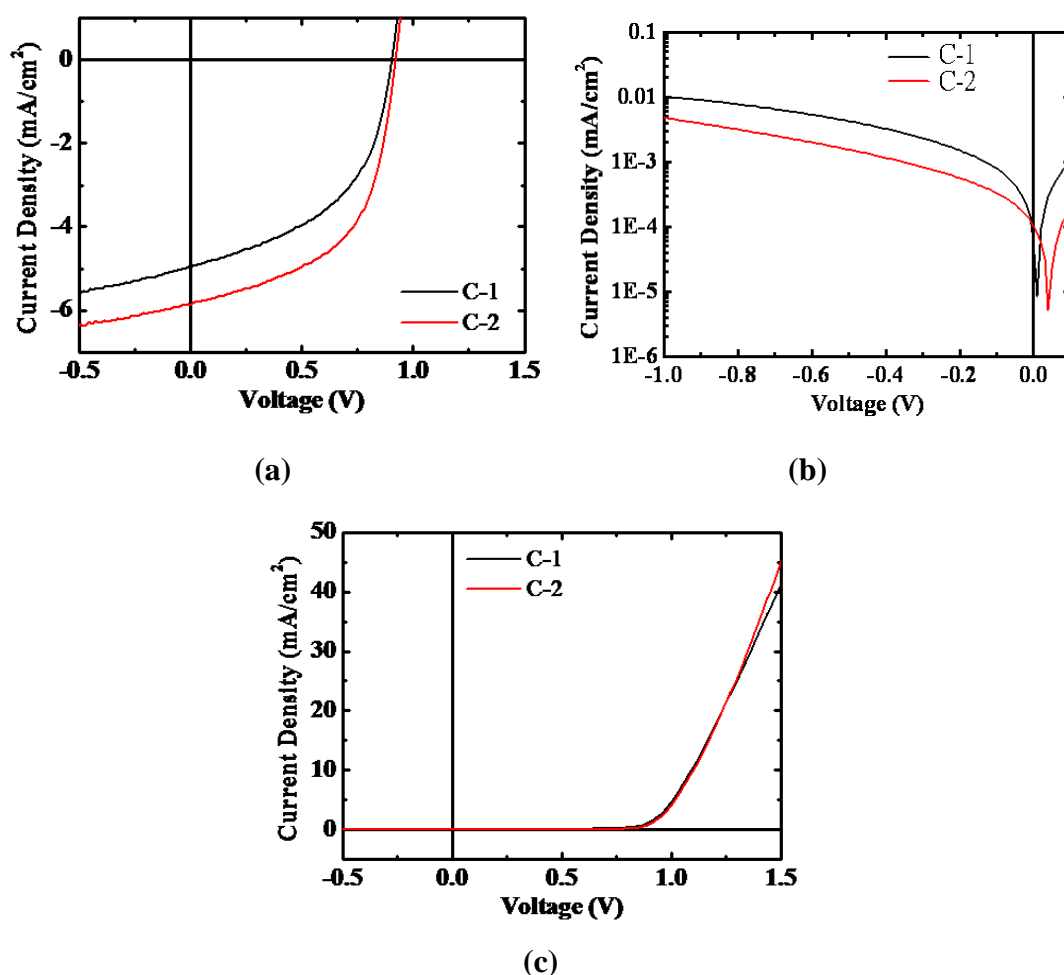


Fig. 3-24 J-V performances of devices from C-1 to C-2 as (a) linear, (b) logarithm plots under dark condition and (c) 1-sun solar illuminations.

Table. 3-22 Performance of device from C-1 to C-2 with various relative ratio between mixing and transport layers under 1-sun solar illumination

Name	V <sub>OC</sub> (V)	J <sub>SC</sub> (mA/cm <sup>2</sup> )	FF (%)	Eff (%)	Rsh (kΩ*cm <sup>2</sup> )	Rs (Ω*cm <sup>2</sup> )
C-1	0.91	4.97	49.30	2.23	0.66	18.24
C-2	0.92	5.76	54.96	2.93	0.87	19.77

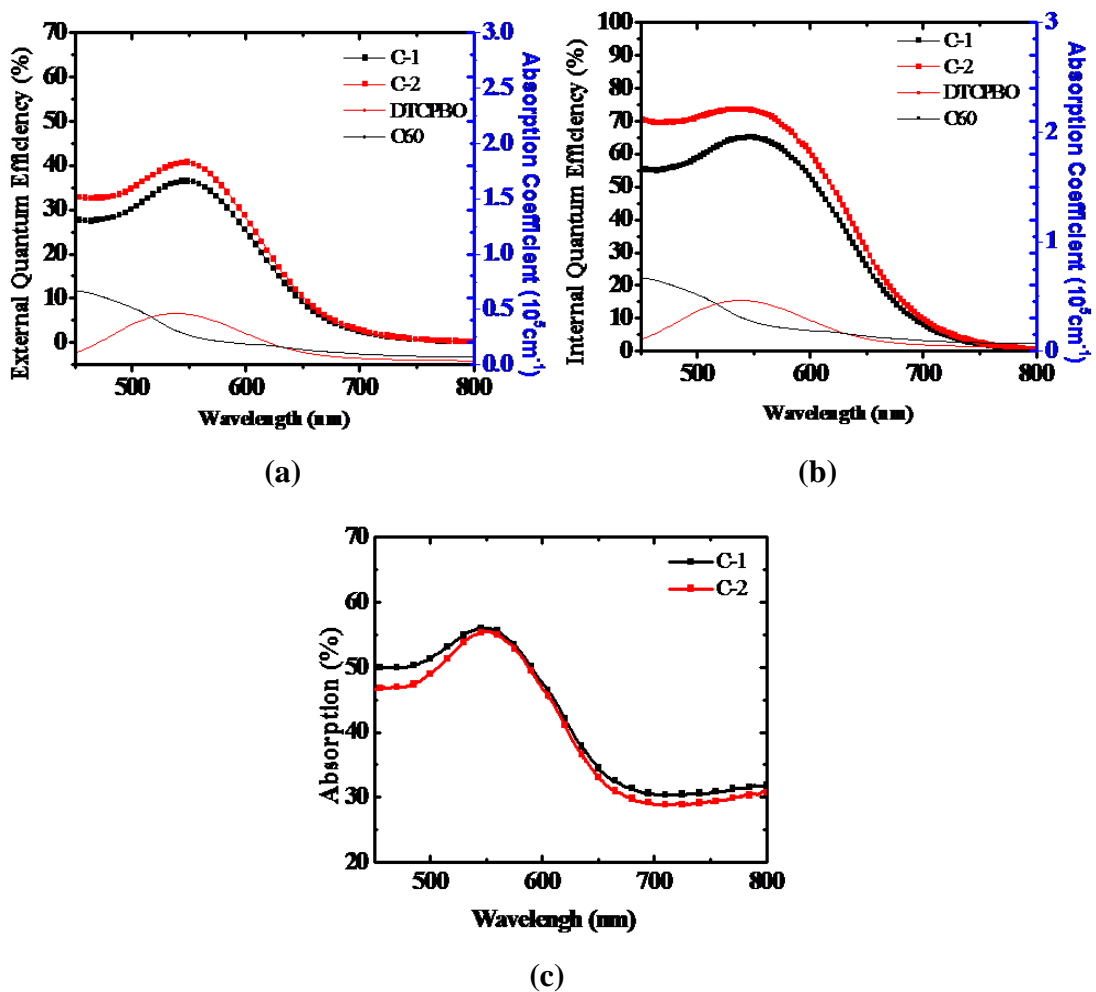


Fig. 3-25 (a) EQE, (b) IQE and (c) absorption spectrum of devices from C-1 to C-2 with various relative ratio between mixing and transport layers under 1-sun solar illumination

### 3.3.6 Optimization of mixing ratio and thickness of active layer

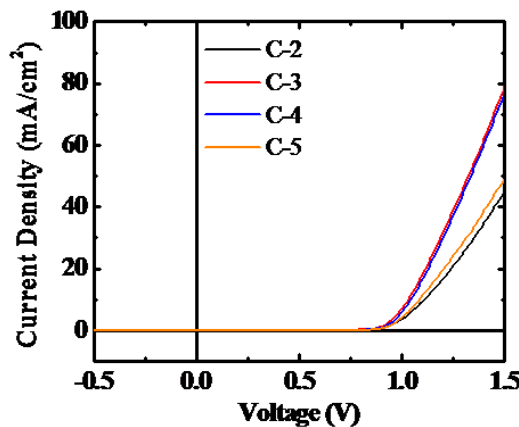
## for DTCPBO

### 3.3.6.1 C<sub>60</sub> based OSC

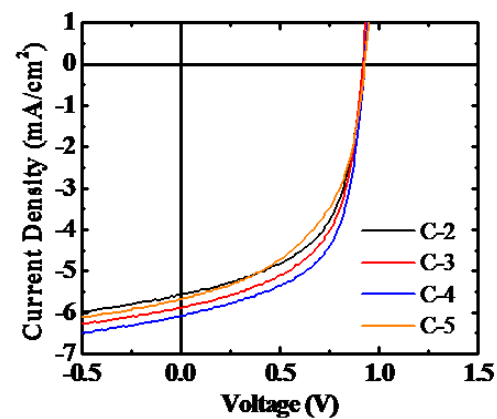
In this section, we varied the mixing ratio and the thickness of the active layer. The optimized values are DTCPBO:C<sub>60</sub>= 1: 2.2 with thickness of 80 nm in C-7, as shown below.

Table. 3-23 Device configurations of DTCPBO, C<sub>60</sub> based OSC for different mixing ratio from C-2 to C-8. The unit is nm.

Device	MoO <sub>3</sub>	DTCPBO:C <sub>60</sub>	BCP	Al
C-2		<b>1:1.6</b> (Mixing ratio), 60 nm		
C-3		<b>1:1.8</b> (Mixing ratio), 60 nm		
C-4		<b>1:2.2</b> (Mixing ratio), 60 nm		
C-5	20	<b>1:2.6</b> (Mixing ratio), 60 nm	7	100
C-6		1:2.2 (Mixing ratio), <b>70 nm</b>		
C-7		1:2.2 (Mixing ratio), <b>80 nm</b>		
C-8		1:2.2 (Mixing ratio), <b>90 nm</b>		



(a)



(b)

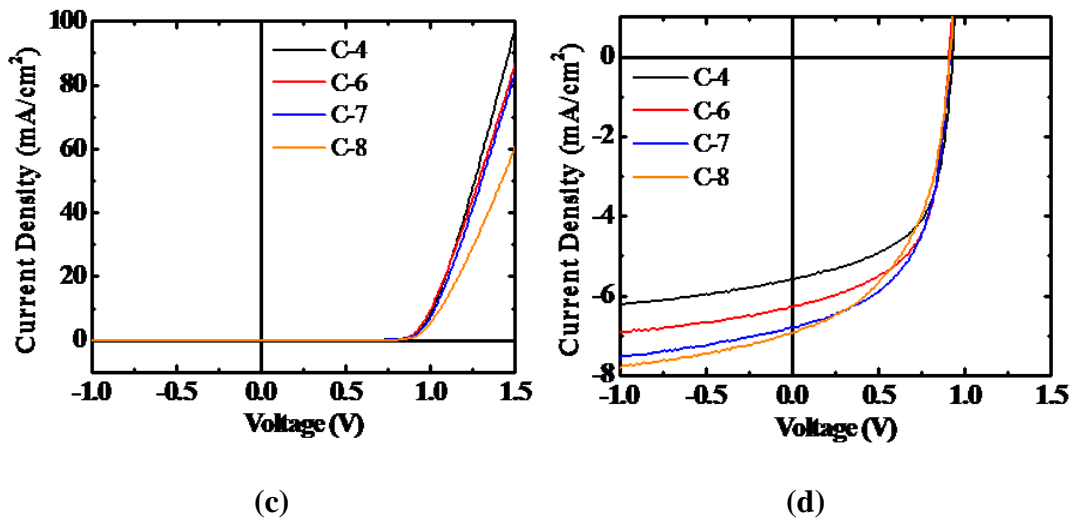


Fig. 3-26 J-V performances of devices for (a) different mixing ratio under dark condition, (b) 1-sun solar illuminations and (c) different thicknesses of active layer under dark condition, (d) 1-sun solar illuminations.

Table. 3-24 Performances of devices with different mixing ratio and different thicknesses of active layer.

Name	V <sub>oc</sub> (V)	J <sub>sc</sub> (mA/cm <sup>2</sup> )	FF (%)	Eff (%)	R <sub>sh</sub> (kΩ*cm <sup>2</sup> )	R <sub>s</sub> (Ω*cm <sup>2</sup> )
C-2	0.92	5.76	54.96	2.93	0.87	19.77
C-3	0.92	5.83	56.02	3.00	0.96	12.85
C-4	0.93	6.02	58.88	3.3	1.02	12.96
C-5	0.93	5.77	51.46	2.76	0.86	17.04
C-6	0.91	6.30	58.97	3.38	0.95	11.35
C-7	0.92	6.84	54.97	3.46	0.88	11.99
C-8	0.91	6.91	49.31	3.11	0.72	14.36



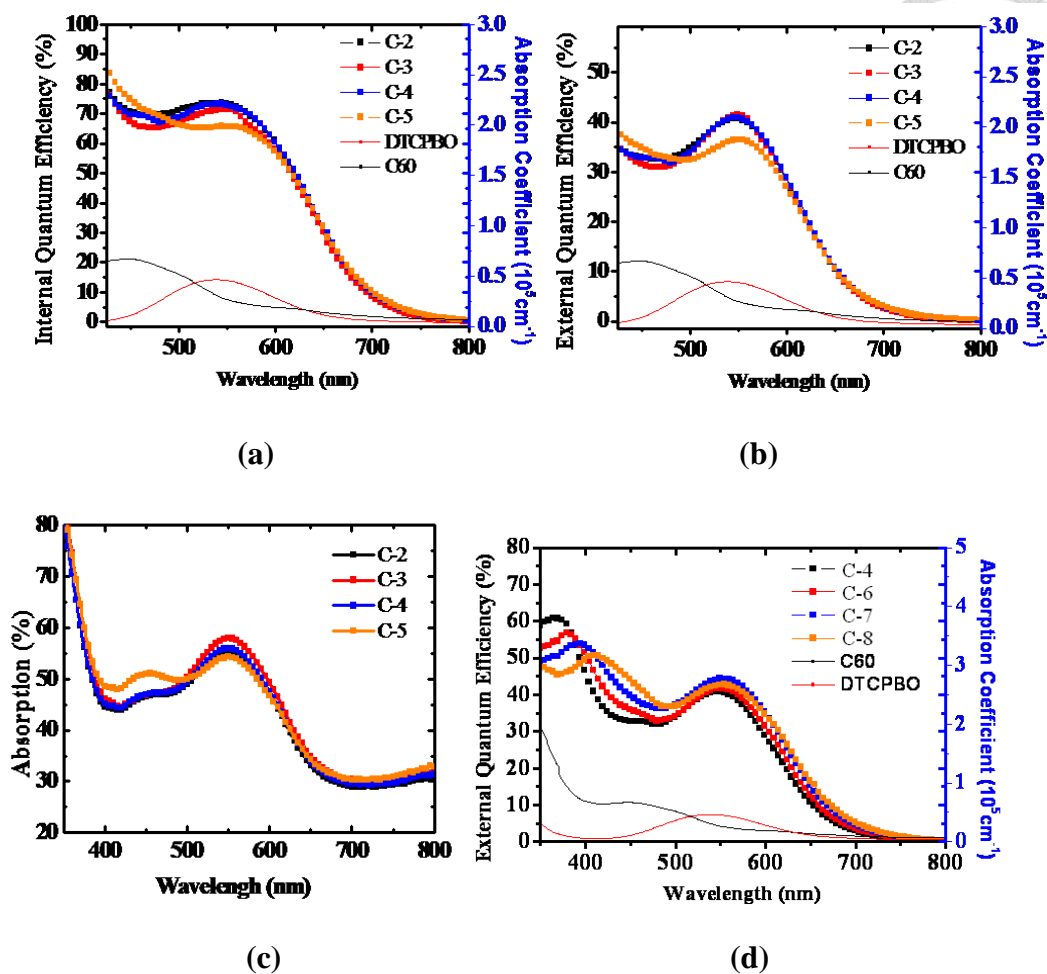


Fig. 3-27 (a) EQE, (b) IQE and (c) absorption spectrum of devices with various mixing ratio of mixing layers and (d) EQE with different thickness of active layers for C<sub>60</sub> based OSC.

### 3.3.6.2 C<sub>70</sub> based OSC

In this section, we varied the mixing ratio and the thickness of the active layer. The optimized values are DTCPBO: C<sub>70</sub>= 1: 2.6 with thickness of 70 nm in C-12, as shown below.

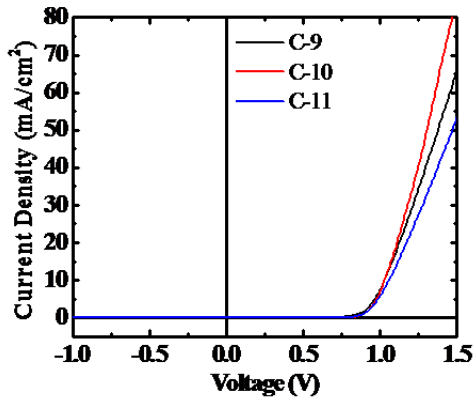
Table. 3-25 Device configurations of DTCPBO based OSC with different mixing ratio and thickness. The unit is nm.

Device	MoO <sub>3</sub>	DTCPBO:C <sub>70</sub>	BCP	Al
--------	------------------	------------------------	-----	----

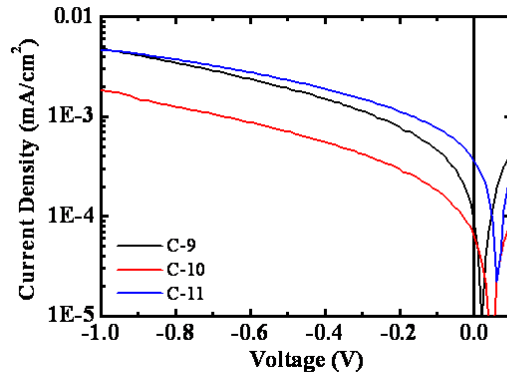
C-9		<b>1:2.2</b> (Mixing ratio), 60 nm
C-10		<b>1:2.6</b> (Mixing ratio), 60 nm
C-11		<b>1:3.0</b> (Mixing ratio), 60 nm
C-12	20	1:2.6 (Mixing ratio), <b>70 nm</b>
C-13		1:2.6 (Mixing ratio), <b>80 nm</b>
C-14		1:2.6 (Mixing ratio), <b>90 nm</b>



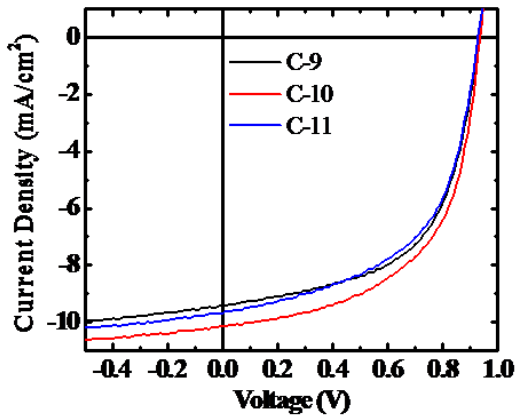
7



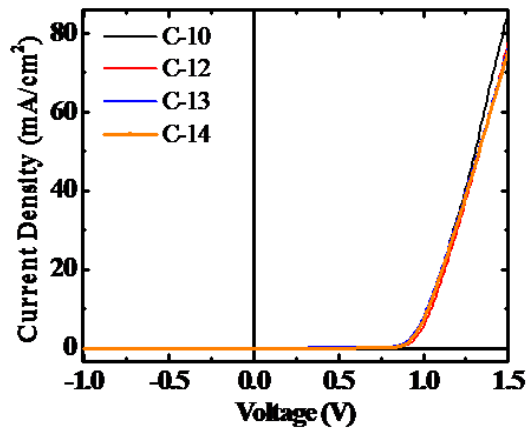
(a)



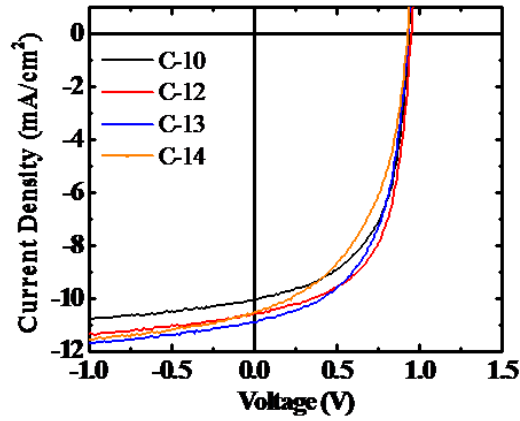
(b)



(c)



(d)



(e)

Fig. 3-28 J-V performances of devices under various ratio for (a) dark condition and (b) 1-sun solar illuminations (c) dark with logarithms plot and various thickness for (d) dark condition and (e) 1-sun solar illuminations

Table. 3-26 Performance of devices from C-9 to C-14 with various mixing ratio and thickness under 1-sun solar illumination.

Name	V <sub>oc</sub> (V)	J <sub>sc</sub> (mA/cm <sup>2</sup> )	FF (%)	Eff (%)	R <sub>sh</sub> (kΩ*cm <sup>2</sup> )	R <sub>s</sub> (Ω*cm <sup>2</sup> )
C-9	0.92	9.49	58.27	5.12	0.72	10.45
C-10	0.94	10.16	55.73	5.35	0.74	11.42
C-11	0.93	9.71	55.16	5.02	0.65	13.11
C-12	0.95	10.52	59.55	5.96	0.87	10.09
C-13	0.94	10.91	54.68	5.61	0.69	10.83
C-14	0.93	10.47	48.93	4.78	0.52	11.54

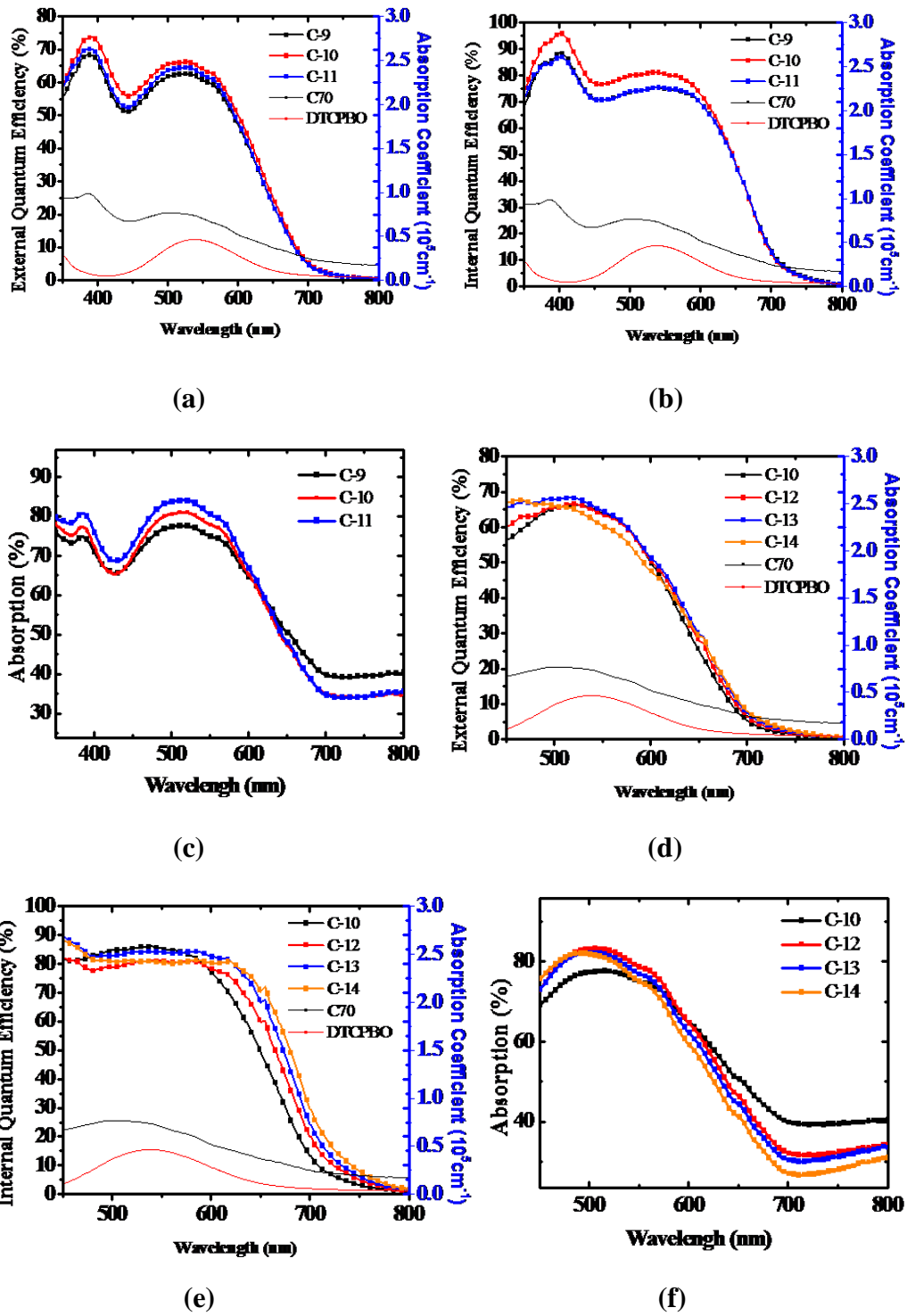


Fig. 3-29 (a) EQE, (b) IQE and (c) absorption spectrum of devices with various mixing ratio of mixing layers and (d) EQE, (e) IQE and (e) absorption spectrum of devices with different thickness of active layers for  $C_{70}$  based OSC.

### 3.3.7 Optimization of mixing ratio and thickness of active layer for DTCTBO

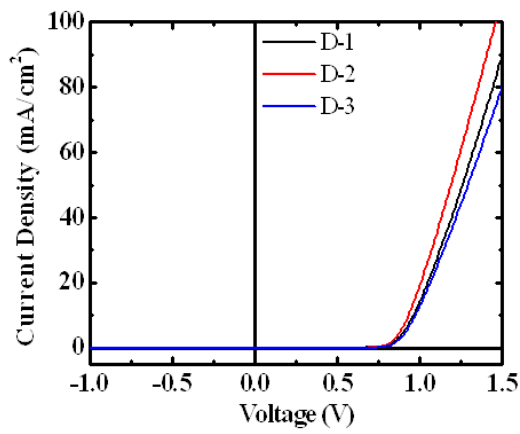


#### 3.3.7.1 C<sub>60</sub> based OSC

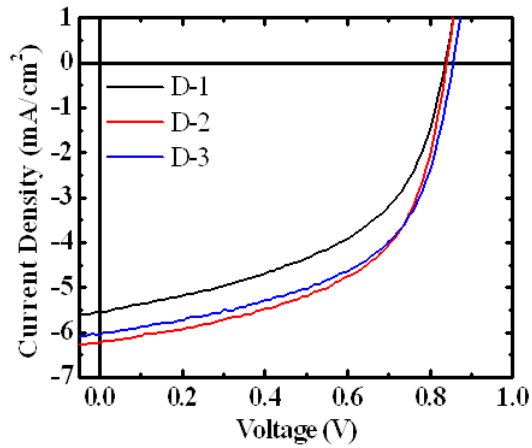
In the last section, we introduced DTCTBO molecule, a cyano terminal substituent with BO central bridging, thiophene electron-withdrawing modified, as electron donor under C<sub>60</sub> based OSC. For energy alignment and optical characteristic, HOMO value is lower than DTCPBO but the absorption is strongest and most red-shift within these four compounds. We varied the mixing ratio and the thickness of the active layer. The optimized values are DTCTBO:C<sub>60</sub>= 1: 2.2 with thickness of 80 nm in D-5, as shown below.

Table. 3-27 Device configurations of DTCTBO, C<sub>60</sub> based OSC for different mixing ratio and thickness of mixing layer from D-1 to D-6. The unit served as nm.

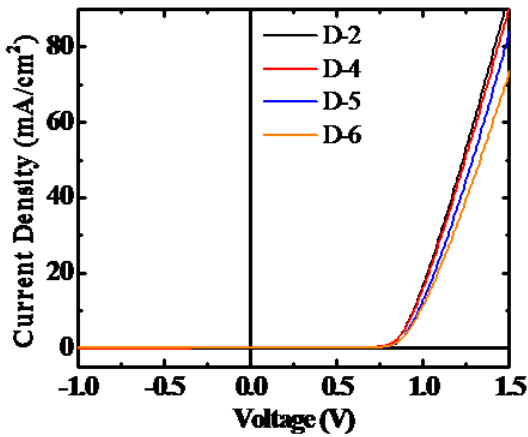
Device	MoO <sub>3</sub>	DTCTBO:C <sub>60</sub>	BCP	Al
D-1		<b>1:1.8</b> (Mixing ratio), 60 nm		
D-2		<b>1:2.2</b> (Mixing ratio) , 60 nm		
D-3		<b>1:2.6</b> (Mixing ratio) , 60 nm		
D-4	20	1:2.2 (Mixing ratio) , <b>70 nm</b>	7	100
D-5		1:2.2 (Mixing ratio) , <b>80 nm</b>		
D-6		1:2.2 (Mixing ratio) , <b>90 nm</b>		



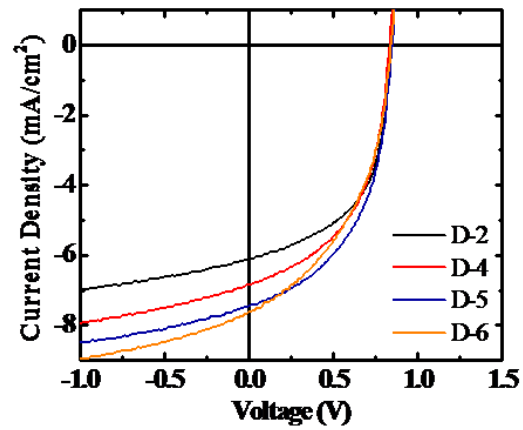
(a)



(b)



(c)



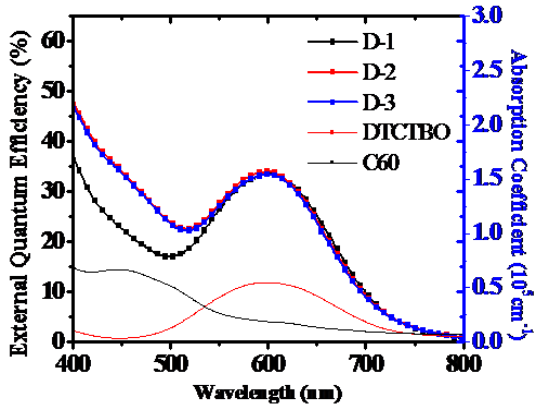
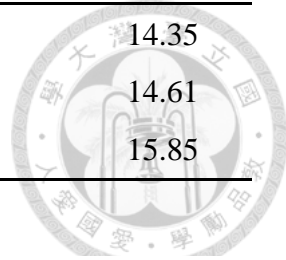
(d)

Fig. 3-30 J-V performance of devices from D-1 to D-6 under various ratio for (a) dark condition and (b) 1-sun solar illumination and under different thickness for (c) dark condition and (d) 1-sun solar illumination.

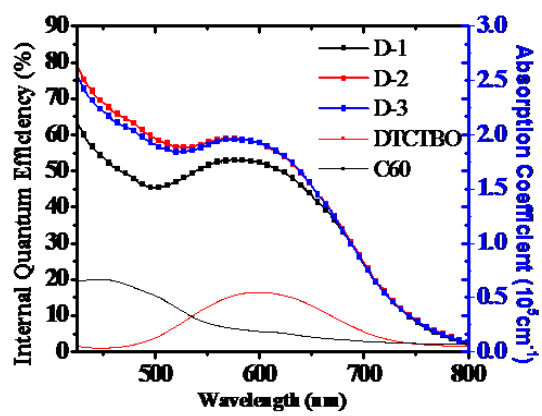
Table. 3-28 Performances of devices with various mixing ratio and thickness of active layer under 1-sun solar illumination.

Name	$V_{OC}$ (V)	$J_{SC}$ (mA/cm <sup>2</sup> )	FF (%)	Eff (%)	$R_{sh}$ (k $\Omega$ *cm <sup>2</sup> )	$R_s$ ( $\Omega$ *cm <sup>2</sup> )
D-1	0.84	5.49	50.83	2.35	0.63	18.84
D-2	0.84	6.23	55.55	2.91	0.74	13.59
D-3	0.86	6.10	54.45	2.87	0.73	18.14

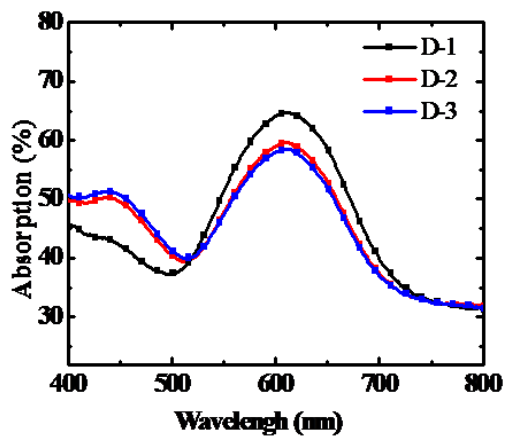
D-4	0.84	6.87	51.07	2.94	0.60	14.35
D-5	0.84	7.56	49.48	3.14	0.58	14.61
D-6	0.84	7.68	45.05	2.92	0.42	15.85



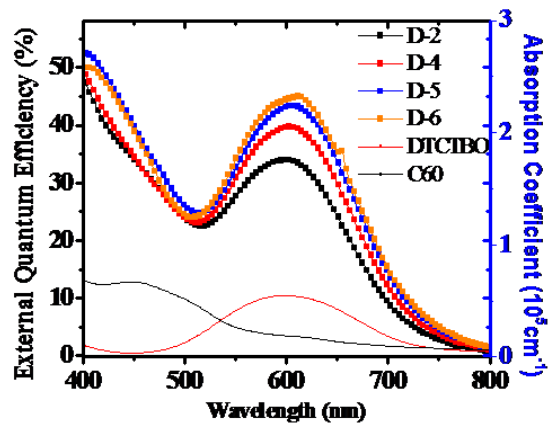
(a)



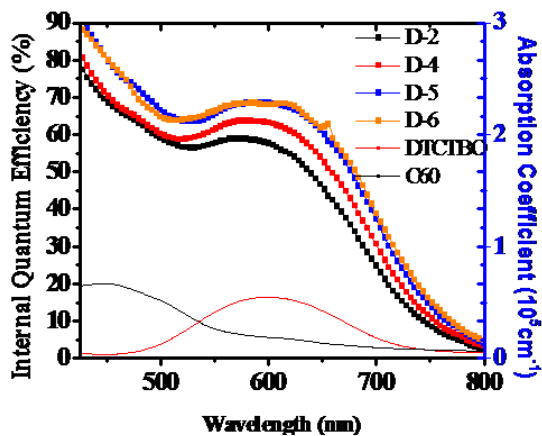
(b)



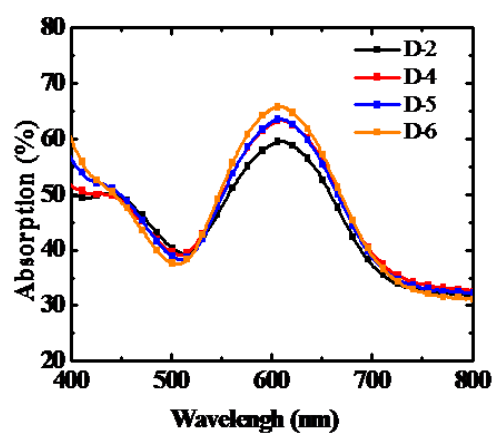
(c)



(d)



(e)



(f)

Fig. 3-31 (a) EQE, (b) IQE and (c) absorption spectrum with various mixing ratio and (d) EQE, (e) IQE and (f) absorption spectrum for different thickness.

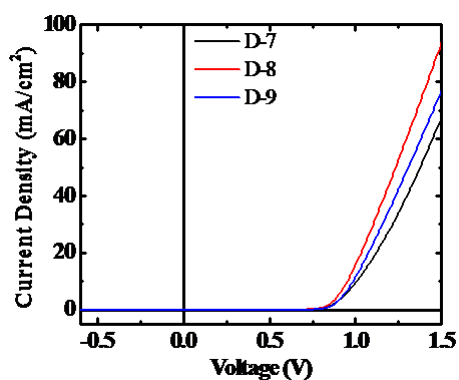


### 3.3.7.2 C<sub>70</sub> based OSC

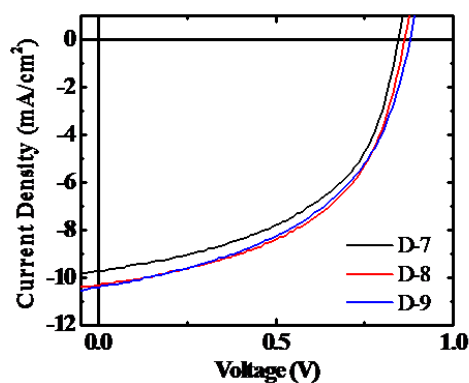
In this section, we varied the mixing ratio and the thickness of the active layer. The optimized values are DTCTBO:C<sub>70</sub>= 1: 2.6 with thickness of 60 nm in D-8, as shown below.

Table. 3-29 Device configurations of DTCTBO, C<sub>70</sub> based OSC for different mixing ratio and thickness from D-7 to D-11. The unit is nm.

Device	MoO <sub>3</sub>	DTCTBO:C <sub>70</sub>	BCP	Al
D-7		<b>1:2.2</b> (Mixing ratio), 60 nm		
D-8		<b>1:2.6</b> (Mixing ratio), 60 nm		
D-9	20	<b>1:3.0</b> (Mixing ratio) , 60 nm	7	100
D-10		1:2.6 (Mixing ratio), <b>70 nm</b>		
D-11		1:2.6 (Mixing ratio), <b>80 nm</b>		



(a)



(b)



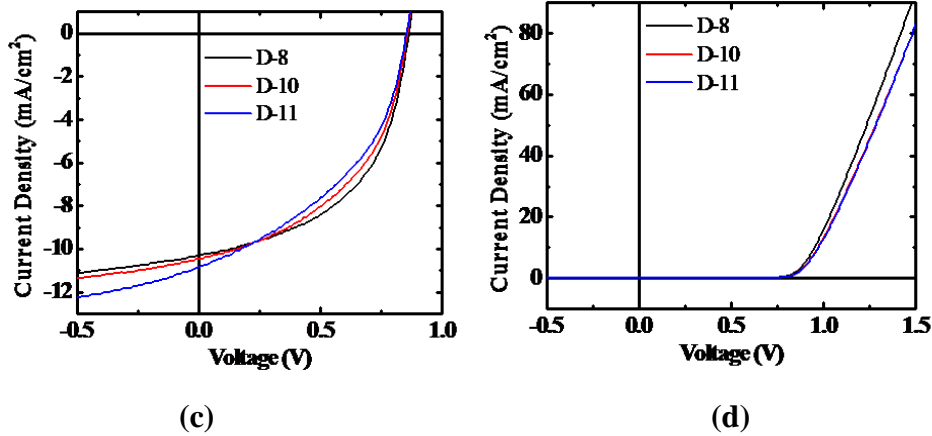
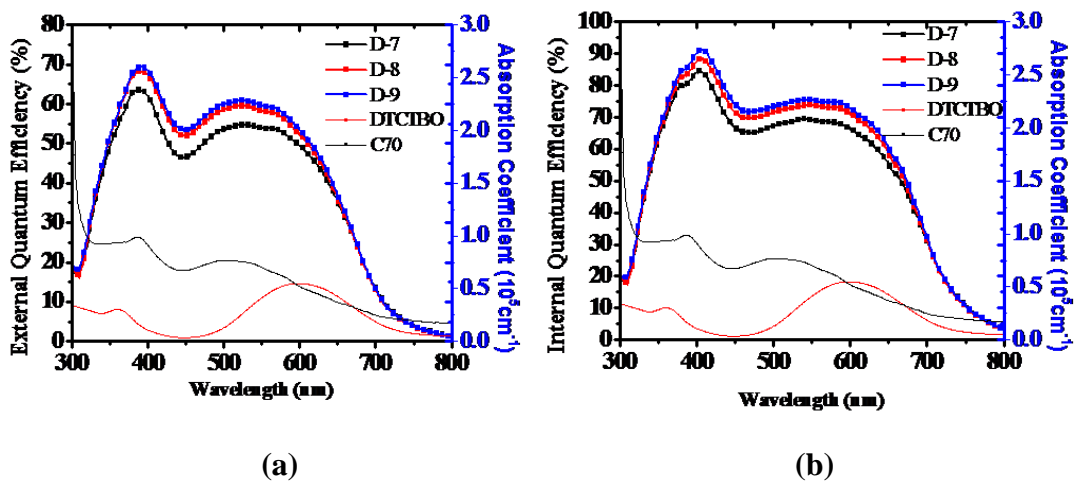


Fig. 3-32 J-V performances of devices to with different mixing ratio under (a) dark condition and (b) 1-sun solar illuminations, and various thickness under (c) dark condition and (d) 1-sun solar illuminations

Table. 3-30 Performances of devices from D-7 to D-11 with various mixing ratio and thickness under 1-sun solar illumination.

Name	V <sub>oc</sub> (V)	J <sub>sc</sub> (mA/cm <sup>2</sup> )	FF (%)	Eff (%)	R <sub>sh</sub> (kΩ*cm <sup>2</sup> )	R <sub>s</sub> (Ω*cm <sup>2</sup> )
D-7	0.85	9.74	50.03	4.14	0.45	12.96
D-8	0.87	10.45	51.10	4.65	0.44	13.98
D-9	0.87	10.64	48.54	4.50	0.38	17.46
D-10	0.85	10.72	46.74	4.28	0.37	14.46
D-11	0.86	10.85	42.56	3.97	0.24	15.14



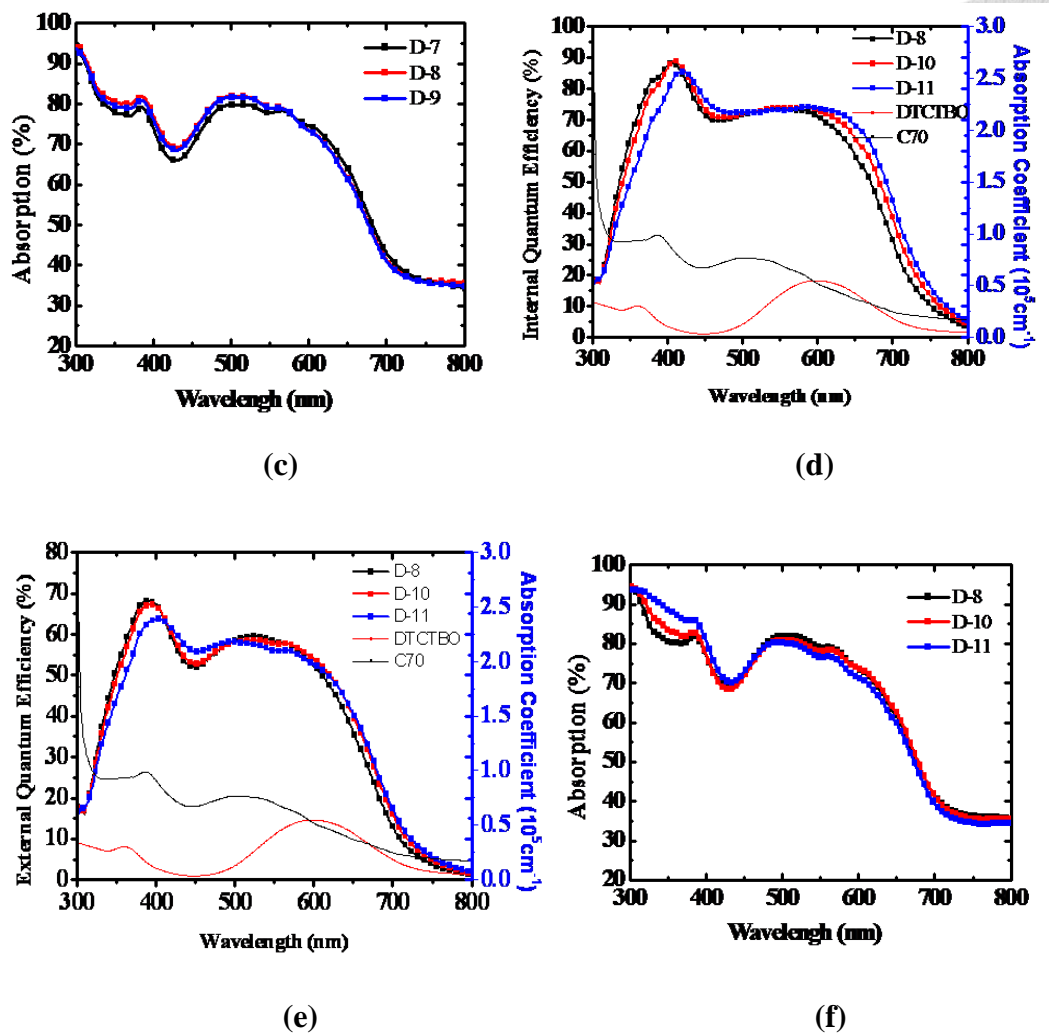


Fig. 3-33 (a) EQE, (b) IQE and (c) absorption spectrum with various mixing ratio and (d) EQE, (e) IQE and (f) absorption spectrum for different thickness.

### 3.4 Comparison of optimized device structures among four single cyano groups electron donor materials

Here, we summarized four single-cyano substituent molecule which served as p-type electron donor mentioned in the above sections in Table. 3-30 and Fig. 3-34. The optimized PCE value was obtained with DTCPB:C<sub>70</sub> -based OSC, as shown below.

Table. 3-31 Device configurations of dye for C<sub>60</sub> and C<sub>70</sub> based OSC for

fine-tune mixing ratio and thickness. The unit served as nm.

Device	MoO <sub>3</sub>	Dye: C <sub>60</sub> or C <sub>70</sub>	C <sub>60</sub> or C <sub>70</sub>	BCP	Al
DTCTB: C <sub>60</sub>	3	1:2.2 (Mixing ratio), 60 nm	10		
DTCTB: C <sub>70</sub>		1:2.6 (Mixing ratio), 70 nm	0		
DTCPB: C <sub>60</sub>		1:2.2 (Mixing ratio), 90 nm	0		
DTCPB: C <sub>70</sub>		1:2.6 (Mixing ratio), 70 nm	0		
DTCTBO: C <sub>60</sub>	20	1:2.2 (Mixing ratio), 70 nm	0	7	100
DTCTBO: C <sub>70</sub>		1:2.6 (Mixing ratio), 60 nm	0		
DTCPBO: C <sub>60</sub>		1:2.2 (Mixing ratio), 80 nm	0		
DTCPBO: C <sub>70</sub>		1:2.6 (Mixing ratio), 70 nm	0		

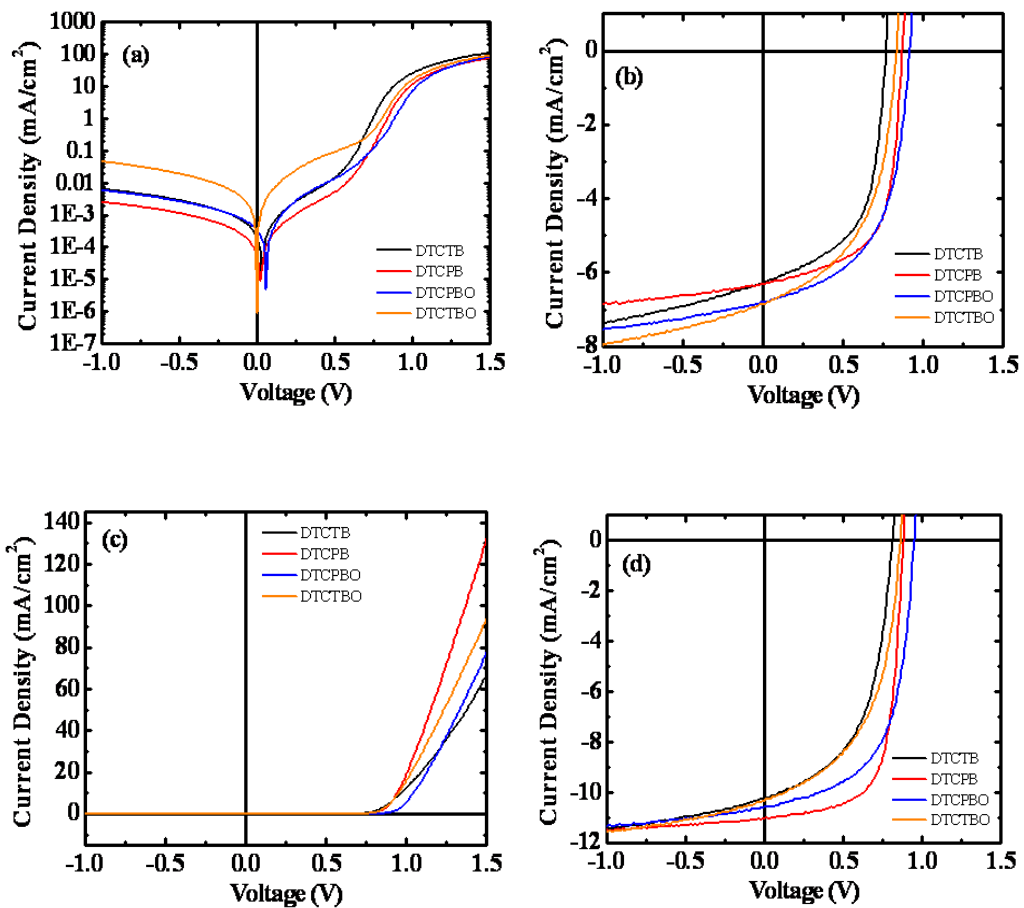


Fig. 3-34 J-V performances of best devices for four compounds (a) C<sub>60</sub> based under dark condition and (b) 1-sun solar illuminations and (c) C<sub>70</sub> based under

dark condition and (d) 1-sun solar illuminations.



Table. 3-32 Performances of dye for C<sub>60</sub> and C<sub>70</sub> based OSC for fine-tune mixing ratio and thickness. The unit is nm.

Device	V <sub>OC</sub> (V)	J <sub>SC</sub> (mA/cm <sup>2</sup> )	FF (%)	Eff (%)	Rsh (kΩ*cm <sup>2</sup> )	Rs (Ω*cm <sup>2</sup> )
DTCTB: C <sub>60</sub>	0.78	6.31	56.53	2.78	0.63	18.3
DTCTB: C <sub>70</sub>	0.81	10.11	53.37	4.40	0.50	9.41
DTCPB: C <sub>60</sub>	0.87	6.36	62.67	3.46	1.16	15.75
DTCPB: C <sub>70</sub>	0.90	11.12	65.63	6.55	1.35	14.60
DTCTBO: C <sub>60</sub>	0.85	7.46	50.56	3.21	0.62	15.23
DTCTBO: C <sub>70</sub>	0.87	10.33	50.32	4.54	0.44	15.50
DTCPBO: C <sub>60</sub>	0.92	6.84	54.97	3.46	0.88	11.99
DTCPBO: C <sub>70</sub>	0.95	10.52	59.55	5.96	0.87	10.09

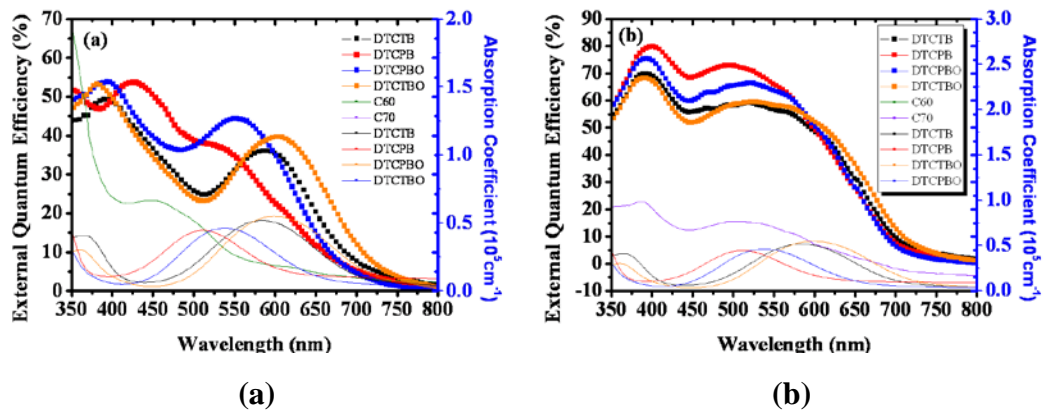


Fig. 3-35 EQE spectrums of best devices for four compounds (a) C<sub>60</sub> based and (b) C<sub>70</sub> based



### 3.5 Sun intensity variation measurements of OSCs with four single

#### cyano groups electron donor materials

In this section, we vary the illumination intensity of OSCs, as shown below. One can see that DTCPB-based OSC showed highest PCE at different illumination intensity.

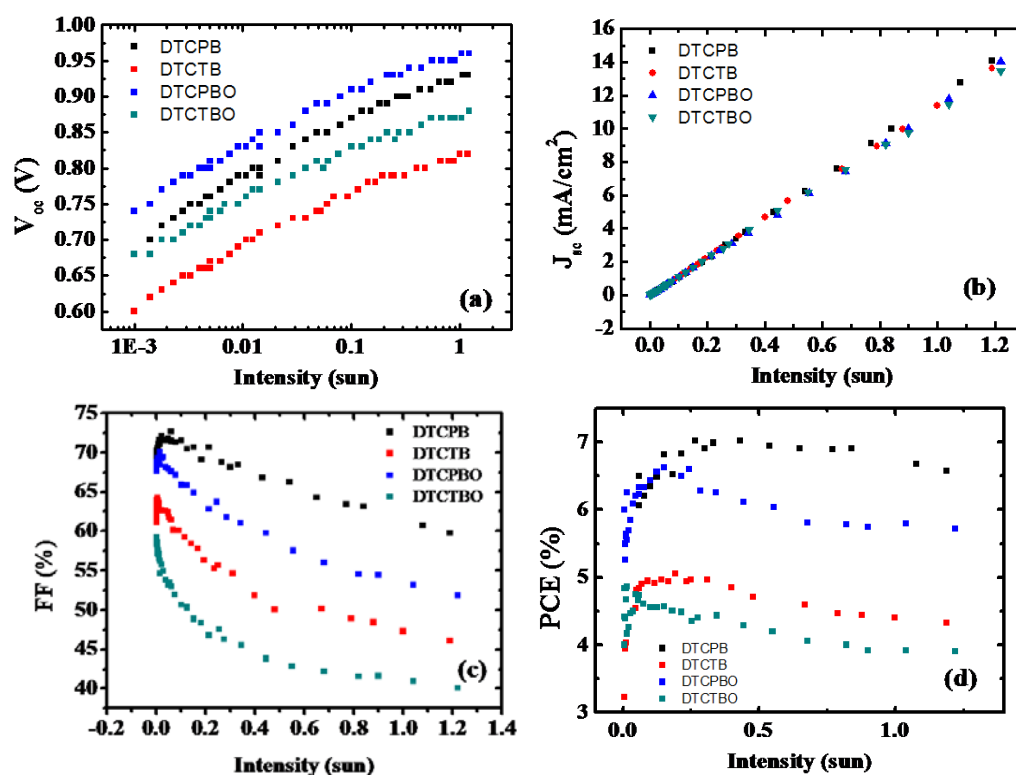


Fig. 3-36 Four parameters under sun variation for four compounds under devices ratio 1:2.2, 70 nm thickness  $C_{70}$  based (a)  $V_{OC}$  (b)  $J_{SC}$  (c) FF (d) PCE.

Table. 3-33 Slope for  $V_{OC}$  versus natural logarithm of the light intensity

Dye	DTCPB	DTCTB	DTCPBO	DTCTBO
Slope	1.21	1.10	1.12	1.02
unit ( $eV \times (kT)^{-1}$ )				

## 4 Chapter 4 Exciton dynamics in rubrene thin films



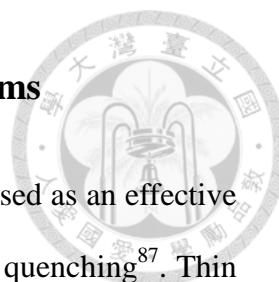
### 4.1 Introduction

The exciton dynamic for 5,6,11,12-tetraphenylanthracene (rubrene) film deposited on glass with lithium fluoride (LiF) 80 nm under SF were investigated under the measurement of steady-state and time-resolved photoluminescence (TrPL). Here, we introduced a rate equation in our model that was applied in our previous work<sup>87</sup>.

$$\frac{dN_s}{dt} = -(k_{sf} + k_{rad})N_s - k_{ssa}N_s^2 + k_{fus}N_T^2 \quad (4-1)$$

$$\frac{dN_T}{dt} = 2k_{sf}N_s - k_{fus}N_T^2 - k_{trip}N_T \quad (4-2)$$

where  $N_S$  and  $N_T$  are singlet and triplet exciton concentrations in rubrene thin film, respectively.  $k_{sf}$ ,  $k_{rad}$ ,  $k_{ssa}$ ,  $k_{fus}$  and  $k_{trip}$  are singlet fission rate, radiative decay (fluorescence) rate, singlet-singlet annihilation (SSA) rate, triplet fusion rate and triplet decay rate, respectively. By measuring the TrPL of rubrene in toluene solution, radiative decay rate can be obtained. SSA can be avoid with ultra-low excitation pulse energy. Hence, singlet fission rate can be obtained from 78 K to room temperature, which can be used to derive the activation energy for singlet fission process. Triplet decay rate is typically very long and hence omitted. Triplet fusion rate can be retrieved by numerical fitting with different excitation pulse energy and temperature. Caging effect, which was revealed in triplet fusion rate, was observed at thin rubrene film (5 nm).



## 4.2 Basic characteristics of amorphous rubrene thin films

In our previous work, we have shown that 80-nm LiF can be used as an effective spacer between substrate and rubrene thin film to prevent substrate quenching<sup>87</sup>. Thin films 4- 1 and 4- 2 in Table. 4-1 were 2-nm rubrene deposited upon 80-nm LiF on quartz and glass substrate, respectively. As shown in Fig. 4-1, TrPL of 2-nm rubrene was almost identical on the glass and quartz substrate with the insertion of 80 nm LiF between them. Hence, in this thesis, we use glass as our substrate. 80 nm LiF was deposited on glass substrate as the exciton blocking layer, followed by rubrene thin film evaporation without breaking the vacuum.

Table. 4-1 Sample structures of thin films 4-1 and 4-2.

Thin film	Structure
4- 1	Quartz / LiF 80 nm / rubrene 2 nm
4- 2	Glass / LiF 80 nm / rubrene 2 nm

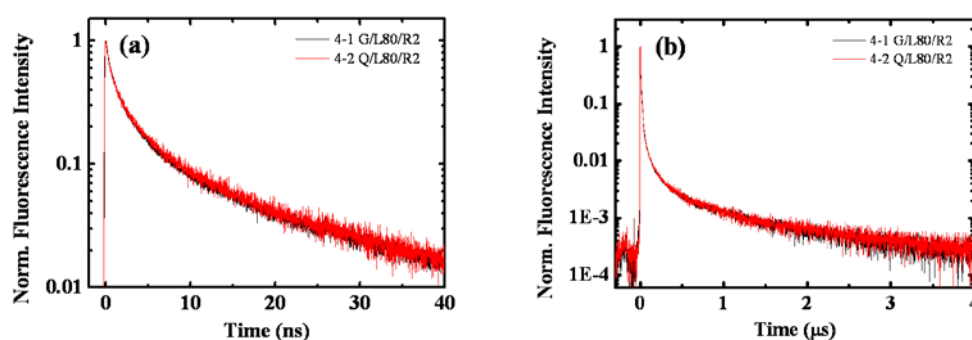


Fig. 4-1 Normalized TrPL fluorescence decay response for thin-films 4-1 and 4-2 in (a) 40 ns window, and (b) 4 μs window.

Also, to prevent from the inhomogeneous excitation during the measurement, the absorption coefficient was measured in Fig. 4-2. According to the Beer–Lambert law shown in equation 4-3, we can obtain the absorption coefficient ( $\alpha$ ) value as the slope of absorbance ( $A$ ) versus thickness ( $l$ ) in Fig. 4-2, where  $I_0$  and  $I$  are the intensity without and with pass through the sample (or reference), respectively. We can found that  $\alpha$  equals to  $0.00275 \text{ nm}^{-1}$  which meant the optical depth ( $1/\alpha$ ) was around 363.3 nm (for optical intensity decays to 36% of its original value). So we should limit the thin film thickness less than this value.

$$A = \alpha l = -\log_{10} \frac{(I_0 / I)_{\text{sample}}}{(I_0 / I)_{\text{ref}}} \quad (4-3)$$

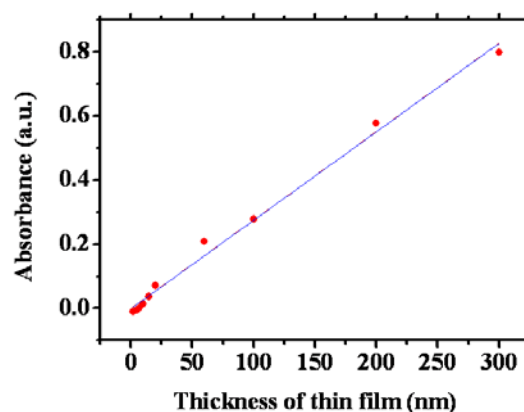


Fig. 4-2 Absorbance ( $A$ ) versus rubrene thickness ( $l$ ).

### 4.3 TrPL of rubrene in toluene

In this section we introduce the radiative decay rate ( $k_{rad}$ ) of rubrene, which means the fluorescence rate from excited state to ground state under optical pumping. The rubrene powder was dissolved in the low polarization solvent toluene with a concentration  $10^{-5} \text{ M}$  to prevent from concentration quenching and aggregation. TrPL signals at short and long time scale were shown in Fig. 4-3.



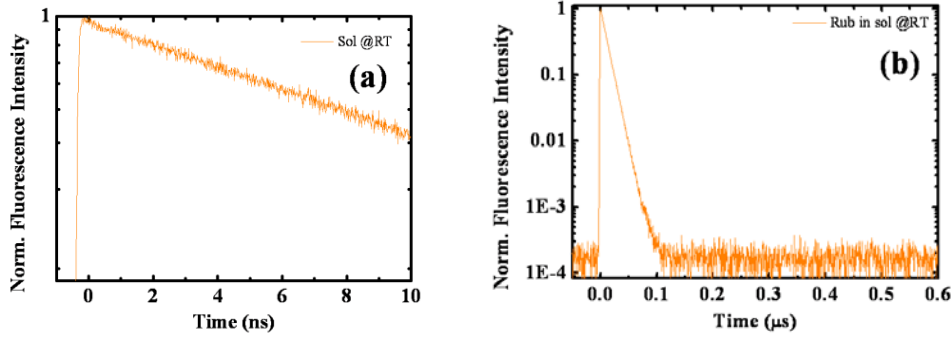


Fig. 4-3 Normalized TrPL fluorescence decay response for  $10^{-5}$  M rubrene in toluene in (a) 10 ns window, and (b) 0.6  $\mu$ s window.

For rubrene in toluene with low concentration ( $10^{-5}$  M), there is no singlet fission, triplet fusion, nor singlet-singlet annihilation. Hence, the rate equation in equation 4-1 can be simplified to:

$$\frac{dN_s}{dt} = -k_{rad} N_s \quad (4-4)$$

Hence, we can obtain that the  $k_{rad}$  was  $0.088 \text{ ns}^{-1}$  (corresponding to decay time of 11.31 ns) in Fig. 4-3. Similar result was found in Ref. <sup>88</sup> (16.3 ns in that paper), and this value was temperature independent. Under steady state, absorbance for rubrene in solution was related to rotationally average molecular orientation which was dominated by the same transition dipole moment along the molecular axis and corresponded to the peaks at 461, 490 and 520 nm, as shown in Fig. 4-4 (b). For rubrene thin film, the absorption spectrum was a little bit red-shift due to the molecule  $\pi - \pi$  stacking as shown in Fig. 4-4 (b). This small shift in absorption response also implied a weak coupling between molecules in rubrene thin film due to its amorphous nature<sup>87</sup>.

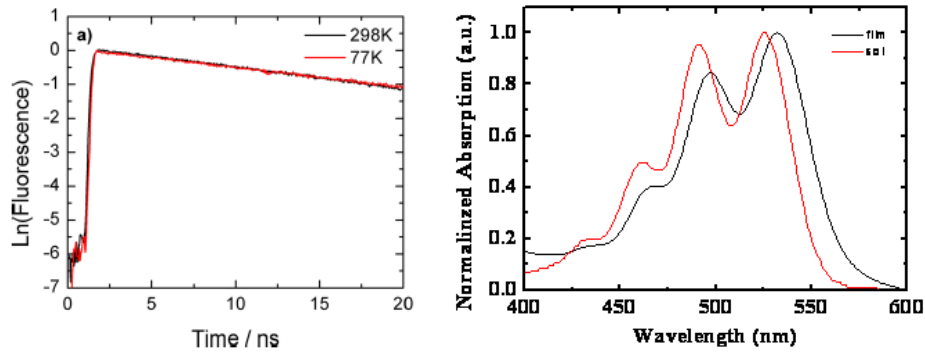
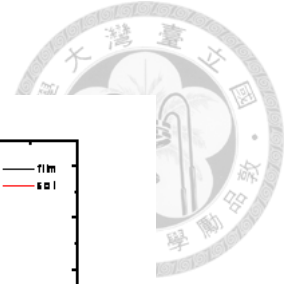


Fig. 4-4 (a) Temperature independent of radiative decay of rubrene in polystyrene and (b) normalized absorption spectrum for rubrene in solution and thin film.

#### 4.4 TrPL of 100-nm rubrene thin film at 78 K with different excitation energy

In this section, we focus on TrPL study of 100 nm at low temperature (78 K). The sample was put in a vacuum chamber ( $1 \times 10^{-5}$  torr) and cooled down by liquid nitrogen. TrPL of the sample under different excitation energy ( $0.00374$ ,  $3.44$  and  $42.6 \mu\text{J}/\text{cm}^2$ ) was shown in Fig. 4-5.

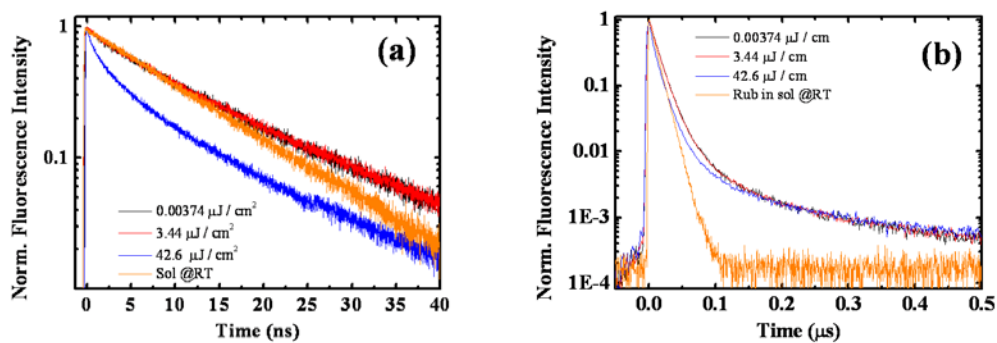


Fig. 4-5 Normalized TrPL fluorescence decay response for rubrene 100 nm at 78 K in (a) 40 ns window, and (b) 0.5  $\mu\text{s}$  window.

When the excitation energy increased from ultra-low ( $0.00374 \mu\text{J}/\text{cm}^2$ ) to low energy ( $3.44 \mu\text{J}/\text{cm}^2$ ), TrPL intensities are almost identical, as shown in Fig. 4-5 (a) and (b). However, when it increased to high energy ( $42.6 \mu\text{J}/\text{cm}^2$ ), significant lifetime decrease was found in Fig. 4-5 (a), due to the strong singlet-singlet annihilation (SSA), as shown in Eq. 4-1.

SSA involves two neighboring chromophores under singlet excited state ( $S_1$ ). One chromophore may transfer the energy to the other and relax energy to the ground state. And the other chromophore obtain the energy and jump to a higher level. This rate is significant in a short time scale and proportion to the square of singlet density in our rate equation, as shown in Eq. 4-1. In Fig. 4-5 (a) and (b), TrPL intensity of rubrene solution was also shown (orange line). When the time scale is less than 15 ns in Fig. 4-5 (a), TrPL intensity of rubrene in solution is quite similar to that in thin-film state under low excitation ( $0.00374$  and  $3.44 \mu\text{J}/\text{cm}^2$ ). It split when the time scale is longer than 15 ns. In Fig. 4-5 (b), for the TrPL intensity of the rubrene solution shows a single exponential decay. On the other hand, delay fluorescence was observed in rubrene thin film which showed the clear evidence of the exciton fusion characteristics.

#### **4.5 TrPL of 100-nm rubrene thin film at room temperature with different excitation energy**

In this section, we study the exciton dynamics of 100 nm rubrene thin film under room temperature. When the excitation energy was ultra-low ( $0.00329$  and  $0.049 \mu\text{J}/\text{cm}^2$ ), the TrPL intensities were quite similar at short time scale Fig. 4-6 (a), which showed the case with negligible SSA. However, when the excitation increased above  $3.88 \mu\text{J}/\text{cm}^2$ , obvious SSA characteristics was observed with shorter exciton lifetime. And exciton lifetime decreased with increasing excitation pulse energy, as shown in

Table. 4-2. Compared to the case under 78 K, there was no SSA when the excitation energy was  $3.44\mu\text{J}/\text{cm}^2$ , and such phenomenon was observed when the excitation energy was as high as  $42.6\mu\text{J}/\text{cm}^2$ . Hence, one can deduce that SSA rate increases with higher temperature. Besides, there is some small difference at long time scale (Fig. 4-6 (b)), which will be described in the following sections.

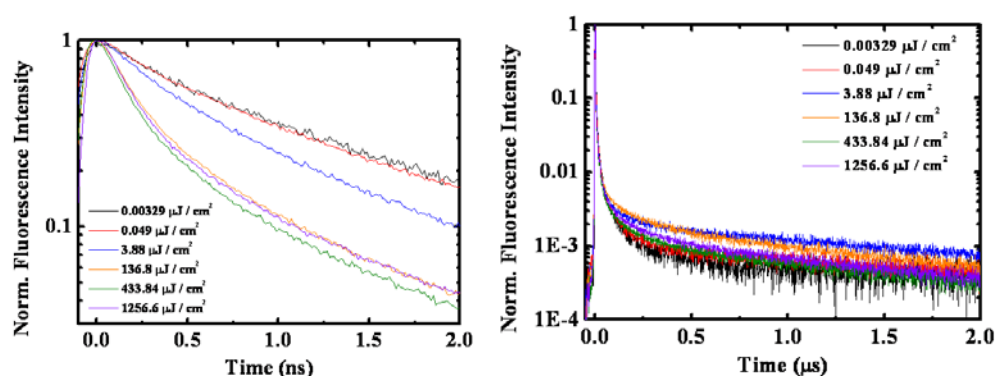


Fig. 4-6 Normalized TrPL fluorescence decay response for rubrene 100 nm at room temperature in (a) 2 ns window, and (b)  $2\mu\text{s}$  window.

Table. 4-2  $\tau_1$  of different excitation densities for 100 nm rubrene at room temperature.

Power ( $\mu\text{J}/\text{cm}^2$ )	0.00329	0.049	3.88	136.8	433.8	1256.6
$\tau_1$ (ns)	0.650	0.643	0.445	0.181	0.147	0.167
$k_1$ (ns)	1.539	1.555	2.247	5.539	6.807	6.001

#### 4.6 TrPL of 100-nm rubrene thin film at different temperatures with ultra-low excitation energy

In this section, we used an ultra-low excitation power,  $0.047\mu\text{J}/\text{cm}^2$  (which resulted in negligible SSA for the temperature ranges from 78 K to room temperature) to excite the 100-nm rubrene thin-film at different temperatures (78 K to room

temperature). Fig. 4-7 (a), (b) and (c) showed the TrPL intensities with 1 ns, 5 ns, and 2  $\mu$ s, respectively. With higher temperature temperatures, we found the shorter  $\tau_1$  value in Fig. 4-7 (a) and Table. 4-3 due to stronger singlet fission. On the other hand, from delay fluorescence (Fig. 4-7 (c)), the  $\tau_2$  value increased with increasing temperature. It may come from the enhanced thermal-assisted diffusion process which reduced the fusion rate.

Because SSA can be neglected, Eq. 1 can be simplified as shown below:

$$\frac{dN_s}{dt} = -(k_{sf} + k_{rad})N_s + k_{fus}N_T^2 \quad (4-5)$$

As discussed above in Sec. 4-3,  $k_{rad}$  was temperature independent with the value of  $0.088 \text{ ns}^{-1}$ , and  $k_{fus}$  was much smaller which can be neglected in this short time interval ( $\sim 0.5 \text{ ns}$ ), the only term influenced the exciton lifetime was the fission rate,  $k_{sf}$ . Hence, we obtained  $k_{sf}$  values at different temperatures, as shown in Fig. 4-8 and Table. 4-3.

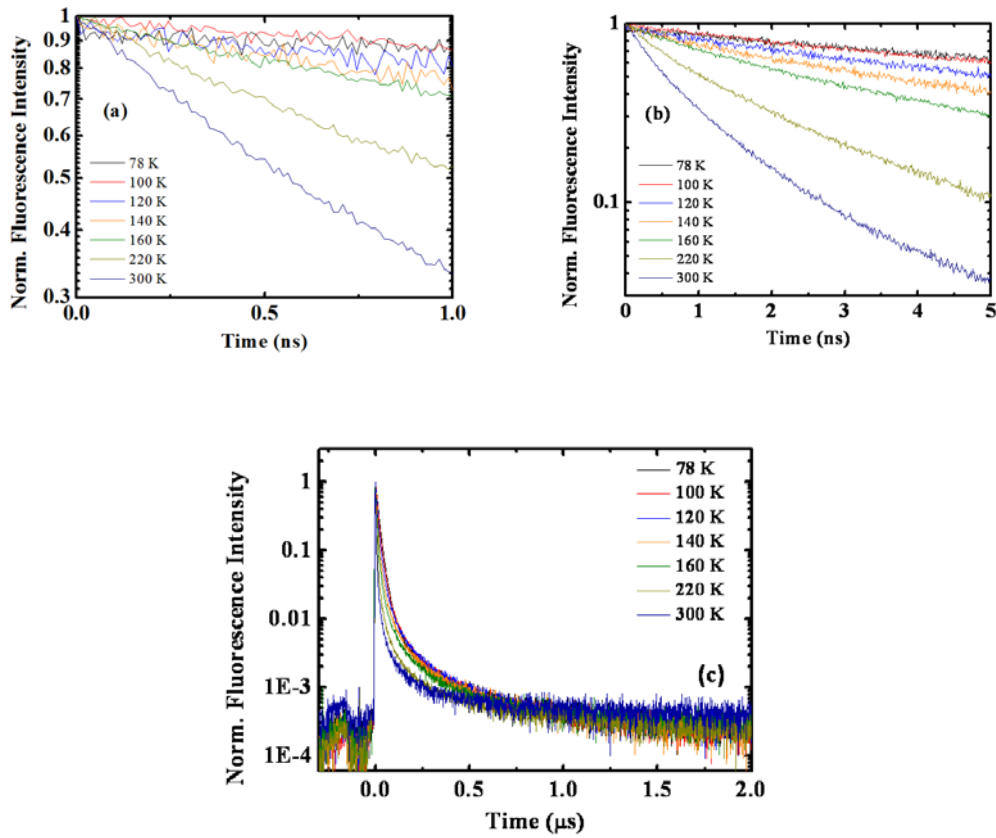


Fig. 4-7 Normalized TrPL fluorescence decay for rubrene 100 nm at  $0.047 \mu\text{J}/\text{cm}^2$  in (a) 1, (b) 5 ns window, and (c)  $2 \mu\text{s}$  window under different temperatures.

One can see that  $k_{sf}$  values increased with increasing temperatures. SF materials with delay fluorescence (such as tetracene and rubrene) typically show the thermal assist characteristic in their energy diagram, because  $S_1$  lies slightly lower than the 2T state and singlet exciton must overcome energy offset to jump to the 2T state for SF process. This energy offset is different from materials and packing situations. Such behavior is typically described by Arrhenius equation shown in the Eq. 4-6:

$$k_{sf} = A \times \exp\left(\frac{\Delta E}{kT}\right) \quad (4.6)$$

where  $A$  is the pre-exponential factor,  $k$  is  $8.617 \times 10^{-5}$  eV/K,  $\Delta E$  is the activation energy, and  $T$  is the temperature.

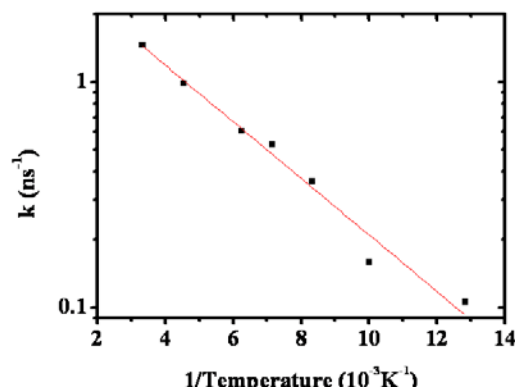


Fig. 4-8 SF rates versus the reciprocal temperature.

Table. 4-3 SF rates for different temperature from 78 K to RT

Temperature (K)	78	100	120	140	160	220	300
$\tau_1$ (ns)	5.181	4.082	2.232	1.631	1.447	0.935	0.650
$k_1$ (ns)	0.193	0.245	0.448	0.613	0.691	1.069	1.539
$k_{sf}$ (ns <sup>-1</sup> )	0.105	0.157	0.360	0.525	0.603	0.981	1.451
$\tau_2$ (ms)	1.015	1.012	1.080	1.226	1.389	1.447	2.167

From Fig. 4-8, Table. 4-3 and Eq. 4-7, one can obtain the activation energy ( $\Delta E$ ) in our case (amorphous rubrene thin film) was -24.9 meV. As shown in Fig. 4-8, single Arrhenius equation fitted pretty well in our rubrene thin film at this temperature range (from 78 K to RT), which meant singlet fission still happened even under low temperature (78 K). It was different from the tetracene case, which showed two slopes in the figure of fission rates in log scale versus reciprocal temperature with the critical temperature at 160 K (that meant singlet fission did not happen below this

temperature)<sup>52</sup>. There were some reports of activation energy values of rubrene in different conditions: as shown by W. G. Herkstroeter et al., the singlet energy  $E(S_1)$  of rubrene in benzene solution was equal to 2.29 eV and the triplet energy  $E(T_1)$  was equal to 1.14 eV<sup>89</sup>. The difference between  $(E(S_1)-2E(T_1))$  showed a positive value for 10 meV. For single crystal rubrene<sup>90</sup>, S. Tao et al. found that  $E(S_1)$  was equal to 2.23 eV and  $E(T_1)$  stayed at 1.14 eV. The difference between them was -50 meV, showed endothermal behavior. Compared to our case (amorphous rubrene thin-film), such activation energy value (-24.9 meV) was just between the cases of rubrene in solution and single crystal phase, as shown in Table. 4-4.

Table. 4-4  $\Delta E$  for different packing conditions of rubrene<sup>6590</sup>.

Molecule Packing condition	Solution	Amorphous	Single crystal
$\Delta E (E(S_1)-2E(T_1))$	10 meV	-24.9 meV	-50 meV

#### 4.7 TrPL of rubrene thin film with different thickness and different excitation energy at room temperature

Fig. 4-9 shows the TrPL intensity at 2 ns window with different rubrene thickness (20, 100, and 200 nm) under room temperature by different excitation pulse energy (0.00329, 0.049, 136.8, and 1256.6  $\mu\text{J} / \text{cm}^2$ ).  $\tau_1$  values are shown in Table 4.5. One can see that it decreases with increasing pulse energy due to SSA, as shown in Sec. 4.5. And it shows similar characteristics with different rubrene thickness, which means SSA is independent to rubrene film thickness.



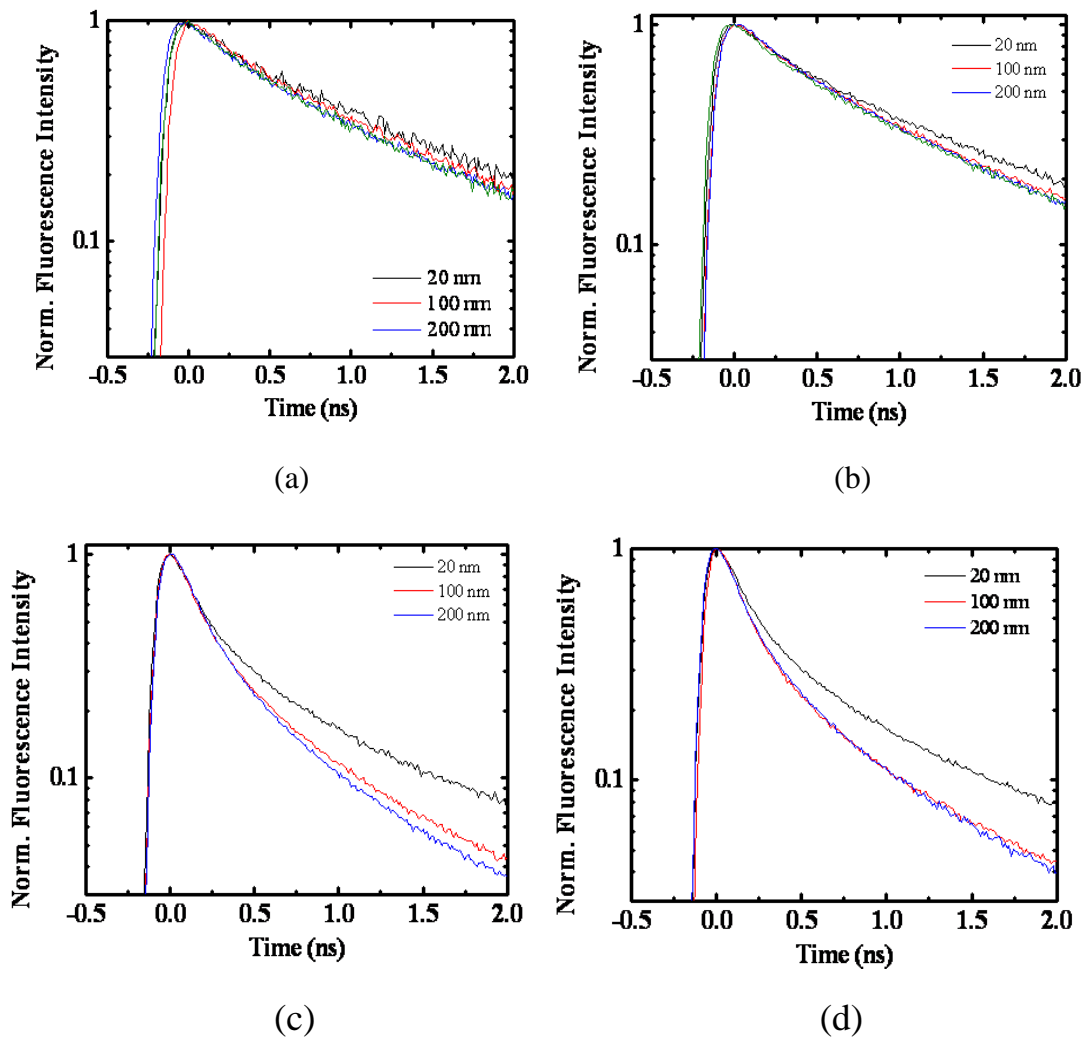


Fig. 4-9 Normalized TrPL fluorescence decay response for 20, 100, 200 nm rubrene under (a) 0.00329, (b) 0.049 (c) 136.8 (d) 1256.6  $\mu\text{J} / \text{cm}^2$  excitation density in 2.0 ns window.

Table. 4-5  $\tau_1$  for different thickness under different excitation density.

Excitation density ( $\mu\text{J} / \text{cm}^2$ )	0.00329	0.049	136.8	1256.6
20 nm	0.819 ns	0.757 ns	0.312 ns	0.314 ns
100 nm	0.830 ns	0.730 ns	0.310 ns	0.251 ns
200 nm	0.809 ns	0.723 ns	0.299 ns	0.266 ns



$\tau_2$  values were characterized by delayed fluorescence in the long time scale, which can be derived from Eq. 2, as shown in Eq. 4-7:

$$\tau_2 \approx \frac{1}{k_{fus} \times N_T} \quad (4-7)$$

Considering the rubrene thickness at 100 nm (as we discussed the short time scale in Sec. 4-5), we can obtain  $\tau_2$  value from the long time scale, as shown in Fig. 4-10. We can see that  $\tau_2$  value decreased and saturated as the excitation pulse energy increased. The first decrease came from the increase in triplet exciton density  $N_T$ . When the power density was larger than  $1256.6 \mu\text{J} / \text{cm}^2$ ,  $\tau_2$  saturated due to strong SSA which limited singlet exciton density and hence triplet exciton density.

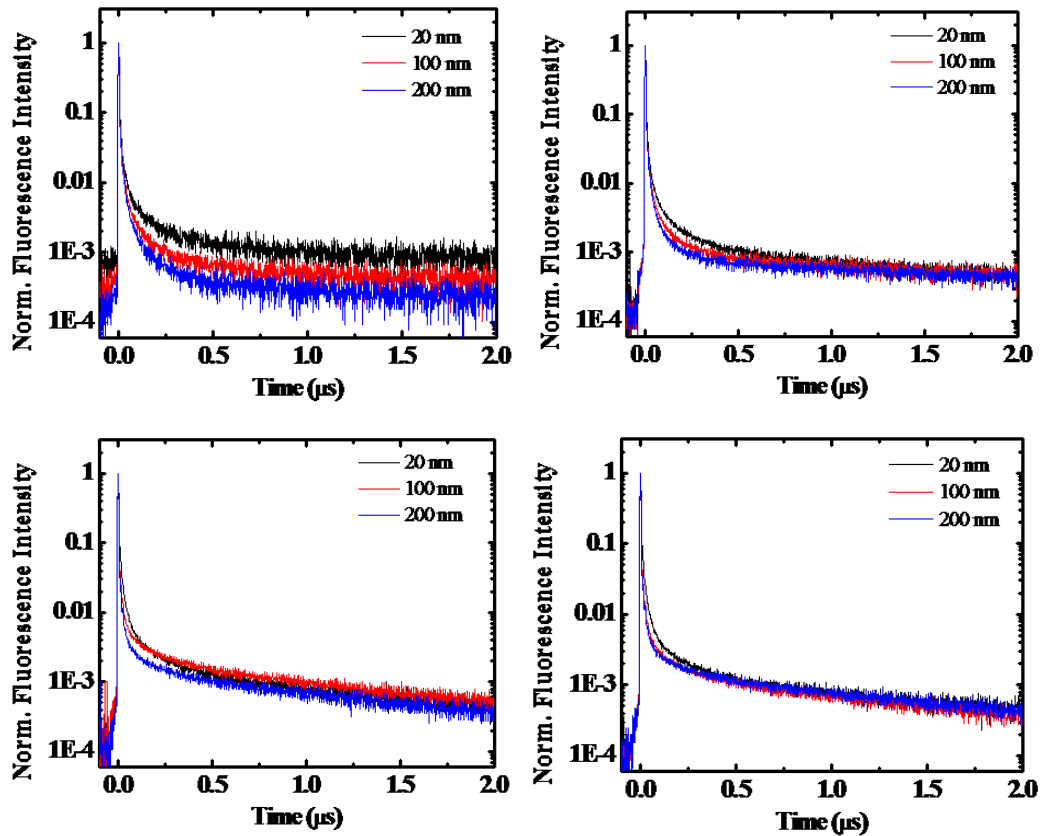


Fig. 4-10 Normalized TrPL fluorescence decay response for 20, 100, 200 nm rubrene under (a) 0.00329, (b) 0.049 (c) 136.8 (d) 1256.6  $\mu\text{J} / \text{cm}^2$  excitation density in 2.0  $\mu\text{s}$  window.

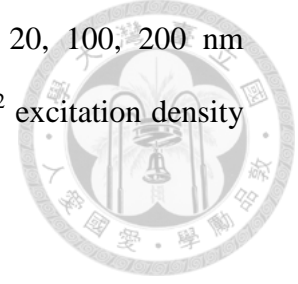


Table. 4-6  $\tau_2$  for different thickness under different excitation density in long time scale.

Excitation density ( $\mu\text{J} / \text{cm}^2$ )	0.00329	0.049	136.8	1256.6
20 nm	1.785 $\square$ s	1.109 $\mu\text{s}$	0.906 $\mu\text{s}$	0.982 $\mu\text{s}$
100 nm	2.061 $\mu\text{s}$	1.792 $\mu\text{s}$	1.026 $\mu\text{s}$	1.016 $\mu\text{s}$
200 nm	2.183 $\mu\text{s}$	2.237 $\mu\text{s}$	1.084 $\mu\text{s}$	1.150 $\mu\text{s}$

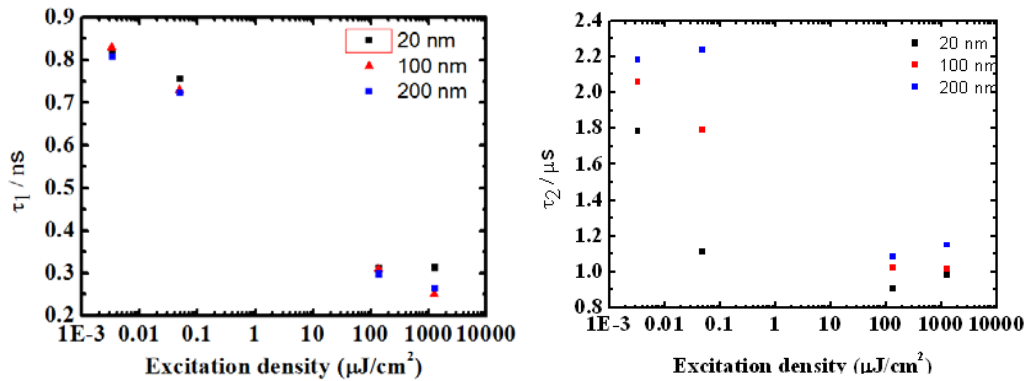


Fig. 4-11 (a)  $\tau_1$  and (b)  $\tau_2$  values of 20, 100, and 200 nm rubrene thin films.

Comparing the  $\tau_2$  at the same pulse energy with different rubrene thickness (20, 100, and 200 nm), we can see that this value decreased with thinner rubrene film. In this case, non-germinate recombination rate increased due to exciton spatial confinement. To further understand such mechanism, a series rubrene thin film with the thickness of 5 to 300 nm was fabricated with the excitation energy density of 43  $\mu\text{J}/\text{cm}^2$ . As the thickness of rubrene increased,  $\tau_1$  almost kept the same while  $\tau_2$

increased, as shown in Fig. 4-12 and Table 4-5. It can be attributed to caging effect, which triplet exciton were caged by thin rubrene film. The schema of this idea is shown in Fig. 4-12 (d). The decrement of  $\tau_2$  in thinner film is cause by the increment of  $k_{fus}$  term in equation 4-7.

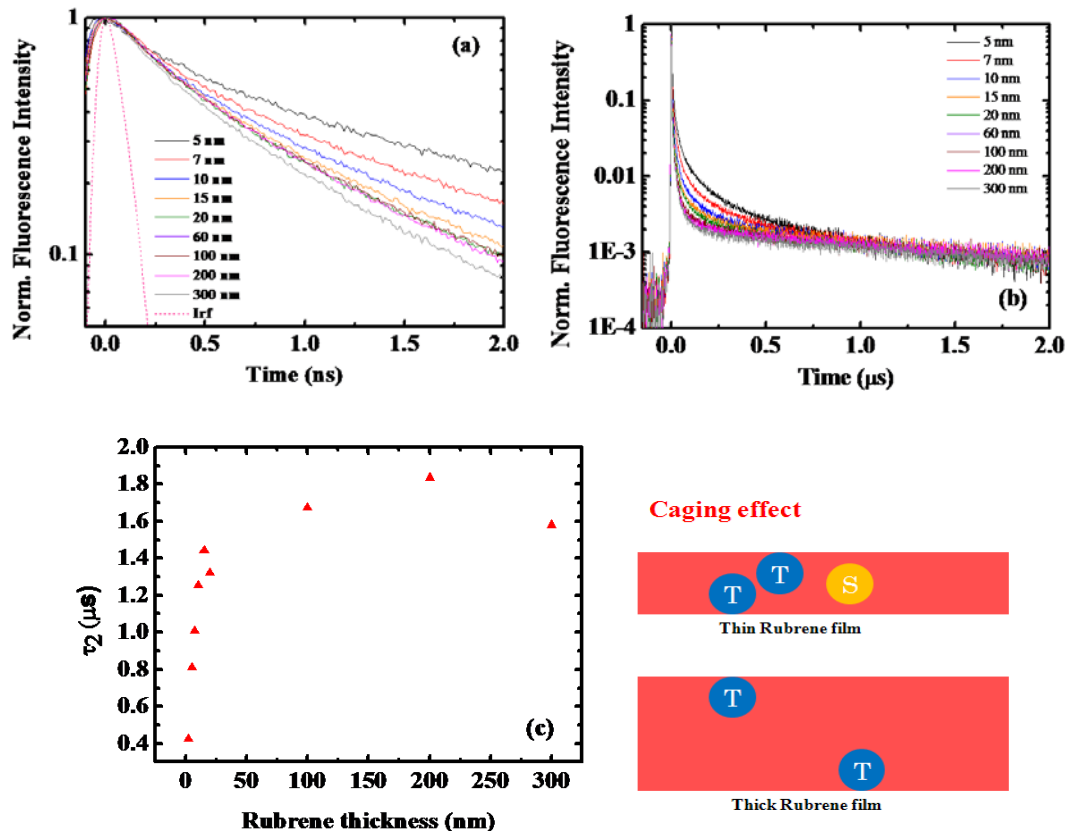


Fig. 4-12 Normalized TrPL fluorescence decay response for different thickness of rubrene for (a) 2 ns window, (b) 2  $\mu$ s window, (c)  $\tau_2$  versus thickness and (d) schema of caging effect.

Table. 4-7  $\tau_2$  for different thickness of rubrene under 43  $\mu$ J/cm<sup>2</sup>

Thickness (nm)	5	7	10	15	20	100	200	300
$\tau_2$ ( $\mu$ s)	0.811	1.008	1.254	1.444	1.322	1.674	1.836	1.582

## 5 Chapter 5 Conclusion



### 5.1 Summary

In chapter 3 of this dissertation, we demonstrated OSC device performances based on the four electron donor materials, DTCPB, DTCTB, DTCPBO, and DTCTBO with D-A-A configurations and C<sub>60</sub> and C<sub>70</sub> as electron acceptor materials. Although we have tried different device configurations, such as planar heterojunction and donor buffer layer, it is interesting that the OSCs with simple bulk heterojunction structure exhibited highest PCE with our electron donor materials. The highest PCE (6.55%) was achieved by using DTCPB and C<sub>70</sub> as electron donor and acceptor materials, with V<sub>OC</sub>, J<sub>SC</sub> and FF of 0.89 V, 11.12 mA/cm<sup>2</sup>, and 65.63%, respectively.

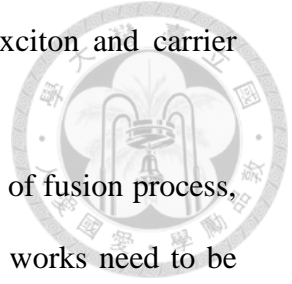
In chapter 4, we obtained the  $k_{rad}$  of rubrene dissolved in toluene solution as 0.088 ns<sup>-1</sup> and  $k_{sf}$  under different temperature without the influence of SSA. By fitting the  $k_{sf}$  under different temperature, we obtained the activation energy for amorphous rubrene is 24 meV. And thinner rubrene (5 nm) exhibited higher fusion rate, which resulted from higher probability for non-germinate recombination. Such phenomenon was also observed when increasing the input power to the thicker film (100 nm rubrene at 43.4  $\mu$ J/cm<sup>2</sup>).

### 5.2 Future work

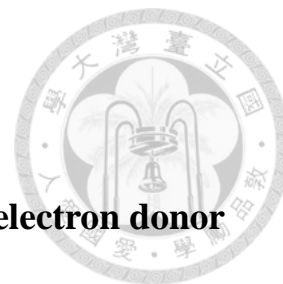
The performance of bulk OSC could be possibly improved by the following concepts by: (1) layer structure engineering by adding more functional layers (such as buffer layer(s) to reduce the recombination or enhance the cavity effect), and (2)

engineering the mixing ratio at different position to adjust the exciton and carrier dynamics.

Although we can qualitatively explain our experimental results of fusion process, a complete and quantitative model is needed and more simulation works need to be done for clarifying germinate and non-germinate recombination process, as well as exciton diffusion dynamics in thin and thick rubrene films.



## Appendix



### Appendix. I Morphology for four single cyano groups electron donor materials

In this section, we measure the roughness of these four compound. D/A interface is important for device and material engineering because a suitable phase separations would be pursued especially for thermal deposition OSCs. Here, four compounds were deposited on quartz with 50 nm, 1 anstrong per second to measured under AFM which shown in Fig. A-1 .

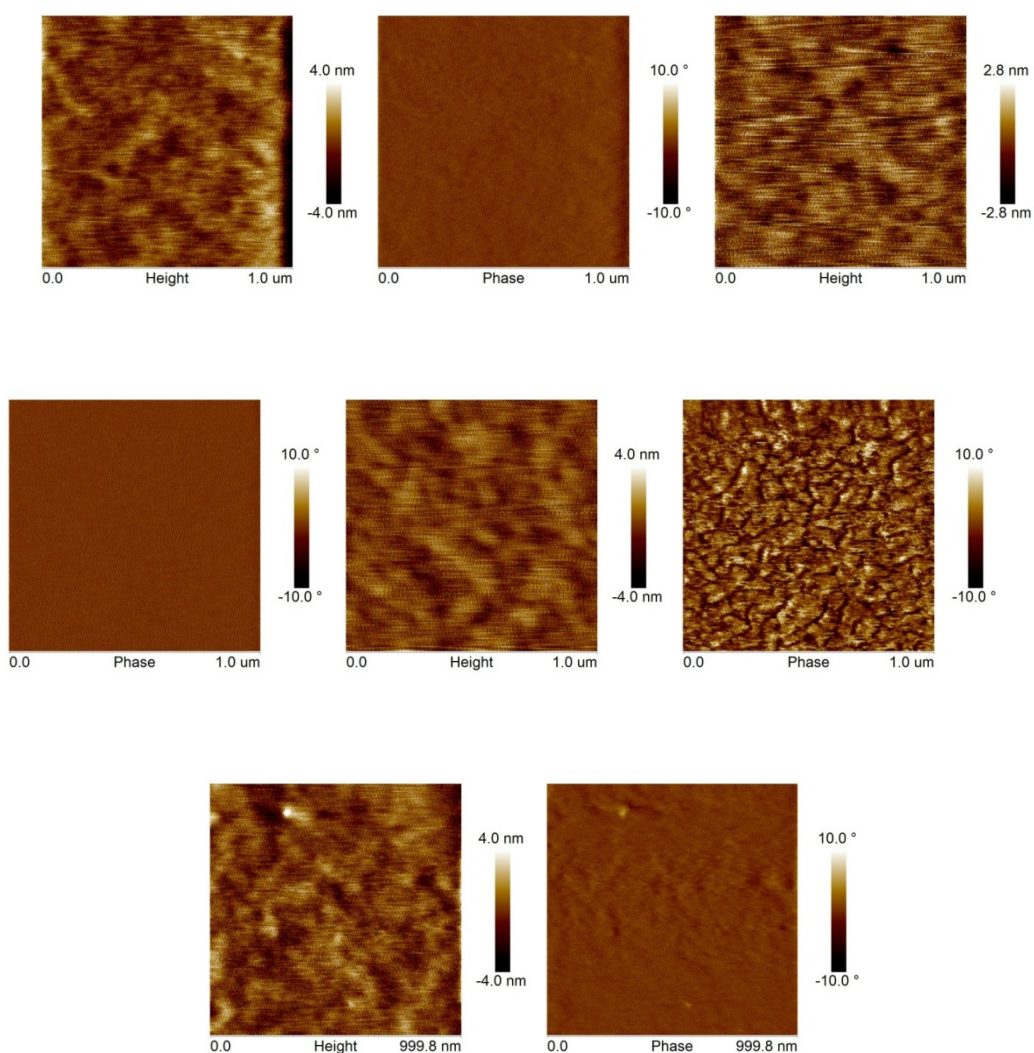


Fig. A-1 AFM image for roughness and phase for (a) DTCTB (b) DTCPB (c) DTCBPO (d) DTCTBO

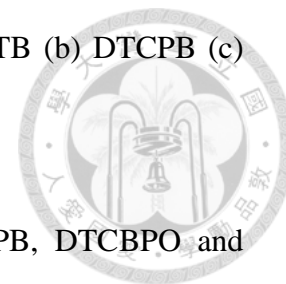


Table. A-1 AFM roughness and phase for DTCTB, DTCPB, DTCBPO and DTCTBO.

	DTCTB	DTCPB	DTCBPO	DTCTBO
Roughness (nm)	0.800	0.776	0.816	0.949
Phase (%)	0.67	0.71	2.97	0.6

The results for these four compounds were shown in Table. A-1. DTCPB show the lowest value and DTCTBO gives the harshest value among these four. Anyway, these four materials didn't show any aggregation and island in AFM image and the roughness were always lower than 1 nm, which implied a very amorphous situation can be formed. This is good to hear because a smoother roughness would be better when mix with acceptor, the coverage for electron donor to acceptor could be better and led to an increment for D/A interface, so the exciton can be well dissociated. For the comparison between BO and BT block, BO will slightly higher than BT. This might be result in a serious recombination for BO block. And the topography of thiophene groups also exhibit a little bit increase compare to phenylene groups. However, these small variations between their morphologies are hard to identify with final PCE accurately. In our future work, it will be clear to mix with acceptor with different mixing ratio and to observe the topography..



## Appendix. II Anisotropic characteristics of four single cyano groups electron donor materials

Molecules who equipped the anisotropic characteristic show a different refractive index or absorbance physical properties when the light is incident along to a different direction or polarization of its optical axis, as oppose to isotropic one. These kinds of materials always show the rod like shapes because light will be encountered at a different speed when it illuminate along at short (or long) axis and also called birefringence property. As shown in equation A, the slacken of light speed is due to the different refractive index, root of  $\epsilon_r * \mu_r$ , which  $\epsilon_r$  and  $\mu_r$  are the relative permittivity and permeability of the material. That means the optical constants can be separated and identified into the ordinary (in-plane) polarization,  $n_o + ik_o$  and the extraordinary (out-of-plane) polarization,  $n_e + ik_e$ . When the difference between ordinary and extraordinary becomes larger, the chromophore is more approach like rod shape. By the effort of Hao-Wu Lin's group, D-A-A system with dicyanoethylene based materials do shows an anisotropic property which the value  $n_o$  is larger than  $n_e$ . This implied that the molecular is laid on the substrate during self-packing which will help to harvest photon with the horizontal polarization more effectively.

$$v = \frac{c}{n} \quad \text{and} \quad \frac{x^2 + y^2}{n_o} + \frac{z^2}{n_e} = 1 \dots \dots \dots (A)$$

For the single cyan group substituent, all the neat film samples were deposited onto the silicon substrates with 1 angstrom/sec and measured by an angle-variation reflective ellipsometry SOPRA GESp5 as presented in the Fig. B-1.

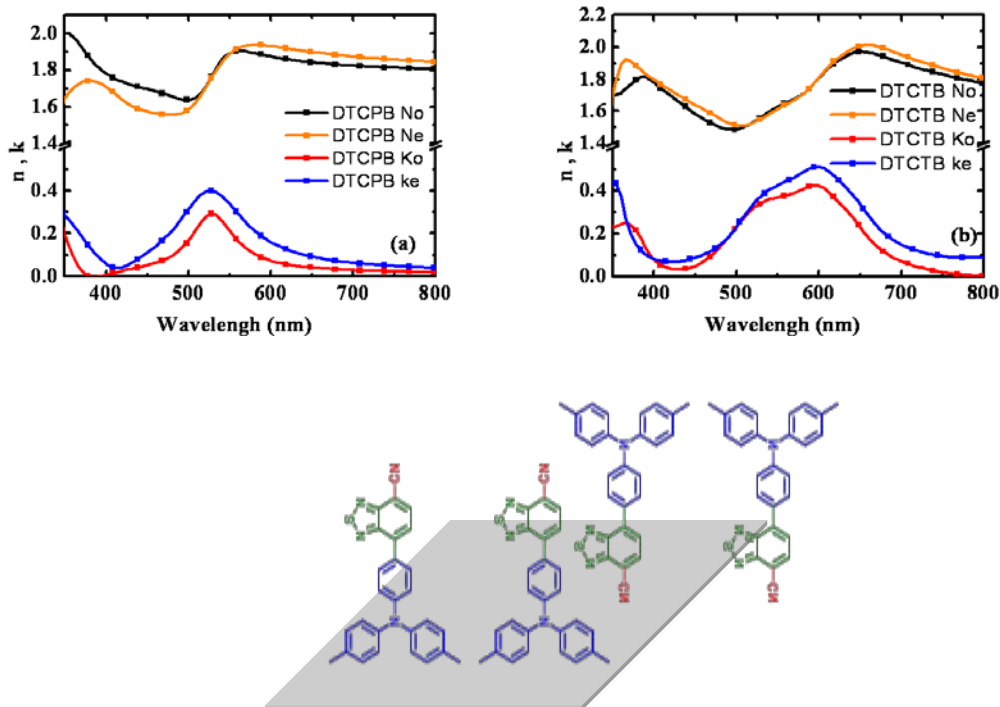


Fig. B-1 Anisotropic characteristics of (a) DTCPB, (b) DTCTB in thin film and (c) packing imaginary representation.

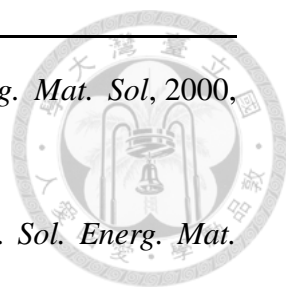
From Fig. B-1 (a) and (b), DTCPB and DTCTB also show an anisotropic characteristic. The difference between  $n_o$  and  $n_e$  ( $k_o$  and  $k_e$ ) exhibited a different value that give the evidence for rod-like shape of the materials during the packing. The worth thing to mentioned is the value of  $n_e$  ( $k_e$ ) is larger than the  $n_o$  ( $k_o$ ), dissimilar from the dicyanoethylene based molecules reported before. Geographically, the chromophore is standing straight on the substrate during the packing. This might be resulted from the changes of molecular length by replacing into single cyano one. A simple imaginary representation was shown in Fig. B-1 (c)

## References

---



- [1] Chapin, D. M, Fuller, C. S, Pearson, G. L. *J. Appl. Phys.*, 1954 (25), 676-677..
- [2] Aman, M. M, Solangi, K. H, Hossain, M. S, Kazi, S. N. *Renew. Sust. Energ. Rev.*, 2015 (41), 1190-1204.
- [3] Li, G, Zhu, R, Yang, Y. *Nature Photon*, 2012, 6(3), 153-161..
- [4] Riede, M., Mueller, Tress, W, Schueppel, R., Leo, K. *Nanotechnology*, 2008, 19(42), 424001.
- [5] Chapin, D. M, Fuller, C. S, Pearson, G. L. *J. Appl. Phys.*, 1954, (25), 676-677..
- [6] The NationCenter for Photovoltaic, National Renewable Energy Laboratory (NREL), (<http://www.nrel.gov/>)
- [7] Tang, C. W. *Appl. Phys. Lett*, 1986, 48(2), 183-185..
- [8] Bonham, J. S, Jarvis, D. H. *Aust. J. Chem*, 1977, 30(4), 705-720.
- [9] Park, C. D, Fleetham, T. A, Vogt, B. D. *Org. Electron.*, 2011, 12(9), 1465-1470.
- [10] Sariciftci, N. S, Smilowitz, L, Heeger, A. J, Wudl, F. *Science*, 1992, 258(5087), 1474-1476.
- [11] Miller, B, et al. *J. Am. Chem. Soc*, 1991, 113(16), 6291-6293.
- [12] Nojiri, T., Alam, M. M, Konami, H, Watanabe, A, Ito, O. *J. Phys. Chem. A*, 1997, 101(43), 7943-7947.
- [13] Pandey, R, Holmes, R. J. *Appl. Phys. Lett*, 2012, 100(8), 083303.
- [14] Heeger, A. J. *Adv. Mater*, 2014, 26(1), 10-28.
- [15] Ting, H. C, Chen, Y. H, Lin, L. Y, Chou, S. H, Liu, Y. H, Lin, H. W, Wong, K. T. *ChemSusChem*, 2014, 7(2), 457-465.
- [16] Peumans, P, Uchida, S, Forrest, S. R. *Nature*, 2003, 425(6954), 158-162.
- [17] Hiramoto, M, Fujiwara, H, Yokoyama, M. *J. Appl. Phys*, 1992, 72(8), 3781-3787.

- 
- 
- [18] Tsuzuki, T, Shirota, Y, Rostalski, J, Meissner, D. *Sol. Energ. Mat. Sol*, 2000, 61(1), 1-8.
- [19] Gebeyehu, D, Maennig, B, Drechsel, J, Leo, K, Pfeiffer, M. *Sol. Energ. Mat. Sol*, 2003, 79(1), 81-92.
- [20] Uchida, S, Xue, J, Rand, B. P, Forrest, S. R. *Appl. Phys. Lett*, 2004, 84(21), 4218-4220.
- [21] Zou, Y, Holst, J, Zhang, Y, Holmes, R. J. *J. Phys. Chem. A*, 2014, 2(31), 12397-12402.
- [22] Kageyama, H, Ohishi, H, Tanaka, M, Ohmori, Y, Shirota, Y. *Adv. Funct. Mater*, 2009, 19(24), 3948-3955.
- [23] Kim, B. G, Chung, K, Kim, J. *Chem. Eur. J*, 2013, 19(17), 5220-5230.
- [24] Wu, Y, Zhu, W. *Chem. Soc. Rev*, 2013, 42(5), 2039-2058.
- [25] Lin, L. Y, Chen, Y. H, Huang, Z. Y, Lin, H. W, Chou, Wong, K. T. *J. Am. Chem. Soc*, 2011, 33(40), 15822-15825.
- [26] Chen, Y. H, Lin, L. Y, Lu, C. W, Lin, F, Huang, Z. Y, Lin, H. W, Darling, S. B. *J. Am. Chem. Soc*, 2012, 134(33), 13616-13623.
- [27] Chiu, S. W, Lin, L. Y, Lin, H. W, Chen, Y. H, Huang, Z. Y, Wong, K. T. *Chem. Commun*, 2012, 48(13), 1857-1859.
- [28] Ting, H. C, Chen, Y. H, Lin, L. Y., Chou, S. H, Liu, Y. H, Lin, H. W, Wong, K. T. *ChemSusChem*, 2014, 7(2), 457-465.
- [29] Koster, L. J. A, Mihailetchi, V. D, Ramaker, R, Blom, P. W. *Appl. Phys. Lett*, 2005, 86(12), 123509-123509.
- [30] Kyaw, A. K. K, Wang, D. H, Gupta, V, Leong, W. L, Ke, L, Bazan, G. C, Heeger, A. *ACS nano*, 2013, 7(5), 4569-4577.
- [31] Cowan, S. R, Street, R. A, Cho, S, Heeger, A. J. *Phys. Rev B*, 2011, 83(3),

---

035205.

[32] Clarke, T. M, Peet, J, Nattestad, A, Drolet, N, Dennler, G, Lungenschmied, Mozer, A. J. *Org. Electron.*, 2012, 13(11), 2639-2646.

[33] Liu, L, Li, G. *Sol. Energ. Mat. Sol.*, 2011, 95(9), 2557-2563.

[34] Servaites, J. D, Ratner, M. A, Marks, T. J. *Energy Environ. Sci.*, 2011, 4(11), 4410-4422.

[35] Park, S. H, Roy, A, Beaupre, S, Cho, S, Coates, N, Heeger, A. J. *Nature Photon*, 2009, 3(5), 297-302.

[36] Ohkita, H, Cook, S, Astuti, Y, Duffy, W, Tierney, S, Zhang, W, Durrant, J. R. *J. Am. Chem. Soc.*, 2008, 130(10), 3030-3042.

[37] Shoaee, S, Clarke, T. M, Huang, C, Barlow, S, Marder, S. R, Durrant, J. R. *J. Am. Chem. Soc.*, 2010, 132(37), 12919-12926.

[38] Shockley, W, Queisser, H. J. *J. Appl. Phys.*, 1961, 32(3), 510-519.

[39] Nozik, A. J. *Chem. Phys. Lett*, 2008, 457(1), 3-11.

[40] Gabor, N. M, Zhong, Z, Bosnick, K, Park, J, McEuen, P. L. *Science*, 2009, 325(5946), 1367-1371.

[41] Beard, M. C, Knutsen, K. P, Yu, P, Luther, J. M, Song, Q, Nozik, A. J. *Nano Lett*, 2007, 7(8), 2506-2512.

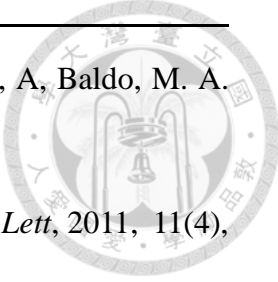
[42] Tauc, J. *J. Phys. Chem. Solids*, 1959, 8, 219-223.

[43] Greyson, E. C, Stepp, B. R, Chen, X, Schwerin, A. F, Paci, I, Smith, Ratner, M. A. *J. Phys. Chem. B*, 2009, 114(45), 14223-14232.

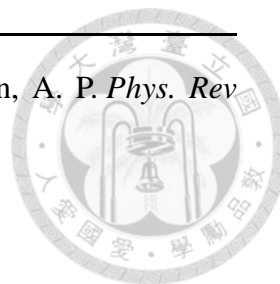
[44] Austin, R. H, Baker, G. L, Etemad, S, Thompson, R. *J. Chem. Phys.*, 1989, 90(11), 6642-6646.


[45] Lee, J, Jadhav, P, Reuswig, P. D, Yost, S. R, Thompson, N. J, Baldo, M. A. *Acc. Chem. Res.*, 2013, 46(6), 1300-1311.



- 
- 
- [46] Jadhav, P. J, Brown, P. R, Thompson, N, Wunsch, B, Mohanty, A, Baldo, M. A. *Adv. Mater*, 2012, 24(46), 6169-6174.
- [47] Jadhav, P. J, Mohanty, A, Sussman, J, Baldo, M. A. *Nano Lett*, 2011, 11(4), 1495-1498.
- [48] Congreve, D. N, Lee, J, Thompson, N. J, Hontz, E, Yost, S. R., Baldo, M. A. *Science*, 2013, 340(6130), 334-337.
- [49] Reusswig, P. D, Congreve, D. N, Thompson, N. J, Baldo, M. A. *Appl. Phys. Lett*, 2012, 101(11), 113304.
- [50] Singh, S, Jones, W. J, Siebrand, W, Stoicheff, B. P, Schneider, W. G. *J. Chem. Phys*, 1965, 42(1), 330-342.
- [51] Swenberg, C. E, Stacy, W. T. *Chem. Phys. Lett*, 1968, 2(5), 327-328.
- [52] Geacintov, N, Pope, M, Vogel, F. *Phys. Rev. Lett*, 1969, 22(12), 593.
- [53] Groff, R. P, Avakian, P, Merrifield, R. E. *Phys. Rev B*, 1970, 1(2), 815.
- [54] Arnold, S, Whitten, W. B. *J. Chem. Phys*, 1981, 75(3), 1166-1169.
- [55] Fleming, G. R, Millar, D. P, Morris, G. C, Morris, J. M, Robinson, G. W. *Aust. J. Chem*, 1977, 30(11), 2353-2359.
- [56] Jundt, C, Klein, G, Sipp, B, Le Moigne, J, Joucla, M, Villaeys, A. A. *Chem. Phys. Lett*, 1995, 241(1), 84-88.
- [57] Lee, J, Bruzek, M. J, Thompson, N. J, Sfeir, M. Y, Anthony, J. E, Baldo, M. A. *Adv. Mater*, 2013, 25(10), 1445-1448.
- [58] Müller, A. M, Avlasevich, Y. S, Schoeller, W. W, Müllen, K, & Bardeen, C. J. *J. Am. Chem. Soc*, 2007, 129(46), 14240-14250.
- [59] Wilson, M. W, Rao, A, Clark, J, Kumar, R. S. S, Brida, D, Cerullo, G, Friend, R. H. *J. Am. Chem. Soc*, 2011, 133(31), 11830-11833.
- [60] Burdett, J. J, Gosztola, D, Bardeen, C. J. *J. Chem. Phys*, 2011, 135(21), 214508.

- 
- [61] Jankus, V, Snedden, E. W, Bright, D. W, Arac, E, Monkman, A. P. *Phys. Rev B*, 2011, 87(22), 224202.
- [62] Casanova, D. *J. Chem. Theory Comput*, 2013, 10(1), 324-334.
- [63] Müller, H, Bässler, H, Vaubel, G. *Chem. Phys. Lett*, 1974, 29(1), 102-105.
- [64] Piland, G. B, Burdett, J. J, Kurunthu, D, Bardeen, C. J. *J. Phys. Chem. C*, 2013, 117(3), 1224-1236.
- [65] Herkstroeter, W. G, Merkel, P. B. *J. Photochem. Photobiol*, 1981, 16(4), 331-341.
- [66] Chen, Y., Lee, B, Fu, D, &Podzorov, V. *Adv. Mater*, 2011, 23(45), 5370-5375.
- [67] Burgdorff, C, Kircher, T, Löhmansröben, H. G. *Spectrochim. Acta Mol. Biomol. Spectrosc*, 1988, 44(11), 1137-1141.
- [68] Merrifield, R. E. *Pure Appl. Chem*, 1971, 27(3), 481-498.
- [69] Lee, J., Jadhav, P., Baldo, M. A. *Appl. Phys. Lett.*, 2009, 95(3), 033301.
- [70] Ma, L, Zhang, K, Kloc, C, Sun, H, Michel-Beyerle, M. E, Gurzadyan, G. G. *Phys. Chem. Chem. Phys*, 2012, 14(23), 8307-8312.
- [71] Ryasnyanskiy, A, Biaggio, I. *Phys. Rev B*, 2011, 84(19), 193203.
- [72] Wen, X, Yu, P, Yuan, C. T, Ma, X, Tang, J. *J. Phys. Chem. C*, 2013, 117(34), 17741-17747.
- [73] Rabinowitch, E. *Trans. Faraday Soc*, 1937, 33, 1225-1233.
- [74] Chuang, T. J, Hoffman, G. W, &Eisenthal, K. B. *Chem. Phys. Lett*, 1974, 25(2), 201-205.
- [75] Rabinowitch, E, & Wood, W. C. *Faraday Soc*, 1936, 32, 1381-1387.
- [76] Laidler, K. J. *IUPAC*, 1996, 68(1), 149-192.
- [77] Weeks, E. R, &Weitz, D. A. *Chem. Phys*, 2002, 284(1), 361-367.
- [78] Braden, D. A, Parrack, E. E, Tyler, D. R. *Coord. Chem. Rev.*, 2011, 211(1), 279-294.



- 
- 
- [79] Jack, R. L, Garrahan, J. P. *J. Chem. Phys*, 2005, 123(16), 164508.
- [80] Donkó, Z, Kalman, G. J, Golden, K. I. *Phys. Rev. Lett*, 2002, 88(22), 225001.
- [81] Hofberger, W. *Phys. Status Solidi*, e
- [82] Arnold, S, Alfano, R. R, Pope, M, Yu, W, Ho, P, Selsby, R, Swenberg, C. E. *J. Chem. Phys*, 1976, 64(12), 5104-5114.
- [83] Arnold, S, Swenberg, C. E, & Pope, M. *J. Chem. Phys*, 1976, 64(12), 5115-5120.
- [84] Hochstrasser, R. M, Whiteman, J. D. *J. Chem. Phys*, 1972, 56(12), 5945-5958.
- [85] 楊雅婷,“小分子有機太陽能電池及非平面液晶元件結構之研究”台大光電所碩士論文(2013)
- [86] 丁浩淳,“應用於有機太陽能電池之小分子材料的設計、合成與鑑定”台大化學所碩士論文 (2014).
- [87] 陳柏勳,“藍色磷光有機發光二極體暫態機制與有機薄膜製作於矽基板之研究”台大光電所碩士論文 (2014).
- [88] Piland, G. B, Burdett, J. J, Kurunthu, D, Bardeen, C. J. *J. Phys. Chem. C*, 2013, 117(3), 1224-1236.
- [89] Herkstroeter, W. G., Merkel, P. B., *J. Photochem.*, 1981, 16(4), 331-341.
- [90] Tao, S., Matsuzaki, H., Uemura, H., Yada, H., Uemura, T., Takeya, Okamoto, H., 2011, *Phys. Rev. B*, 83(7), 075204.